

IFT - UNESP
INSTITUTO DE FÍSICA TEÓRICA

Doctoral Thesis

IFT–T.003/2024

Advances in Electronic Transport Theory and Applications

Felippe Pereira Amorim

Supervisor
Alexandre Reily Rocha

Co-supervisor
Mauro Ferreira

March, 2024

Amorim, Felippe Pereira
A524a Advances in electronic transport theory and applications / Felippe Pereira Amorim. – São Paulo, 2024
133 f.: il. color.

Tese (doutorado) – Universidade Estadual Paulista (Unesp), Instituto de Física Teórica (IFT), São Paulo
Orientador: Alexandre Reily Rocha
Coorientador: Mauro Ferreira

1. Física. 2. Matéria condensada. 3. Física do estado sólido. I. Título

Sistema de geração automática de fichas catalográficas da Unesp. Biblioteca do Instituto de Física Teórica (IFT), São Paulo. Dados fornecidos pelo autor(a).

ADVANCES IN ELECTRONIC TRANSPORT

THEORY AND APPLICATIONS

Tese de Doutorado apresentada ao Instituto de Física Teórica do Câmpus de São Paulo, da Universidade Estadual Paulista "Júlio de Mesquita Filho", como parte dos requisitos para obtenção do título de Doutor em Física, Especialidade Física Teórica.

Comissão Examinadora:

Prof. Dr. ALEXANDRE REILY ROCHA (Orientador)
Instituto de Física Teórica/UNESP

Prof. Dr. DANILO BARBOSA LIARTE
Instituto de Física Teórica/UNESP / ICTP-SAIFR

Prof. Dr. LUIS GREGORIO GODOY DE VASCONCELOS DIAS DA SILVA
Instituto de Física/Universidade de São Paulo

Prof. Dr. GERSON FERREIRA JUNIOR
Instituto de Física/Universidade Federal de Uberlândia

Prof. Dr. MATHEUS PAES LIMA
Instituto de Física/Universidade Federal de São Carlos

Conceito: Aprovado

São Paulo, 15 de abril de 2024.

To my parents

Agradecimentos

Em primeiro lugar eu agradeço a minha família, que sempre foi meu alicerce em cada passo dessa jornada. Em especial, agradeço aos meus pais, Vilma e Pedro e à minha irmã, Larissa, por estarem ao meu lado em todos os momentos e por sempre me insentivarem a lutar meus sonhos.

Agradeço ao meu orientador, Alexandre. Seus valiosos ensinamentos e as várias discussões foram fundamentais para o desenvolvimento deste trabalho. Também sou grato por sua paciencia e compreensão, além de me dar toda a liberdade para perseguir as minhas idéias. Todos estes fatores contribuiram para tornar o processo de investigação científica muito mais instigante e desafiador.

Agradeço ao meu orientador do doutorado sanduiche, Mauro, por todas as discussões e sábios conselhos. Sua orientação tornou a minha experência em Dublin única, contribuindo tanto em nível acadêmico para o desenvolvimento deste trabalho, quanto a nível pessoal.

Agradeço aos meus amigos, tanto os de longa data quanto aos que tive a oportunidade de conhecer ao longo desta jornada: Matheus, Lucas, Enzo, Gabriel, Jogean, Thais, Denner, Raul, Silas e tantos outros. Agradeço pelos vários cafés e pelos vários ótimos momentos que compartilhamos juntos. Cada um de voĉes contribui para tornar a jornada muito mais leve e agradável. Espero revê-los.

Agradeço aos amigos que tive a oportunidade de conhecer durante o meu durante o meu doutorado sanduiche: Shardul, Umit, Sumanta, Anitta, Suman, Matheus, Antik, Sonal, Dhanashree, Andrew e muitos outros. Nunca irei esquecer das várias pints e dos ótimos momentos que tivemos juntos, vocês tornaram a minha experiencia em dublin única e serei eternamente grato por isso. Espero revê-los em breve.

Agradeço a minha namorada, Shubhrima. Desde que lhe conheci, voĉe tem sido uma pessoa muito especial com a qual eu tenho aprendido muito. Agradeço por todo o suporte, paciência e companheirismo.

Agradeço à agência de fomento CNPq pela bolsa de estudos no Brasil e reserva técnica. Também agradeço à agência CAPES pela bolsa de estudos, despesas de viagens, todos os auxílios e suporte necessário para o desenvolvimento do doutorado sanduíche no Trinity College Dublin, Irlanda.

Fica aqui o meu mais sincero agradecimento à todos os que contribuíram para que eu chegasse até aqui. Esta conquista é nossa.

Acknowledgements

Firstly, I express my gratitude to my family, who has always been my foundation at every step of this journey. In particular, I thank my parents, Vilma and Pedro, and my sister, Larissa, for being by my side at all times and for constantly encouraging me to pursue my dreams.

I extend my gratitude to my supervisor, Alexandre. His valuable teachings and numerous discussions were crucial to the development of this work. I am also thankful for his patience and understanding, as well as for granting me the freedom to pursue my ideas. All these factors contributed to making the process of scientific research much more intriguing and enjoyable.

I thank my Ph.D. sandwich program supervisor, Mauro, for all the discussions and wise advises. His guidance made my experience in Dublin unique, contributing both academically to the development of this work and personally.

Thanks to my friends, both those I've known for a long time and those I had the opportunity to meet along this journey: Matheus, Lucas, Enzo, Gabriel, Jogean, Thais, Denner, Raul, Silas, and many others. I am grateful for the numerous coffees and the many great moments we shared together. Each one of you contributes to making the journey much lighter and more enjoyable. I hope to see you again.

I express my gratitude to the friends I had the opportunity to meet during my Ph.D. sandwich program: Shardul, Umit, Sumanta, Anitta, Suman, Matheus, Antik, Sonal, Dhanashree, Andrew, and many others. I will never forget the various pints and the great moments we had together; you made my experience in Dublin unique, and I will be eternally grateful for that. I hope to see you again soon.

I thank my partner, Shubhrima. Since I met her, she has been a very special person from whom I have learned a lot. I thank for all the support, patience, companionship and all the good times that we shared together and all the ones that we are still going to live .

I express my thanks to the CNPq funding agency for the scholarship in Brazil and the technical reserve. I also thank the CAPES agency for the scholarship, travel expenses, all aids, and necessary support for the development of the Ph.D. sandwich program at Trinity College Dublin, Ireland.

My sincerest thanks to everyone who contributed to bringing me to this point. This achievement is ours.

"God used beautiful mathematics in creating the world"

Paul A. M. Dirac

Resumo

A teoria de transporte eletrônico é uma parte fundamental da física da matéria condensada que investiga o movimento de elétrons através de materiais, proporcionando insights cruciais em vários fenômenos e possibilitando avanços na tecnologia. Em sua essência, a teoria de transporte eletrônico aborda o comportamento complexo dos elétrons em sistemas quânticos. Este domínio teórico engloba uma rica diversidade de fenômenos, desde interferência quântica e tunelamento até o efeito de complexas interações de muitos corpos.

Uma parte crucial no desenrolar histórico da teoria do transporte eletrônico é a teoria de Landauer-Büttiker, formulada em 1957 por Rolf Landauer. Esta teoria estabeleceu a base para compreender a condutância de elétrons em sistemas mesoscópicos, conectando o comportamento microscópico dos elétrons com a condutância macroscópica do sistema. Sendo especialmente adequada para o regime transporte coerente, a teoria de Landauer realça a dualidade onda-partícula, onde a função de onda se propaga pelo sistema mantendo relações de fase entre os estados quânticos.

Quando o sistema em estudo é caracterizado pela existência de interações de muitos corpos, o formalismo de Landauer falha em descrever suas propriedades de transporte. De fato, neste caso, as interações de muitos corpos entre as partículas do sistema podem resultar em espalhamentos incoerentes e/ou inelásticos, exigindo assim uma abordagem mais sofisticada. Este problema pode ser abordado utilizando o formalismo das funções de Green fora do equilíbrio, com base no qual Meir e Wingreen propuseram uma expressão geral para a corrente eletrônica.

Neste trabalho, estudaremos os fenômenos de transporte eletrônico empregando diferentes metodologias com diferentes níveis de complexidade teórica. Cada uma das técnicas apresentadas, que variarão do método da matriz de transferência (usado no estudo do transporte coerente) à Funções de Green Fora do Equilíbrio (um método sofisticado usado no estudo de sistemas com interações de muitos corpos), será utilizada para abordar diferentes problemas em aberto na área de física da matéria condensada.

Iremos explorar as características de transporte em isolantes topológicos empregando o método da matriz de transferência. Utilizando-se deste método será desenvolvido uma teoria quantitativa que examine como momentos magnéticos

locais afetam as propriedades de transporte em isolantes topológicos bidimensionais de HgTe. Além disso, iremos avaliar numericamente e separadamente o impacto de spins nucleares e de impurezas magnéticas nestas propriedades.

A teoria de transporte também será aplicada para investigar as propriedades eletrônicas e termoelétricas de um material recentemente sintetizado: um ponto quântico de grafeno armchair 7-14-7. O estudo destas propriedades será realizado por meio de cálculos atomísticos *ab initio*, utilizando uma combinação de métodos de funções de Green fora do equilíbrio e Teoria do Funcional Densidade.

Finalmente, além de aplicar a teoria do transporte a problemas práticos, também contribuímos para a teoria ao fornecer uma base matemática para a abordagem de Ng. Além disso, uma será realizada uma generalização do formalismo de Buttiker-Landauer por meio da definição de uma transmissão generalizada aplicável a sistemas com interações de muitos corpos. A expressão derivada será usada para examinar as propriedades de transporte eletrônico de um ponto quântico descrito pelo modelo de impureza de Anderson no regime de Bloqueio Coulombiano.

Palavras Chaves: Transporte Eletrônico; Isolantes Topológicos; Funções de Green fora do equilíbrio; Pontos quânticos de grafeno; Pontos quânticos; Interações de muitos corpos.

Áreas do conhecimento: Física; Física da Matéria Condensada; Fenômenos de Transporte.

Abstract

Electronic transport theory is a fundamental framework in condensed matter physics that investigates the movement of electrons through materials, offering crucial insights into various phenomena and enabling advancements in technology. At its core, electronic transport theory addresses the intricate behaviors of electrons in quantum systems, where classical concepts are transposed into the quantum realm. This theoretical domain encompasses a rich tapestry of phenomena, ranging from quantum interference and tunneling to the complex effects of many-body interactions.

One cornerstone in the historical development of electronic transport theory is the Landauer-Büttiker theory, formulated in 1957 by Rolf Landauer. This theory laid the foundation for understanding the conductance of electrons in mesoscopic systems, connecting microscopic electron behavior with the macroscopic conductance of the system. Particularly well-suited for coherent transport, Landauer's theory illuminates the wave-particle duality, where electronic waves propagate across a system while maintaining phase relations among quantum states.

When the system under study is characterized by the existence of many-body interactions the Landauer formalism fails to describe its transport properties. Indeed, in this case, the intricate many-body interactions among its particles may lead incoherent and/or inelastic scatterings, thus requiring a more sophisticated approach. This problem can be dealt with by employing the formalism of Non-equilibrium Green's functions, based on which Meir and Wingreen proposed a general expression for the electronic current.

In this work, we are going to study the phenomena of electronic transport by employing different methodologies with increasing level of theoretical complexity as it is required by the system being studied. Each of the presented techniques, which will range from the transfer matrix method (used in the study of coherent transport) to Non-Equilibrium Greens Functions (a sophisticated method used in the study of systems with many-body interactions), will be used to approach different open problems in physics.

We are going to address the transport properties of topological insulators, where the transfer matrix method will be employed to create a quantitative theory for the influence of local magnetic moments on the transport properties of

two-dimensional HgTe topological insulators. The impact of nuclear spins and magnetic impurities on these properties is also quantified.

The transport theory will also be applied to investigate the electronic and thermoelectric properties of a recently synthesized graphene quantum dot, specifically the 7-14-7 armchair graphene quantum dot. *Ab initio* atomistic numerical calculations, utilizing a combination of Non-equilibrium Green's functions and Density Functional Theory methods, are performed.

Finally, in addition to applying the transport theory to practical problems, we also give contribution to the theory by providing a mathematical foundation for the Ng ansatz. Additionally, a generalization of the Buttiker-Landauer approach is introduced by defining a generalized transmission applicable to many-body interacting systems. The derived expression is used to examine the electronic transport properties of a quantum dot described by the Anderson impurity model in the Coulomb Blockade regime.

Keywords: Electronic Transport ; Topological Insulators; Non-equilibrium Green's functions ; Graphene quantum dots; Many-body interactions.

Knowledge Areas : Physics; Condensed Matter Physics; Transport Phenomena.

Contents

1 Introduction **11**

1.1 Anderson Localization 11
1.2 Topological Materials 13
1.3 Graphene Quantum Dots 13
1.4 General Aspects About Electronic Transport and Thesis Structure . 14

2 Landauer-Büttiker Approach and the Influence of Magnetic Impurities on the Transport Properties of HgTe Topological States **20**

2.1 Introduction 20
2.2 Landauer-Büttiker Approach and the Transfer Matrix Method . . . 22
2.3 2DTI Model and the Hyperfine Interaction 25
2.4 Model Analysis 29
2.5 Anomalous Localization 31
2.6 Contact to experiments - hyperfine interaction 39
2.7 Supression in the conductivity due to Mn magnetic impurities . . . 41
2.8 Conclusions 44

3 Green's Function And Many-body Techniques **46**

3.1 Introduction 46
3.2 Real Time GF 47
3.3 Non-Equilibrium Greens Functions Formalism 54
3.4 General current equation 58
3.5 Thermoeletric transport properties 62

4 Gate-voltage enhancement of thermoelectric transport in graphene nanoribbons quantum dots **65**

4.1 Introduction 65
4.2 Methodology 66
4.3 Discussion 69
4.4 Conclusions 74

5 Generalized Landauer-Buttiker formula: Effective transmission for systems with many-body interactions **75**
5.1 Introduction 75
5.2 Meir-Wingreen and the ansatz based effective transmission 77
5.3 Charge Flux Conservation and the Effective Transmission 80
5.4 Uncorrelated Transport 84
5.5 Sequential Tunneling Transport 86
5.6 Applications: The single and Double Impurity Anderson Model . . 88
5.7 Conclusions 95

6 General Conclusions **97**

A Scientific Publications **100**

B Transfer Matrix of Local Magnetic Moment **101**

C Proportional coupling condition for systems with inversion symmetry **103**
C.1 Recovering the proportional coupling regime for parity symmetric systems 108

D Non-equilibrium multilevel Anderson model in the Non-crossing approximation **112**
D.1 General multilevel Anderson impurity model 113

Bibliography **119**

Chapter 1

Introduction

The behavior of electrons in quantum systems stands as a paradigmatic example of the intricacies that arise when classical concepts are transposed to the quantum realm. Electronic transport in quantum systems encompasses a rich tapestry of phenomena, ranging from quantum interference and tunneling to the delicate interplay between electron-electron interactions and external perturbations. This realm of investigation is particularly pertinent in the context of emerging technologies such as quantum computing, spintronics, and quantum communication, where understanding and manipulating electron transport on the nanoscale are critical.

Historically, the theoritical description of electronic transport in quantum systems was marked by the Landauer-Büttiker theory initially formulated in 1957 by Rolf Landauer [1]. His work laid the foundation for understanding the conductance of electrons in mesoscopic systems as it allowed to connect the microscopic behavior of electrons with the macroscopic conductance of the system.One of the characteristic of Landauer's theory is that is better suited for the description of the, so called, coherent transport. In this regime the wave-particle duality manifests itself in such a way that the electronic waves propagates across the system maintaning the phase relations among the quantum states.

1.1 Anderson Localization

A plethora of phenomena may arise in coherent transport due to constructive or destructive interference of the electronic wave-function, an important and classic example is the Anderson Localization introduced by Philip W. Anderson in 1958 [2]. This phenomena, depicted in figure 1.1, can be summarized as the localization of the electron due to destructive interference of the wave function in disordered systems and it stands in contrast to the conventional understanding of electronic

transport in crystalline materials, where electrons move freely, contributing to electrical conductivity. The disorder can come from different sources, which can be impurities, defects, or random variations in the potential, but it must effectively create a non-uniform environment for electrons, as the disorder increases there's a point beyond which the electronic states undergo a transition from extended states, where electrons can move freely, to localized states, where electrons are confined to specific regions. The regime of Anderson localization is associated with an exponential decay of the wave-function on the systems size. This allows the phenomena to be characterized by a single parameter named localization length which, basically, determines how far an electron can propagate before its wavefunction becomes significantly localized due to interference effects.

Starting from the concept of localization, other related phenomena can be observed. One such effect is anti-localization [3, 4], a quantum interference phenomenon in which strong spin-orbit coupling leads to destructive interference, reducing the likelihood of electron backscattering and enhancing conductivity. This effect is commonly observed in systems with strong spin-orbit interactions, such as topological insulators and 2D electron gases. Additionally, the lesser known phenomenon of anomalous localization [5, 6, 7] can occur. Unlike conventional Anderson localization, anomalous localization arises due to more complex factors like nonlinear interactions or quasiperiodic potentials, leading to unconventional and sometimes stronger electron trapping behavior. In these cases, the localization length can exhibit non-standard dependencies on system parameters.

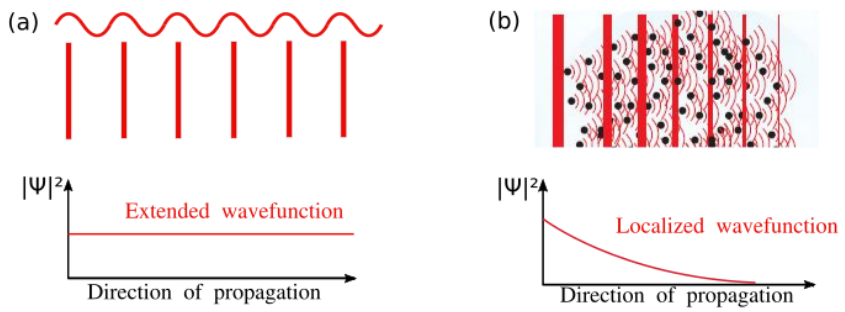


Figure 1.1: (a) The wavefunctions of crystaline ordered systems extend across the direction of propagation, leading to a constant probability density along this direction. (b) Anderson Localization: The disorder caused by random impurities induces coherent destructive interference of the wavefunction, resulting in exponential decay along the direction of propagation. Figure adapted from [8]

1.2 Topological Materials

With the advances in the creation and controlability of mesoscopic systems the realization of devices displaying coherent transport and other quantum interference related phenomena has been achieved by a number of experiments [9, 10, 11]. These advances in nanotechnology has also paved the way for the discovery of new materials with unique electronic properties. One important example of such materials are the topological insulators. With first experimental realization in 2007 on HgTe quantum wells, the topological insulators possess an insulating bulk, characterized by a band gap, akin to conventional insulators, however, their defining feature lies in the existence of robust, conducting surface states within this band gap. These surface states are topologically protected, rendering them immune to local perturbations and impurities. At the heart of topological insulators lies the concept of nontrivial topological order. In two dimensions, this is manifested as the quantum spin Hall effect [12, 13], where counter-propagating edge states with opposite spins coexist along the material's boundary, as depicted in figure 1.2. This spin-polarized surface conduction is a consequence of the nontrivial topology of the electronic wavefunctions.

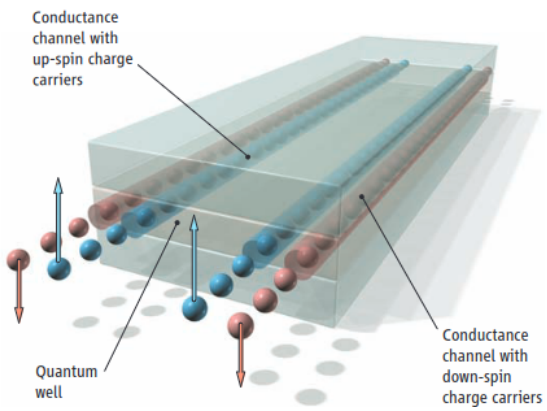


Figure 1.2: Schematic representation of the spin-polarized edge channels in the quantum Hall effect. Figure obtained from [14]

1.3 Graphene Quantum Dots

Another instance of material with remarkable properties is single-layer graphene sheet. Firstly produced in 2004 by Andre Geim and Konstantin Novoselov, this material consist of a two-dimensional single layer of carbon atoms arranged in

a hexagonal lattice. Its unique electronic, mechanical, and thermal properties make it a subject of intense scientific exploration and technological interest [15]. Graphene exhibits exceptional electrical conductivity, high thermal conductivity, and extraordinary mechanical strength, making it a promising candidate for a wide range of applications, including electronics, sensors, and materials science [16].

Within the realm of graphene, graphene quantum dots (GQDs) emerge as a distinctive class of nanomaterials (see figure 1.3). GQDs are small fragments of graphene with dimensions typically less than 10 nanometers, endowing them with quantum confinement effects. The quantum dots inherit some of the extraordinary properties of graphene, but their reduced size introduces quantum phenomena that offer additional opportunities for tailored electronic, optical, and thermal characteristics. As a result, graphene quantum dots have garnered attention for their potential applications in quantum computing, optoelectronics, and bioimaging, among others.

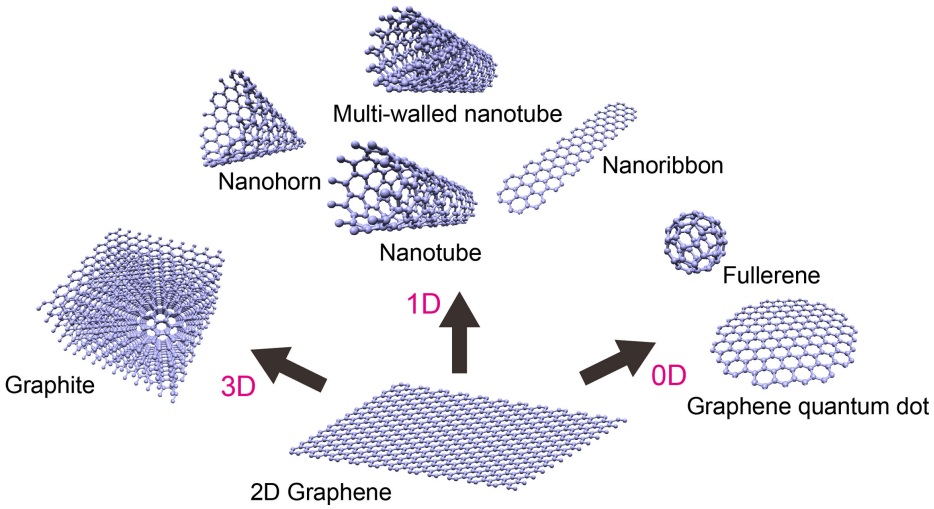


Figure 1.3: Classification of carbon allotropes derived from graphene. Figure obtained from [17]

1.4 General Aspects About Electronic Transport and Thesis Structure

Despite being capable of describing a vast category of systems, the Landauer formalism still has its limitations. In condensed matter physics we can find the so

called systems with many-body interactions. As the name suggest, these systems are characterized by having intricate interactions among its particles, which can give rise to emergent phenomena such as collective excitations, correlation effects, and phase transitions. Due to their complexity, the Landauer formalism fails to describe the transport properties of these systems and a more sophisticated approach should be used. A very powerfull method in dealing with many-body systems is Green's function formalism. It provides a systematic and elegant way to analyze the response of a system to external perturbations, allowing for the development of a perturbation theory which facilitates the calculation of various physical observables and offers insights into the spectral properties, correlation functions, and dynamic response of complex quantum systems. An extension of this formalism designed to study out-of-equilibrium quantum systems was independently proposed by Keldysh [18] and Kadanoff-Baym [19]. The Keldysh formalism is particularly valuable for studying quantum transport, open quantum systems, and phenomena such as quantum dissipation, offering a versatile tool to analyze time-dependent quantum dynamics. One important application of this formalism is the deduction of a general current equation, from which the Landauer formula is just a particular case in which interactions are treated up to the mean field level. In addition to the transport of charge, this formalism also allows us study the transport of heat across mesoscopic devices. It does so by providing the theoretical framework for deriving expressions for the electronic thermal conductance and other thermoelectronic quantities, such as the Seebeck coefficient, the latter being a measure of the Seebeck effect.

An important example of model with many-body interaction is the Anderson Impurity Model (AIM). Proposed by P. W. Anderson in 1961 [20], this model was designed to elucidate the behavior of localized magnetic impurities interacting with a conduction electron bath in a metallic host. The Anderson Impurity Model plays a crucial role in understanding the electronic structure and transport properties of materials containing magnetic impurities, providing insights into phenomena such as the Kondo effect [21]. Discovered in the early 30s, the Kondo effect is a phenomen where the interaction between the electrons bath and the magnetic impurities leads to an increasce in the metals resistivity for suficiently low temperatures, more specifically when the temperature reduces below the so called Kondo temperature. In conjunction with the AIM, the Kondo effect gained renewed attention in the late 90s, particularly following its rediscovery in the context of quantum dots [22]. Also known as artificial atoms, quantum dots are

essentially nanostructures that display discrete energy levels owing to quantum confinement. When subjected to sufficiently low temperatures, the Kondo effect manifest in these structures as an augmentation in conductance rather than a resistance increase, as is shown in figure 1.4. At higher temperatures, the observed phenomenon is the Coulomb blockade effect [23]. As the name suggest, this effect is a manifestation of electrostatic repulsion between individual electrons and it becomes prominent when the charging energy required to add or remove an electron from the structure exceeds the thermal energy of the system. As a result, the addition or removal of single electrons is energetically unfavorable, leading to discrete charge states and suppressed current flow, as is schematically represented in figure 1.5. Thus, given its wide range of applicability and its rich physics, the Anderson model is still today focus of active research in the scientific community [24] and, finding a simple way to obtain the bias-dependent conductance for a many-body interacting system like the Anderson model is therefore, a challenge worth pursuing.

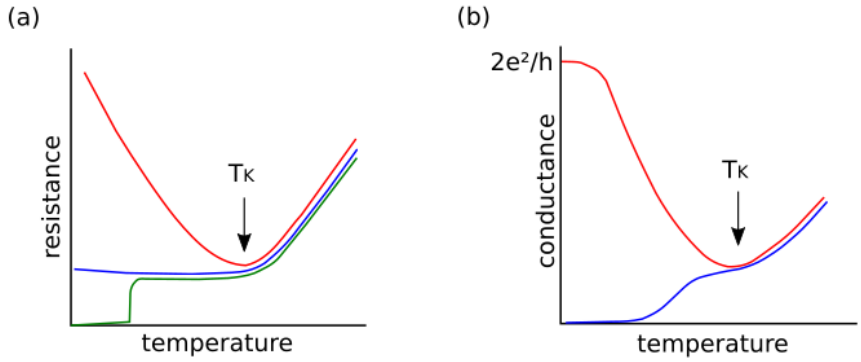


Figure 1.4: As the temperature of a metal is lowered, its resistance decreases until it saturates at some residual value(blue).Some metals become superconducting at a critical temperature(green). However, in metals that contain a small fraction of magnetic impurities, such as cobalt-in-copper systems, the resistance increases at low temperatures due to the Kondo effect (red). (b) A system that has a localized spin embedded between metal leads can be created artificially in a semiconductor quantum-dot device containing a controllable number of electrons. If the number of electrons confined in the dot is odd, then the conductance measured between the two leads increases due to the Kondo effect at low temperature (red). In contrast, the Kondo effect does not occur when the dot contains an even number of electrons and the total spin adds up to zero. In this case, the conductance continuously decreases with temperature (blue). Figure adapted from [25]

In this work, we are going to study the phenomena of electronic transport by

employing different methodologies with increasing level of theoretical complexity as it is required by the system being studied. Each of the presented techniques, which will range from the transfer matrix method (used in the study of coherent transport) to Non-Equilibrium Greens Functions (a sophisticated method used in the study of systems with many-body interactions), will be used to approach different open problems in physics.

Together with the transfer matrix method, the Buttiker-Landauer formalism will be presented on chapter two. As applications, this method will be used to develop a quantitative theory for the effect of local magnetic moments in the transport properties of two-dimensional topological insulators (2DTI). The occurrence of a local magnetic moment in a 2DTI may be attributed to different causes such as the existence of charge puddles or the presence of magnetic impurities. In both cases, different approaches had been used to study the impact of the magnetic moment in the transport properties of 2DTI. Considering a model accounting for the Coulomb interaction in the helical edge states and their coupling to the spin of a charge puddle, Maciejko et al. [26] predicted the existence of different regimes depending on the strength of the Coulomb interaction and the systems temperature. The effect of a local magnetic moment was also quantitatively studied by Kurilovich et al. [27], in which the deviation in the conductance of HgTe 2DTI due to a Mn magnetic impurity was calculated.

Despite being extensively studied [26, 27, 28, 29, 30, 31], a quantitative description of the cumulative effect of a macroscopically large ensemble of magnetic impurities on the conductance of 2DTIs has yet to be presented. To address this theoretical gap, we tackle this problem by modeling the helical edge states coupled with a large set of point-like magnetic moments. The magnetic moments are treated classically, given the technical challenges of dealing with a large number of quantum impurities.

Using the transfer matrix method, we develop a semi-analytical approach to calculate the conductance in such systems. In line with the results of [29], we observe the phenomenon of Anderson localization for a sufficiently large number of impurities. However, we also predict the existence of an intermediate regime of anomalous localization, characterized by an exponential decay of the conductance on the square root of number of impurities, which contrasts with traditional Anderson localization.

As application of the developed methodology, we study the effect of the hyperfine interaction with nuclear magnetic moments on the transport properties of

HgTe 2DTI. We show that, despite being a valid mechanism of suppression, the hyperfine interaction with the nuclear magnetic moments is not strong enough to have any impact in the conductance of HgTe 2DTI systems. We further apply our methodology to calculate the conductance in a HgTe 2DTI doped with dilute Mn impurities. We demonstrate that our predicted results are in striking accordance with the experimental findings of [32]. Additionally, we highlight the potential of HgTe 2DTI devices doped with Mn impurities for probing and studying the anomalous localization regime.

In chapter three it will be presented the Greens Function formalism. Being a more sophisticated method, the Green functions provide the tools to analyze quantum systems with many-body interactions. As an extension of this formalism it will also be presented the Non-equilibruim Greens Functions, which is suitable to analyze quantum systems out of thermodynamic equilibrium. This method will later be used to derive the general current equation.

In Chapter four, as an application of the NEGF formalism, the electronic and thermoelectric properties of a recently synthesized graphene quantum dot, known as the 7-14-7 armchair graphene quantum dot (AGQD) [33], will be investigated. This study is conducted by performing ab initio atomistic numerical calculations using software that combines the NEGF method with Density Functional Theory (DFT). We demonstrate how the electronic and thermoelectric properties of the quantum dot are influenced by the application of a gate voltage, with particular emphasis on the gate-induced enhancement of the figure of merit ZT, a quantity directly related to the thermal efficiency of the device.

In chapter five, we investigate how the concept of quantum transmission can be defined for systems with many-body interactions. Indeed, given a quantum system that can be approximated by a non-interacting Hamiltonian, the system's transmission can be readily calculated by the Buttiker-Landauer or the equivalent Fisher-Lee [34] approach. However, when many-body interactions are present, the definition of such quantity is not as straightforward as in the non-interacting case and any proposed effective transmission must account for both coherent and incoherent scattering. There are in the literature proposals for an effective transmission capable of accounting for many-body effects, albeit with limited range of applicability. In this chapter, by using the NEGF formalism, we demonstrate how the conservation of flux of charge can be used to deduce an equation constraining the lesser component and the anti-Hermitian part of the interacting self-energy's retarded component. This constraint equation will then be used to

present a proposal for an transmission probability capable of dealing with the most general interacting case. In addition to the general transmission equation, the case of fully incoherent transport is also studied. At this point, the equations to fully incoherent transport proposed by Meir-Wingreen [35] and Beenakker [36] are derived as a limiting case of a more general incoherent transport theory. Finally, the last chapter presents the conclusion and final remarks.

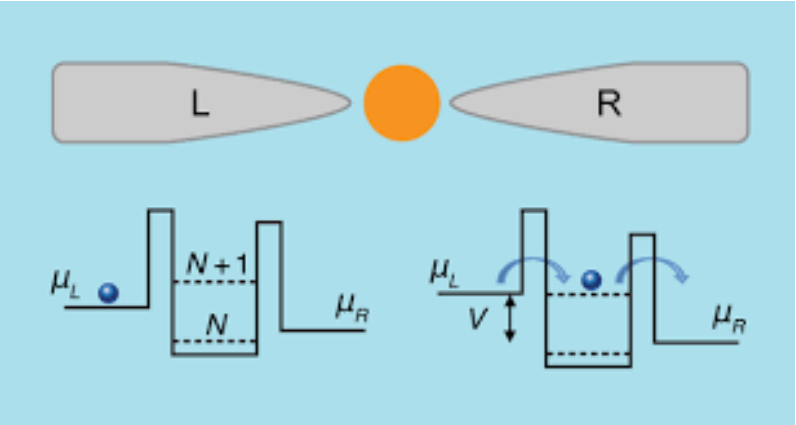


Figure 1.5: Schematic picture of Coulomb blockade in a nanoscale tunneling junction in which a quantum dot is weakly connected to two leads. Electrons can tunnel only if the bias voltage V is large enough to line up the chemical po- tential of the left lead (L) and an empty level. Otherwise the access is blocked due to the Coulomb repulsion caused by the filled N-electron leve. Figure adapted from [37].

Chapter 2

Landauer-Büttiker Approach and the Influence of Magnetic Impurities on the Transport Properties of HgTe Topological States

2.1 Introduction

The past few years has seen a significant increase in the number of topology-related studies, primarily driven by the field of Condensed Matter Theory. In particular, two-dimensional (2D) Topological Insulators (TI) have been the main focus of these studies. While there is no conduction in the bulk of these materials, current-carrying spin-polarised states exist near their edges, giving rise to a variety of intriguing yet technologically promising properties [38]. Also referred to as Quantum Spin Hall (QSH) systems [39, 40], in theory they must possess strong spin-orbit (SO) interaction, which may be intrinsic such as in inverted band semiconductor heterostructures and various other 2D materials [41], or extrinsic, usually generated by adatom doping [42] or by proximity effects [43]. Far from pure theoretical abstractions, numerous examples have been reported in semiconductor quantum wells [14, 44, 45, 46, 47], 2D crystals [48, 49, 50, 51], and graphene with adsorbed clusters [52], to name but a few.

The coexistence of time-reversal symmetry and momentum-spin locking prevents the occurrence of backscattering in 2D TI. Furthermore, this feature is predicted to arise regardless of how ordered the material is. In other words, scattering-free edge states are expected to withstand different levels of structural disorder. As a result, the conductance of these materials should coincide exactly with $\mathcal{G}_0 = 2e^2/h$, *i.e.*, the quantum conductance originated from the edge states. However, this is not the case and deviations from $\mathcal{G}_0$ have been observed in all

transport experiments to date, both in semiconductor heterostructures and in 2D crystals. The deviations depend on the system size but they are always present [44, 53, 54], a feature that remains a longstanding puzzle in the field [51, 55, 56].

Proposed physical mechanisms that may induce backscattering in 2DTI involve either intra- or inter-edge spin-flip scattering processes. The latter is highly unlikely for the simple fact that the edge states have a negligible penetration depth ζ compared with the characteristic sample diemnsions, *i.e.*, $\zeta \ll \mathcal{W}$, where $\mathcal{W}$ is the distance between opposite edges. Despite recent speculations that inter-edge scattering in semiconductor heterostructures could generate edge-connecting percolating paths[55] that would invalidate the above inequality, no quantitative evidence for such a behaviour has been reported to date. Regarding possible intra-edge mechanisms, at first glance one may find the presence of magnetic impurities as the most likely explanation for destroying the topologically protected edge states through spin-flip scattering processes. Nevertheless, the conductance suppression is seen in ultra clean MBE-grown heterostructures, which suggests that this explanation is also highly unlikely. These facts have motivated numerous studies that explore a plethora of ingenious mechanisms that could in principle break time-reversal symmetry, namely, noise [57], edge reconstruction [58], Rashba SO interaction [59], phonons [60], charge puddles [61], and adatom-induced scattering processes [62], to name but a few.

In view of the challenge of defining a mechanism responsible for deviations in the conductance of 2DTI, in this chapter it will be developed a methodology capable of providing a quantitative analysis from the impact from magnetic moments on the transport properties of edge states. The development of this methodology is motivated, in principle, to study the back-scattering mechanism due to the hyperfine interaction between electrons and nuclear spins [63, 64, 65] which, although weak, plays an important role in nanostrcutures, like for instance limiting the coherence of single electrons spins. Previous works have also considered that interplay of electron-electron interaction and disorder to discuss the effect of the hyperfine interaction on electronic transport in InAs/GaSb quantum wells using a helical Tomonaga-Luttinger model [66, 65, 56]. Here, we address HgTe systems, where interaction effects are not relevant (in the sense of renormalization groug), and we use a standard single-particle approach the combines analytical and numerical results based on the transfer matrix method. We use a realistic estimate of the hyperfine interaction matrix elements [63] that couple pairs of time-reversal symmetric electronic helical edges states to compute the deviations

of quantized conductance in 2DTIs as a function of system size.

In adition to the study of the effect of hyperfine interaction, this methodology will also be used to probe the impact of backscatterings induced by the presence of Mn magnetic impurities. In order to contrast theoretical predictions with experimental values, realistic estimations of parameters obtained from the literature will be used to estimate transport-related quantities for a particular HgTe 2DTI device. The predicted quantities are then contrasted with experimental values available in the literature.

Using the developed approach, we show that the interaction between local magnetic moments and edge states electrons is indeed a mechanism of supression of conductance in the model proposed for HgTe 2DTIs. We also show that the system is characterized by two different localization regimes with different levels of disorder: One in which it was observed a non-exponential localization and another for which an anomalous exponential localization is present, both in contrast with the widely known phenomena of Anderson localization [2]. Despite the observation of suppression of conductance, the analysis using realistic estimates for the parameters of the model for the hyperfine interaction shows that the calculated localization lengths surpasses by far the size of the devices used for experimental measures, what indicates that the hyperfine interaction is too weak to have any negligible effect in conductance of HgTe systems. On the other hand, the calculations performed for Mn impurities predicted a measurable effect on the conductance, in fact, the predictions has shown an outstanding agreement with experimental results.

2.2 Landauer-Büttiker Approach and the Transfer Matrix Method

As it was mentioned in the introduction, the Landauer-Büttiker (LB) formalism allows to describe the electronic transport properties of mesoscopic systems in terms of the microscopic behavior of electrons. It does so by establishing a relation between the wave functions (scattering amplitudes) of electrons in a quantum junction and the macroscopic conduction of this junction. The core concept of the formalism is the Landauer formula [67], which relates the conductance (G) of a

system to the transmission (T) of electrons through it:

$$G = \frac{e^2}{h} \sum_{ij} T_{i \to j}. \tag{2.1}$$

Here, e is the elementary charge, h is Planck's constant, and T_{ij} is the transmission probability from channel i to channel j. Therefore, in a typical coherent transport problem, one is usually interested in the calculation of the transmission probability of the electron to propagate across the quantum junction. As is depicted in figure (2.1), these structures can be divided into three parts: two ideal electrodes, which are assumed to be noninteracting [1] and in thermal equilibrium, and a central scattering region. As the name indicates, the scattering region is the place where scattering processes happen, leading to a possible transmission or reflection of the quantum particle.

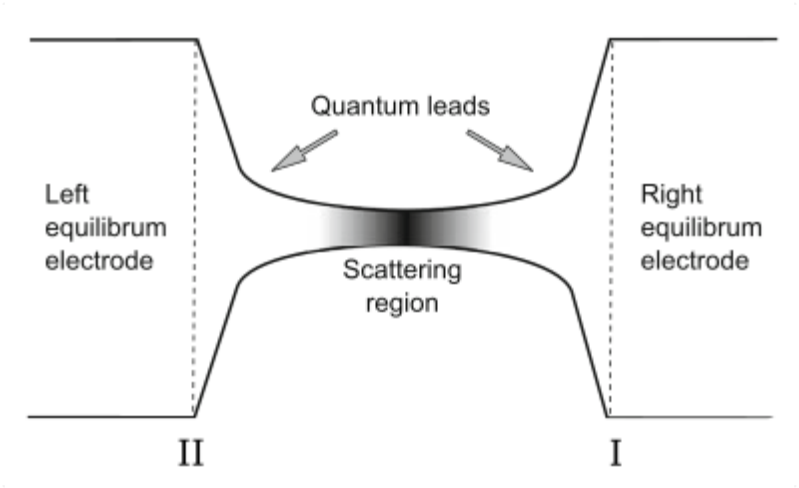


Figure 2.1: Schematic picture of a quantum junction: the scattering region is connected to the electrodes through the quantum leads. Figure adapted from [68].

Among the different methods available to calculate the transmission probability in quantum junctions, the transfer-matrix is one that stands out for its generality. Indeed, this method can be applied to analyze the propagation of waves across different interconnected regions, be they acoustic, electromagnetic, or matter waves. In the context of Quantum Mechanics, given the particle-wave duality, the analysis of electron transmission from one region to another translates into

[1] Noninteracting in the sense of not having any many-body interaction beyond the linear term. The concept of many-body interactions is discussed in chapter 3.

solving the time-independent Schrödinger wave equation:

$$\frac{-\hbar^2}{2m}\frac{d^2\Psi(x)}{dx^2} + V(x)\Psi(x) = E\Psi(x) \tag{2.2}$$

The wave description allows us to apply the transfer matrix method to calculate transport-related observables. This method consist essentially in defining the, so called, transfer matrix M capable of relating the wave function components from the two different regions. In the example of figure 2.1, the transfer matrix M connects the wave function defined in II to the wave function components defined in I:

$$\Psi_{II} = M_{II\leftarrow I}\Psi_I \tag{2.3}$$

In some sense, the transfer matrix directly codifies the effect of the potential of the region for which it's being calculated, into a transmission coefficient. The method is particularly effective for transport problems involving systems with many scattering centers, since it allows to calculate the transfer matrix of the entire system in terms of the transfer matrix of individual scatterers, which can usually be easily calculated. Indeed, from the definition (2.3) it's possible to see that the transfer matrix of such a system, depicted in figure 2.2, can be expressed in terms of the transfer matrix of the subsystems as:

$$M_{N\leftarrow 1} = M_{N\leftarrow(N-1)}...M_{3\leftarrow 2}M_{2\leftarrow 1} \tag{2.4}$$

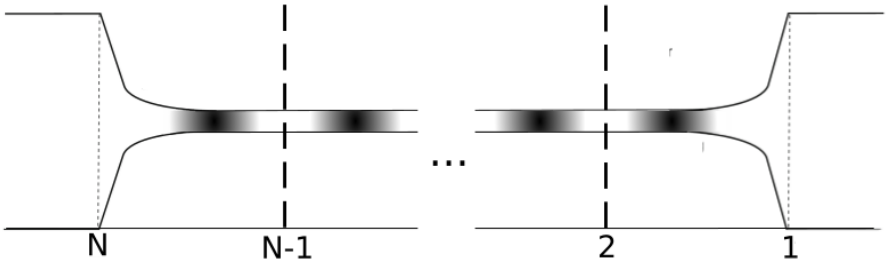


Figure 2.2: Schematic picture of a quantum junction composed of multiple individual scatters. The transfer matrix of the entire system can be calculated by the product of the transfer matrix of the individual scatters.

Despite being a relatively simple approach, the transfer matrix method is a powerful mathematical tool that can be used in the solution of modern problems in condensed matter physics. This will become more evident in the next section, where the transfer matrix method is going to be used to study the effect of local

magnetic moments in the conductivity of HgTe topological insulators.

2.3 2DTI Model and the Hyperfine Interaction

The modeling of type III HgTe semiconductor quantum well will follow the reference [69], in which it's presented how the variation of well length can induce the system to go through a topological phase transition. The major consequence of this transition is the formation of the topologically protected QSH edge states, indicating the system to be a 2DTI. In the particular case of the reference, the barriers of the quantum well were composed of CdTe, for which the relevant bands displays a progression such that the s-type Γ_6 band lies above the p-type Γ_8 in terms of energy. The HgTe, on the other hand, has a band ordering such that the p-type Γ_8 lies above the s-type Γ_6. The band progression of both CdTe and HgTe in Γ is shown in figure 2.3(a). As depicted in figure 2.3(b), this difference in the ordering is the key characteristics behind the phenomena of band inversion, the responsible for the topological phase transition.

In order to describe topological phase transition it's enought to consider the six bands $|\Gamma_6 + \frac{1}{2}\rangle, |\Gamma_6 - \frac{1}{2}\rangle, |\Gamma_8 + \frac{1}{2}\rangle, |\Gamma_8 - \frac{1}{2}\rangle, |\Gamma_8 + \frac{3}{2}\rangle, |\Gamma_8 - \frac{3}{2}\rangle$ of HgTe. When the effect of hibridization with the bars is taken into account, these bands mixture among themselves to form the spin up and spin down components of the bands E1, H1, and L1, also known as BHZ states. In the vicinity of the Dirac point the model can be further simplified to a four band description by neglecting the L1 band, whose energies are sufficiently separated from the E1 and H1 ones. In addition to that, the fact m_J is still a good quantum number in this regime must also be taken into consideration. This will lead to the following form for the bands E1 and H1:

$$|E+\rangle = f_{E\Gamma_6}(z)|\Gamma_6 + 1/2\rangle + f_{E\Gamma_8}(z)|\Gamma_8 + 1/2\rangle \tag{2.5}$$

$$|H+\rangle = f_H(z)|\Gamma_8 + 3/2\rangle \tag{2.6}$$

$$|E-\rangle = f_{E\Gamma_6}(z)|\Gamma_6 - 1/2\rangle + f_{E\Gamma_8}(z)|\Gamma_8 - 1/2\rangle \tag{2.7}$$

$$|H-\rangle = f_H(z)|\Gamma_8 - 3/2\rangle \tag{2.8}$$

An effective low-energy description can be achieved on the basis of general symmetry arguments and with the use of $k.p$ theory. The obtained Hamiltonian, also

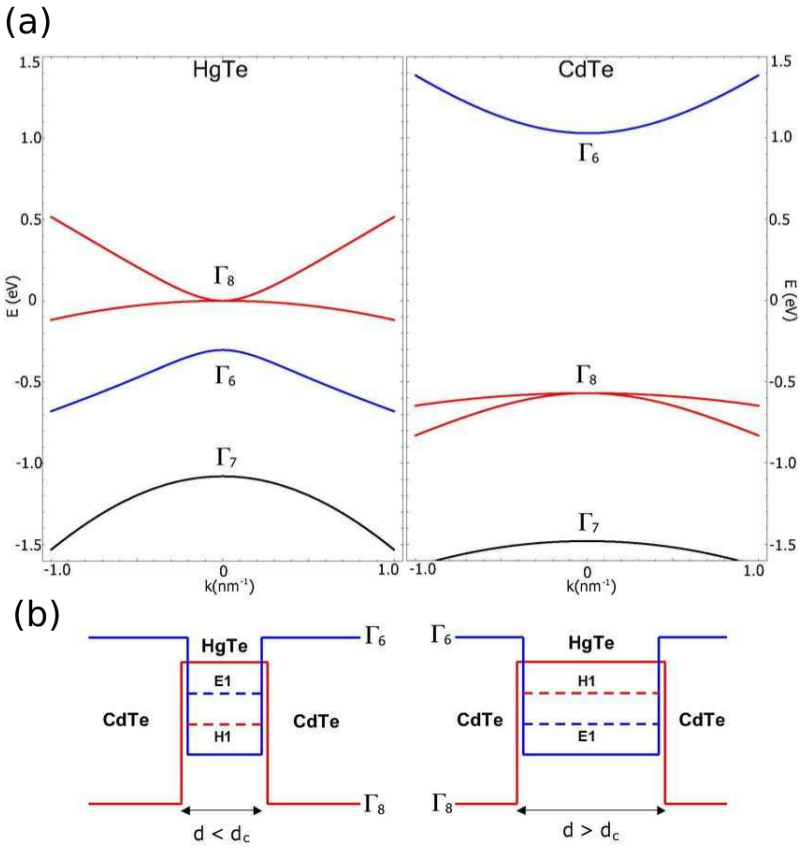


Figure 2.3: (a)Bulk energy bands of HgTe and CdTe near the G point. (b)The CdTe-HgTe-CdTe quantum well in the normal regime E1 > H1 with d < dc and in the inverted regime H1 > E1 with d > dc. In this and other figures, G8/H1 symmetry is indicated in red and G6/E1 symmetry is indicated in blue. Figure obtained from [70]

known as BHZ Hamiltonian, can be written in the basis $|E+\rangle, |H+\rangle, |E-\rangle, |H-\rangle$ as:

$$H_{BHZ} = \begin{pmatrix} H(k) & 0 \\ 0 & H(-k) \end{pmatrix} \tag{2.9}$$

with 0 being a 2x2 matrix and

$$H(k) = \begin{pmatrix} \epsilon_k + M_k & A(k_x + ik_y) \\ A(k_x - ik_y) & \varepsilon_k + M_k \end{pmatrix} \tag{2.10}$$

where $\varepsilon_k = -Dk^2$, $M_k = M_0 - Bk^2$ and $k = \sqrt{k_x^2 + k_y^2}$ and the parameters A, B, D and M_0 depends on the geometry of the quantum well.

The Hamiltonian of equation (2.9) describes a 2D quantum well for which periodic boundary conditions in both x and y directions are used. Since we are

interested in the effect of HF interaction in the transport properties of the helical edge states, its necessary to impose the proper boundary conditions leading to their formation. This task can be achieved by considering a semi-infinite plane (x>0) topological insulator, and, by introducing a confining potential $V(x)$ responsible to restrict the helical states to the edge x=0. In this case, the real space description of the Helical States located in the border of the semi-infinite plane is be given by

$$[H_{BHZ}(-i\partial_x, -i\partial_y) + V(x)]\Psi(x,y) = E\Psi(x,y). \tag{2.11}$$

Due to the periodic boundary conditions in the y direction, k_y is still a good quantum number, that leads equation (2.11) to have eigenstates of the form:

$$\Psi_{k_y}^{\uparrow(\downarrow)}(x,y) = \frac{1}{\sqrt{L_y}} e^{ik_y y} \eta_{k_y}^{\uparrow(\downarrow)}(x) \chi^{\uparrow(\downarrow)}, \tag{2.12}$$

where $\eta_{k_y}^{\uparrow(\downarrow)}$ is an envelope function in the x direction, χ is a four component spinor and the indices $\uparrow$ $(\downarrow)$ refers to the z-component of the total state's angular momentum, which includes contribution from both the intrinsic electron spin and the orbital angular momentum. The corresponding eigenergies are found to be

$$E_{k_y}^{\uparrow(\downarrow)} = E_0 + (-)\hbar v_0 k_y, \tag{2.13}$$

where $E_0 = -M_0 D/B$ and $v_0 = -\sqrt{B^2 - D^2}|A|/(\hbar B)$.

In order to account for the effect of hyperfine interactions in the topological edge states, the Dirac Equation can be used to extract the mathematical form of the hyperfine interaction between an electron of spin, $\mathbf{S}$, located at $\mathbf{r}$ and the n-th nuclear magnetic moment of the crystal, $\mathbf{I}_n$, located at $\mathbf{R}_n = (\mathbf{X}_n, \mathbf{Y}_n, \mathbf{Z}_n)$. The nuclear magnetic moments will be treated classically i.e. it's quantum dynamics will not be considered. This interaction can be calculated by three terms [71]

$$h_1^n = \frac{\mu_0}{4\pi}\frac{8\pi}{3}\gamma_e\gamma_{j_n}\delta(\mathbf{r}_n)\mathbf{S}.\mathbf{I}_n, \tag{2.14}$$

$$h_2^n = \frac{\mu_0}{4\pi}\gamma_e\gamma_{j_n}\frac{3(\mathbf{e}_n.\mathbf{S})(\mathbf{e}_n.\mathbf{I}_n) - (\mathbf{S}.\mathbf{I}_n)}{r_n^3(1+\frac{r_c}{r_n})}, \tag{2.15}$$

$$h_3^n = \frac{\mu_0}{4\pi}\gamma_e\gamma_{j_n}\frac{\mathbf{L}_n.\mathbf{I}_n}{r_n^3(1+\frac{r_c}{r_n})}. \tag{2.16}$$

where the vectors $\mathbf{r}_n = \mathbf{r} - \mathbf{R}_n$, $\mathbf{L}_n = \mathbf{r}_n$ x $\mathbf{p}$ corresponds respectively to relative position of the electron in relation to the nuclear momentum and to angular

momentum of the electron, also, $r_n = |\mathbf{r}_n|$ and $\mathbf{e}_n = \mathbf{r}_n / r_n$. The constants μ_0, r_c, γ_e and γ_j corresponds respectively the vacuum magnetic permeability, the nuclear radius and the giromagnetic ratio of the electron and the n-th nuclear spin, whose values can be found in [71]. Therefore the total HF hamiltonian is then:

$$H_{HF} = \sum_n h_1^n + \sum_n h_2^n + \sum_n h_3^n \tag{2.17}$$

Its important to observe that only a fraction of the atoms in the crystal of HgTe possess a non-zero nuclear magnetic moment, and therefore the sum in equation (2.17) is perfomed over a specific configuration of arrangement of the nuclear moments, which makes it a sample dependent model. Lunde and Platero [71] showed that it is possible to get a more general description of the system by taking the position average over all possible different values of $(\mathcal{X}_n, \mathcal{Z}_n)$, keeping fixed the direction of the magnetic moments. The $\mathcal{Y}_n$ component is also kept fixed in such a way to break the symmetry along the y direction. The final result can be written in the basis of eigenstates of equation (2.12) as:

$$\bar{H}_{HF} \approx \frac{1}{2\hbar} \sum_{n,k_y,k_y'} e^{i(k_y'-k_y)\mathcal{Y}_n} \left[\frac{A_{j_n}^z}{\rho_N} \eta_{k_y,k_y'} \mathbf{I}_{z,n} (c_{k_y,\uparrow}^\dagger c_{k_y',\uparrow} - c_{k_y,\downarrow}^\dagger c_{k_y',\downarrow}) \right.$$
$$\left. - \frac{A_{j_n}^\perp}{\rho_N} \eta_{k_y,-k_y'} (\mathbf{I}_{-,n} c_{k_y,\uparrow}^\dagger c_{k_y',\downarrow} + \mathbf{I}_{+,n} c_{k_y,\downarrow}^\dagger c_{k_y',\uparrow}) \right], \tag{2.18}$$

where $I_{\pm,n} = I_{x,n} \pm i I_{y,n}$ and,

$$\eta_{k_y,k_y'} = 1 - \frac{D^2[A^2 B + 2(B^2 - D^2)M_0]}{8BM_0^2(B^2 - D^2)} (k_y - k_y')^2. \tag{2.19}$$

Both the parallel and perpendicular coupling constants, $A_{j_n}^z$ and $A_{j_n}^\perp$, and the linear density of nuclear magnetic moments ρ_N emerge from the averaging process.

In order to proceed with our analysis, we considered the low energy regime, where the second order terms in momentum can be disconsidered. In this case the term $\eta_{k_y,k_y'}$ can be approximated by 1, and the hyperfine interaction Hamiltonian can be written as:

$$\bar{H}_{HF} \approx \frac{1}{2\hbar\rho_N} \sum_n \left[A_{j_n}^z \mathbf{I}_{z,n} (c_{\mathcal{Y}_n,\uparrow}^\dagger c_{\mathcal{Y}_n,\uparrow} - c_{\mathcal{Y}_n,\downarrow}^\dagger c_{\mathcal{Y}_n,\downarrow}) - A_{j_n}^\perp (\mathbf{I}_{-,n} c_{\mathcal{Y}_n,\uparrow}^\dagger c_{\mathcal{Y}_n,\downarrow} + \mathbf{I}_{+,n} c_{\mathcal{Y}_n,\downarrow}^\dagger c_{\mathcal{Y}_n,\uparrow}) \right] \tag{2.20}$$

Therefore, considering the basis of edge states, the BHZ Hamiltonian together with the HF interaction can be written in the position representation as

$$\left(1E_0 - \hbar v_0 \sigma_z i\partial_y + \sum_n \left[\frac{A^z_{j_n}}{2\hbar\rho}\sigma_z I_{z,n} - \frac{A^\perp_{j_n}}{2\hbar\rho}\sigma_x I_{x,n} - \frac{A^\perp_{j_n}}{2\hbar\rho}\sigma_{y,n} I_y\right]\delta(\mathcal{Y}_n)\right)\Psi = E\Psi \quad (2.21)$$

where $\boldsymbol{\sigma} = (\sigma_x, \sigma_y, \sigma_z)$ are the Pauli matrices. From Table 2.1 we can see that the values of the parameters $A^z_{j_n}$ and $A^\perp_{j_n}$ are relatively close to each other, having both the same order of magnitude. Regarding the quantitative results, we are mostly interested in the order of magnitude of the calculated quantities, therefore, for our purposes its enough to consider the approximation of isotropic coupling: $A^z_{j_n} \approx A^\perp_{j_n} = A_0$. This approximation leads to:

$$\bar{H}_{HF} = 1E_0 - \hbar v_0 \sigma_z i\partial_y + \frac{A_0}{2\hbar\rho_N}\sum_n \boldsymbol{\sigma}\cdot\mathbf{I}_n\delta(\mathcal{Y}_n), \quad (2.22)$$

As we can see, the averaging over $(\mathcal{X}_n, \mathcal{Z}_n)$ coordinates ultimately allows a one dimensional description of the edge states coupled with local magnetic moments.

2.4 Model Analysis

Before we study the general situation, let us obtain some insight by studying the single magnetic impurity case. For this simple case the Lippmann-Schwinger equation is analytically solvable [72, 73] and the transmission and reflection coefficients can be written in a closed form. Since we are not considering classical magnetic moments, we analyze the problem using the transfer matrix approach [74]. For a single-impurity, the Hamiltonian (2.22) in the position basis reads

$$\hat{H} = 1E_0 - \hbar v_0 i\partial_y \begin{pmatrix} 1 & 0 \\ 0 & -1 \end{pmatrix} + \frac{A_0|I|}{2\hbar\rho_N}\delta(y)\begin{pmatrix} \cos\theta & e^{-i\phi}\sin\theta \\ e^{i\phi}\sin\theta & -\cos\theta \end{pmatrix}. \quad (2.23)$$

From where θ and ϕ are respectively, the polar and azimuthal angles of the magnetic moment, as depicted in figure 2.4. In appendix B is presented the calculation

of the transfer matrix associated to this model, which corresponds to

$$M_\delta = e^{i\alpha}\begin{pmatrix} \cosh(\beta) & ie^{-i\phi}\sinh(\beta) \\ -ie^{i\phi}\sinh(\beta) & \cosh(\beta) \end{pmatrix} \qquad \alpha = -\Lambda\cos(\theta),\ \beta = -\Lambda\sin(\theta), \tag{2.24}$$

and $\Lambda = A_0|I|/2\hbar^2\rho_N v_0$. The transmission coeffiecient can be calculated by

$$T_\delta = \frac{1}{|[M_\delta]_{11}|^2} = sech^2(\beta) \tag{2.25}$$

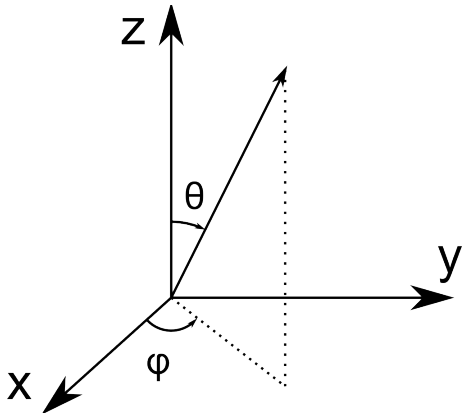


Figure 2.4: Schematic picture showing the polar and azimunthal angles θ and ϕ defined by the local magnetic moment.

Here its possible to observe that the transmission coefficient does not depend on the momentum, a result very different that the obtained for a non-topological quantum well. The generalization to the many impurity case (2.22) can be found by considering the product of a chain of transfer matrices

$$M = M_{\delta_N} M_{0_{N-1}} ... M_{\delta_2} M_{0_1} M_{\delta_1} \tag{2.26}$$

where $y_N > y_{N-1} > ... > y_2 > y_1$ and M_{0_n} is the transfer matrix associated with the free propagation between the n-th and (n+1)-th magnetic moment, wich is given by

$$M_{0_n} = \begin{pmatrix} e^{ik(y_{n+1}-y_n)} & 0 \\ 0 & e^{-ik(y_{n+1}-y_n)} \end{pmatrix} \tag{2.27}$$

Further insight into the problem can be obtained by analyzing the product

$M_{\delta_{n+1}} M_0 M_{\delta_n}$, which can be written as

$$\cos(k(\mathcal{Y}_{n+1}-\mathcal{Y}_n)-\Delta_n^-/2)e^{i(\alpha_n+\alpha_{n+1})}\begin{pmatrix} e^{i\Delta_n^-/2}\cosh(\beta_n+\beta_{n+1}) & ie^{-i\Delta_n^+/2}\sinh(\beta_n+\beta_{n+1}) \\ -ie^{i\Delta_n^+/2}\sinh(\beta_n+\beta_{n+1}) & e^{-i\Delta_n^-}\cosh(\beta_n+\beta_{n+1}) \end{pmatrix}$$
$$+i\sin(k(\mathcal{Y}_{n+1}-\mathcal{Y}_n)-\Delta_n^-/2)e^{i(\alpha_{n+1}+\alpha_n)}\begin{pmatrix} e^{i\Delta_n^-/2}\cosh(\beta_n-\beta_{n+1}) & ie^{-i\Delta_n^+/2}\sinh(\beta_n-\beta_{n+1}) \\ ie^{i\Delta_n^+/2}\sinh(\beta_n-\beta_{n+1}) & e^{-i\Delta_n^-}\cosh(\beta_n-\beta_{n+1}) \end{pmatrix} \tag{2.28}$$

Where is defined $\Delta_n^- = \phi_n - \phi_{n+1}$ and $\Delta_n^+ = \phi_n + \phi_{n+1}$. Now observe that, considering the Hamiltonian (2.22), for any realistic system we expect the existence of disorder in both the polar and azimunthal angles θ and ϕ as well as in the positions $\mathcal{Y}_n$. However, from equation (2.28) it is possible to see that, since the term $\mathcal{Y}_{n+1} - \mathcal{Y}_n$ always appears accompanied by the term $\phi_{n+1} - \phi_n$, the effect of disorder in $\mathcal{Y}_n$ is redundant to the presence of disorder in ϕ_n. This observation allows us to simplify the problem by neglecting the disorder in the positions. In fact, the transfer matrix (2.26) can be simplified by replacing all the terms $\mathcal{Y}_{n+1} - \mathcal{Y}_n$ by the average distance l.

2.5 Anomalous Localization

With the assitance of equation (2.26) the average transmission was numerically calculated for different values of the dimensionless momentum kl using $2x10^5$ different random configurations. In figure 2.5a is presented calculations performed for the systems sizes N=100, N=200 and parameters $\Lambda = 0.2$, and $\Lambda = 0.3$. From this plot we can draw two intuitive conclusions: the average transmission tends to decrease by increasing the size of the system or the coupling constant. A less intuitive observation is that, as in the case of a single impurity, the average transmission is independent of the dimensionless momentum kl. Despite simple this, result gives basis to idea that, even being weak, the hyperfine interaction can be the responsible for suppression of the conductance of edge states provided

there are enough scatters.

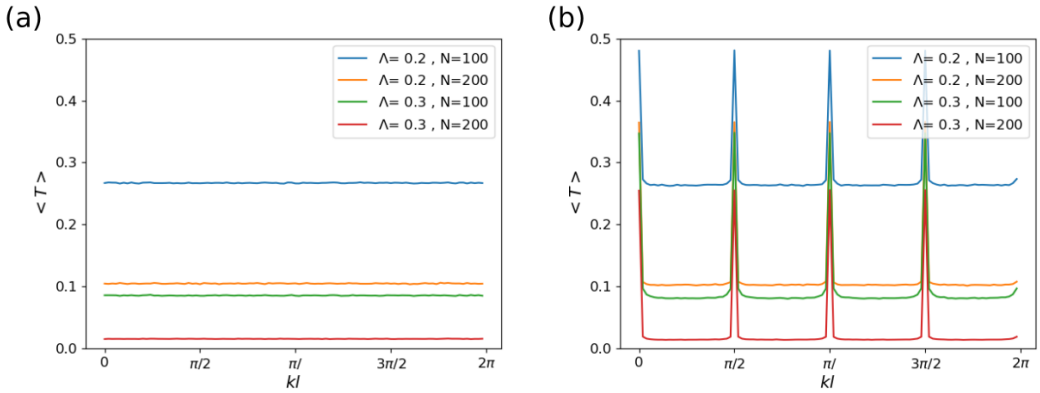


Figure 2.5: (a) Average transmission calculated in the presence of disorder in both the polar, θ_n, and azimunthal ϕ_n angles. (b) Average transmission calculated in the presence of disorder in the polar angle but keeping the azimunthal angle fixed $\phi_n = 0$. The average transmission is numerically equivalent in both cases with exception to the values of momentum where $kl = n\pi/2$, $n \in \mathcal{N}$. The numerical calculations were performed using $2x10^5$ different random configurations of magnetic moments.

A deeper understanding of the system can be obtained by comparing the two plots in figure 2.5. Its possible to observe that in the plot 2.5b, where the average transmission was calculated using a constant value for $\phi_n = 0$, the average transmission assumes the same value as in the case of disordered ϕ_n, figure 2.5a, except when the dimensionless momentum assumes a value of an integer multiple of $\pi/2$. This observation shows that, regarding the average transmission, the component of the local magnetic moment in the direction of the propagating modes can be neglected without any loss of generality, allowing a further simplification of the Hamiltonian (2.22) and therefore the associated transfer matrix, for which expression (2.28) becomes

$$M_{\delta_{n+1}} M_0 M_{\delta_n} = \cos(kl) M_{\delta_n+\delta_{n+1}} + i\sin(kl) e^{i(\alpha_n+\alpha_{n+1})} \begin{pmatrix} \cosh(\beta_n-\beta_{n+1}) & i\sinh(\beta_n-\beta_{n+1}) \\ i\sinh(\beta_n-\beta_{n+1}) & \cosh(\beta_n-\beta_{n+1}) \end{pmatrix} \quad (2.29)$$

This equation can be recurrently used to obtain an expression for the element M_{11}

of the product chain of matrices (2.26):

$$M_{11} = e^{i\sum_n \alpha_n} \sum_{n=0}^{N-1} [\cos(kl)]^{N-1-n} [i\sin(kl)]^n \sum_{C_n} \cosh(\beta_N + B_n) \tag{2.30}$$

where B_n is a given combination of n subtractions and $N-1-n$ summations of the remaining β_i parameters. C_n is the set of all possible combinations B_n.

As long as kl differs from a integer multiple of $\pi/2$, the previous expression is, up to a global phase, numerically equivalent to the most general case of disorder in ϕ_n. In the case where kl is a multiple integer of $\pi/2$ the peaks in the average transmission can be undertood on the basis that most of the terms of M_{11} vanish in this regime, thus minimizing its module and maximizing the transmission. Indeed, M_{11} simplyfies to $M_{11} = e^{i\sum_n \alpha_n} \cosh(\beta_N + B_0)$ for an even multiple of $\pi/2$ and to $M_{11} = e^{i\sum_n \alpha_n} \cosh(\beta_N + B_{N-1})$ for an odd mutiple of $\pi/2$, leading to a transmission given by

$$\sin(kl) = 0 \rightarrow T_{\phi=cte} = \cosh^{-2}(\beta_1 + \beta_2 + ... + \beta_{N-1} + \beta_N) \tag{2.31}$$

$$\cos(kl) = 0 \rightarrow T_{\phi=cte} = \cosh^{-2}(\beta_1 + \beta_2 + ... + \beta_{N-1} - \beta_N) \tag{2.32}$$

It is possible to observe that in this regime the effect of the many impurities can be accounted for as the effect of a single impurity where the parameter which goes into the expression is given by the sum of the parameters of every single scatter. A more detailed analysis can be obtained by employing the Central Limit Theorem, which allows to define the probability distribution that the sum of parameters $\beta_N + B_0$ and $\beta_N + B_{N-1}$ assumes a certain value. These two terms will effectively lead to the same transmission, therefore it is enough to focus in $\beta_N + B_0$, for which the probability distribution will be Gaussian with mean and standard deviations given respectively by:

$$\langle \beta_1 + \beta_2 + ... + \beta_N \rangle = -\Lambda N \langle \sin(\theta) \rangle = 0, \tag{2.33}$$

$$\sigma_{SD}(\beta_1 + \beta_2 + ... + \beta_N) = \Lambda\sqrt{N/2}. \tag{2.34}$$

The average transmission can then be calculated as

$$\langle T \rangle_{N>>1} = \int_{-\Lambda N}^{\Lambda N} P_{\beta_1+\beta_2+...+\beta_N}(s)\, \mathrm{sech}^2(s) ds \approx \frac{2}{\sqrt{\Lambda^2 N \pi}} \tanh\left(\frac{\sqrt{\Lambda^2 N}}{4\pi}\right) \approx \frac{2}{\sqrt{\Lambda^2 N \pi}} \tag{2.35}$$

Where $P_{\beta_1+\beta_2+...+\beta_N}(s)$ is the normal distribution giving the probability that the sum $\beta_1 + \beta_2 + ... + \beta_N$ assumes a value s. This analysis is confirmed by the plots presented in Fig. 2.6, where the behavior of the average transmission with system size is studied for the cases of $\Lambda = 1$ and $\Lambda = 2$, and the analytical expression (2.35) is compared with the results of numerical calculations.

As stated before, its possible to observe a decrease in the average transmission with the increase of the systems size, a behavior that signals to the occurrence of localization due to disorder, however, as we can see from equation (2.35) , the behavior of the drop in transmission strongly differs from the exponential decay proposed by Anderson. This type of decay, also known as anomalous localization, has already been observed in other systems and its usually related to the low energy behavior of systems with non-diagonal disorder. [5, 6, 7, 75, 76]

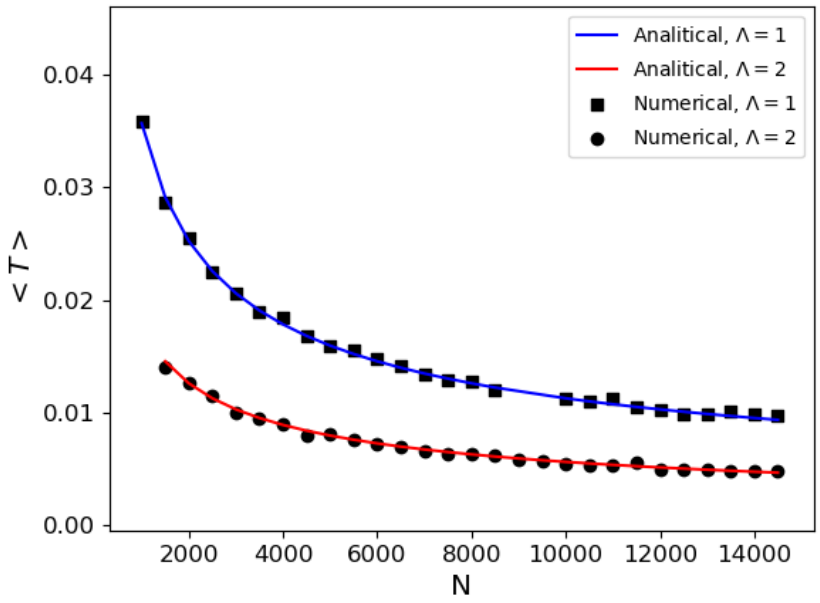


Figure 2.6: Anomalous decay of the average transmission with the number of scatters. It's possible to observe the good agreement between the analytical prediction and the numerical results. This non-exponential decay is only observed in the absence of disorder in the azimuthal angles of the magnetic moments and for particular values of the dimensionless momenta kl, when it equates to an integer multiple of $\pi/2$.

The analytical description of the average transmission provided by (2.35) only applies to specific values of momentum and can not be extended to the general case of disorder in ϕ_n. A quantitative description of this general case is of upmost

importance since the results obtained for this regime can be contrasted with experimental values. An important step in this direction can be obtained by considering the small coupling limit, $\Lambda \to 0$, of equation (2.30):

$$M_{11} \approx M_0 + e^{i\sum_n \alpha_n} \sum_{n=0}^{N-1} [\cos(kl)]^{N-1-n} [i\sin(kl)]^n \sum_{C_n} \frac{(\beta_N + B_n)^2}{2} \tag{2.36}$$

where were considered only terms up to second order in Λ, and

$$M_0 = M_{11}(\Lambda = 0) = \sum_{n=0}^{N-1} [\cos(kl)]^{N-1-n} [i\sin(kl)]^n \begin{pmatrix} N-1 \\ n \end{pmatrix} = (\cos(kl) + i\sin(kl))^{N-1} = e^{ikl(N-1)} \tag{2.37}$$

The transmission in this regime will be give by

$$T \approx 1 - Re\Big\{ M_0^* \sum_{n=0}^{N-1} [\cos(kl)]^{N-1-n} [i\sin(kl)]^n \sum_{C_n} (\beta_N + B_0)^2 \Big\} \tag{2.38}$$

which leads to the average transmission up to second order in Λ:

$$\langle T \rangle \approx 1 - \langle (\beta_N + \beta_{N-1} + ... + \beta_1)^2 \rangle \tag{2.39}$$

$$\approx 1 - \frac{\Lambda^2 N}{2} \tag{2.40}$$

The importance of this expression lies in the fact that it is valid for the most general case of disorder in both the polar angles and the positions of the local magnetic moment, a situation that is usually met in experimental devices.

By looking at (2.35) and (2.39) it is possible to observe that the dependence of the average transmission in the parameters Λ and N follows a rule:

$$\langle T \rangle (\Lambda, N) \equiv \langle T \rangle (\Lambda^2 N). \tag{2.41}$$

This constraint in the dependence of parameters strongly simplify the problem and, despite being shown for these particular cases, it can also be numerically confirmed for the most general case of finite coupling as is shown in Fig. (2.7).

Another insight into the general case can be obtained by observing that in equation (2.30) there are terms with all possible combinations of signs in the arguments of the hyperbolic cosine, therefore, there will be a term of highest

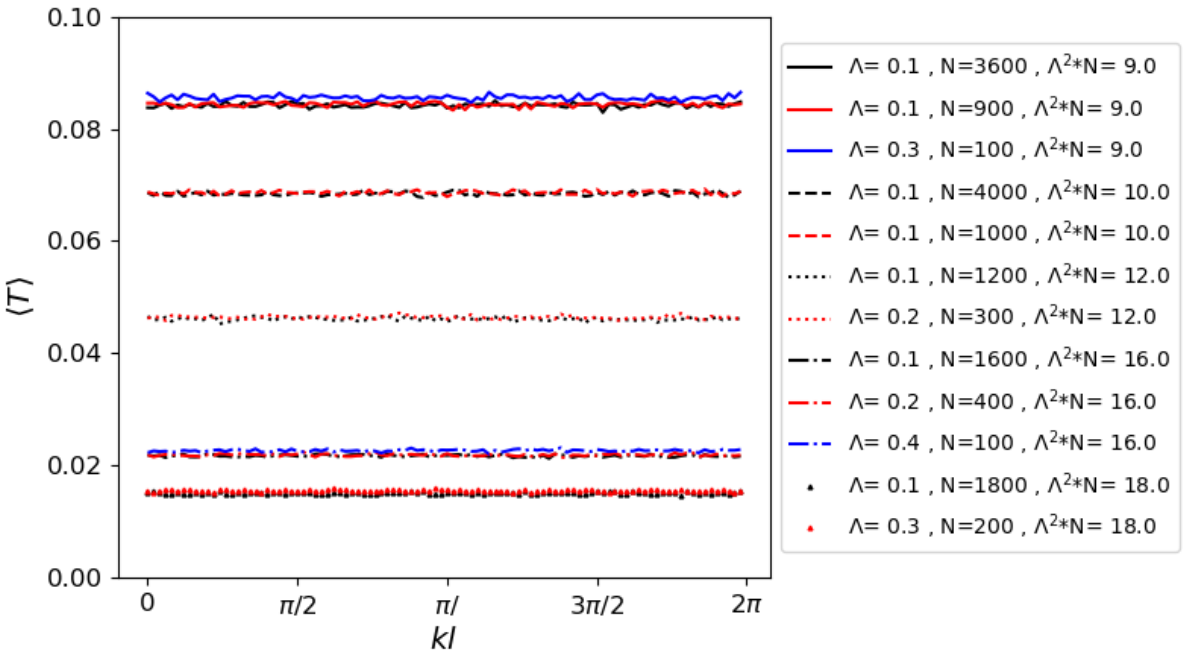


Figure 2.7: Plot of the average transmission for different values of $\Lambda^2 N$ using different combinations of Λ and N. The plot shows a constraint in the dependence of the average transmission on the variables Λ and N, such that $\langle T\rangle(\Lambda, N) \equiv \langle T\rangle(\Lambda^2 N)$.

value for which the argument of the hyperbolic cosine will be $|B| = |\beta_1| + |\beta_2| ... + |\beta_N|$. Together with the observation of momentum invariance of the average transmission, this analysis allows we to define a superior limit for the module of M_{11}: choosing $kl = \pi/4$, (2.30) becomes:

$$M_{11} = \frac{1}{2^{(N-1)/2}} \sum_{n=0}^{N-1} i^n \sum_{C_n} \cosh(\beta_N + B_n) \tag{2.42}$$

By replacing all the hyperbolic cosines by $\cosh(|B|)$ we get

$$|M_{11}| < \left| \frac{\cosh(|B|)}{2^{(N-1)/2}} \sum_{n=0}^{N-1} i^n \begin{pmatrix} N-1 \\ n \end{pmatrix} \right| = \left| \frac{\cosh(|B|)}{2^{(N-1)/2}} (i+1)^{N-1} \right| = \cosh(|B|) \tag{2.43}$$

Similarly to the calculation of equation (2.35), the inequality in equation (2.43) can be used to define an inferior limit for the average transmission. This inferior limit can be calculated by observing that, by the Central Limit Theorem, the probability of $|B|$ to assume a certain value will be given by a normal distribu-

tion with mean $\langle|B|\rangle = \Lambda N\langle|\sin(\theta)|\rangle$ and standard deviation(width) $\sigma_{SD}(|B|) = \Lambda\sqrt{N}\sigma_{sd}(|\sin(\theta)|)$. Therefore, it is possible to write for the average transmission:

$$\langle T\rangle_{N>>1} > \int_0^{\Lambda N} P_{|B|}(s)\,\mathrm{sech}^2(s)ds > \frac{1}{\sigma_{SD}(|B|)\sqrt{2\pi}}\tanh(x)\Big|_{\langle|B|\rangle-\sigma_{SD}(|B|)}^{\langle|B|\rangle+\sigma_{SD}(|B|)}$$
$$\approx \frac{2exp\{2(\sigma_{SD}(|B|) - \langle|B|\rangle)\}}{\sigma_{SD}(|B|)\sqrt{2\pi}} \quad (2.44)$$

Where $P_{|B|}(s)$ is the normal distribution giving the probability that the sum $|B| = |\beta_1| + |\beta_2| + ... + |\beta_N|$ assumes a value s. Its possible to see that there are two main contributions to the lower limit in (2.44): One which depends on the exponential of N, and another that depends on the exponential of $\sqrt{N}$. The firt one can be associated to the exponetial decay in the phenomena of Anderson localization and it originates from fact that the average value of the argument of cosh, $\langle|B|\rangle$, is proportional to N. The second represent an anomalous effect and is a direct consequence of the large fluctuations in $\langle|B|\rangle$, for which the stantadard deviations grows proportionally to $\sqrt{N}$.

Being an inequality, equation (2.44) doesn't allow us to directly calculate the value of $\langle T\rangle$, however it gives an important insight into the behavior of this quantity. One might be tempted to assume an exponential decay of the average transmission on the number of scatters, just as in the case of Anderson localization which is observed for several quantum systems, however, as was used in the deduction of equation (2.44), $\cosh(|B|)$ is the highest and most relevant term in equation (2.30). Therefore, even without replacing all the $\cosh(\beta_N + B_n)$ by $\cosh(|B|)$ we can expect a similar behavior for $\langle T\rangle$: having an Anderson-localization-like exponential decay in N and an anomalous exponential decay in $\sqrt{N}$,

$$\langle T\rangle(\Lambda^2 N) \propto e^{\gamma_1\Lambda^2 N + \gamma_2\Lambda\sqrt{N}} \quad (2.45)$$

where γ_1 and γ_2 are constants to be determined, and the dependence on Λ is already fixed by the relation $\langle T\rangle(\Lambda, N) \equiv \langle T\rangle(\Lambda^2 N)$. This result is supported by numerical calculations. Indeed, in figure (2.8) we presented a plot of $Log(\langle T\rangle)X\sqrt{N}$ where, for an exponential decay, a quadratic decrease of $Log(\langle T\rangle)$ in $\sqrt{N}$ is expected. However, it is possible to see that the numerical results (scattered points) can't be solely described by a quadratic term (blue curve) and need an extra term linear in $\sqrt{N}$ (red curve) for a proper fitting.

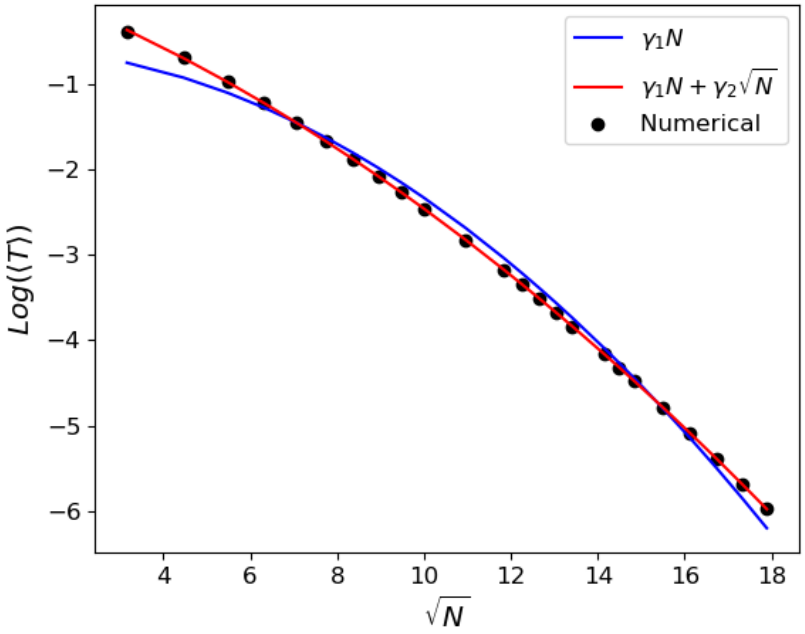


Figure 2.8: $Log\langle T\rangle$ (scatter plot) can not be properly described by a curve proportional to the number of scatters (blue curve), it needs an extra term proportional to $\sqrt{N}$ (red curve) for a proper fitting.

This result is of utmost importance since it shows the coexistence of two different regimes of localization: one in which the average transmission decays exponentially with the number of scatters, similar to the Anderson localization, and an anomalous one in which there is an exponential decay in $\sqrt{N}$. This type of anomalous localization has already been observed in other systems [5, 6, 7] and, similarly to the problem tackled in this work in which the term responsible for the anomalous behavior emerges as a consequence of the fluctuations in $|B|$, these systems are also characterized by parameters displaying large fluctuations.

Similarly to the phenomena of Anderson localization, it is also possible to define the localization length for the anomalous regime. This can be achieved by writing the average transmission in terms of the length of the system as:

$$\langle T\rangle(\Lambda^2 L) \propto e^{L(\gamma_1\Lambda^2 N/L)+\sqrt{L}(\gamma_2\Lambda\sqrt{N/L})} = e^{L/\xi_S+\sqrt{L/\xi_A}} \tag{2.46}$$

where we define the standard and the anomalous localization lengths, give respecvely by

$$\xi_S = \frac{1}{\gamma_1\Lambda^2\rho_S} \tag{2.47}$$

$$\xi_A = \frac{1}{\gamma_2^2 \Lambda^2 \rho_S} \tag{2.48}$$

In order to complete the description of the general case the constants γ_1 and γ_2 must be determined. This can be achieved by numerically analyzing the coefficients of the quadratic curve $Log(\langle T \rangle) \text{x} \sqrt{N}$ considering different values of Λ. In figure 2.9 we present the result of these calculations. In the upper panel we show the coefficient of the term proportional to N for different values of Λ while in the lower panel we present the plot of the coefficient of the term proportional to $\sqrt{N}$ for different values of Λ. As expected, the coefficient of N has a quadratic dependence on Λ, while the coefficient of $\sqrt{N}$ has a linear dependence. The parameters γ_1 and γ_2 can the be calculated from the fittings (solid curves), from which we obtained $\gamma_1 = -0.10$ and $\gamma_2 = -0.63$.

So far the two opposite regimes of transmission approaching unity ($\Lambda^2 N << 1$) and approaching zero ($\Lambda^2 N >> 1$) have been described. To derive an analytical description of the intermediary regime is a challanging task. Instead, we can describe it with the aid numerical calculations. In figure 2.10 the behavior of the average transmission for different values of $\Lambda^2 N$ is shown. This plot allows us to numerically describe the average transmission in the entire phase-space of the model (2.22). Interestingly, the expression (2.45) can also be used to fit the intermediary behavior of $\langle T \rangle$, but with different values for the parameters γ_1 and γ_2.

2.6 Contact to experiments - hyperfine interaction

Having outlined the localization properties of the model describing a 2DTI, its now possible to calculate length scale to which conductance is suppressed by scatterings with nuclear spins. In order to calculate the Anderson and anomalous localization lengths, its going to be used the parameters provided in [63], according to which $A = 3.65, B = -68.6eV^2, D = -51.2eV^2, M_0 = -0.010eV$ and $\rho_N \approx 10^7/\mu m, \rho_S \approx 2\text{x}10^6/\mu m$. In table 2.1 the intensity of the hyperfine interaction is shown together with spin and the observed proportion for each magnetic isotope of Hg and Te. Using these values, the kinetic parameter can be calculated to be $\hbar\nu_0 = 2.42eV$ while the average spin and average intensity of the hyperfine interaction can be calculated to be $I = 0.842\hbar$ and $A_0 = 3.51\text{x}10^{-6}eV$ respectively. By its turn, these values provide $\Lambda = 1.2\text{x}10^{-9}$, which can then be used in equations (2.47)

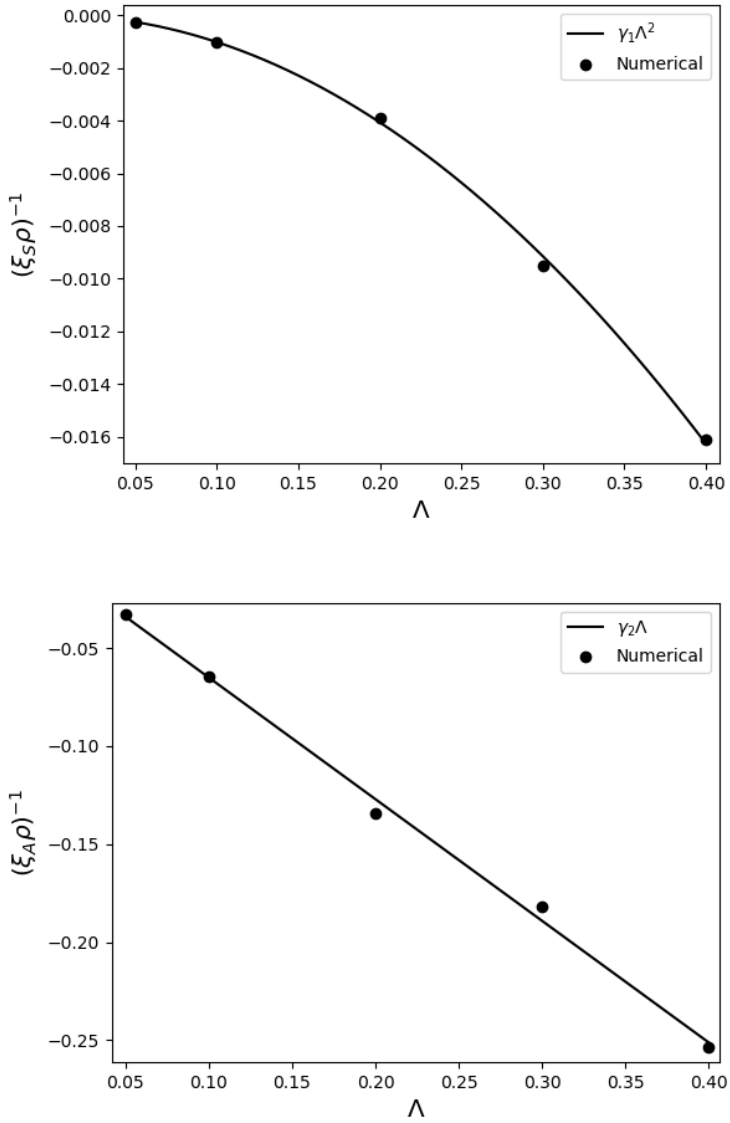


Figure 2.9: Plots of the coefficients of the terms N and $\sqrt{N}$ in $Log\langle T\rangle$ for different values of Λ. In the upper panel is presented the plot corresponding to the coefficient of the term proportional to N, which according to (2.45) is of the form $\gamma_1\Lambda^2$. In the lower panel is presented the plot corresponding to the coefficient of the term proportional to $\sqrt{N}$, which according to (2.45) is of the form $\gamma_2\Lambda\sqrt{N}$.

and (2.48) to obtain $\xi_S = 3.47\text{x}10^4 m$ and $\xi_A = 1.14\text{x}10^4 m$.

As we can see the coupling constant with the nuclear spins is approximately 10^9 times greater than the constant associated with the kinetic term $\hbar v_0$ which translates into large localization length. In fact, the calculated localization lengths of $\approx 10^4 m$ surpasses by 10 orders of magnitude what is experimentally observed

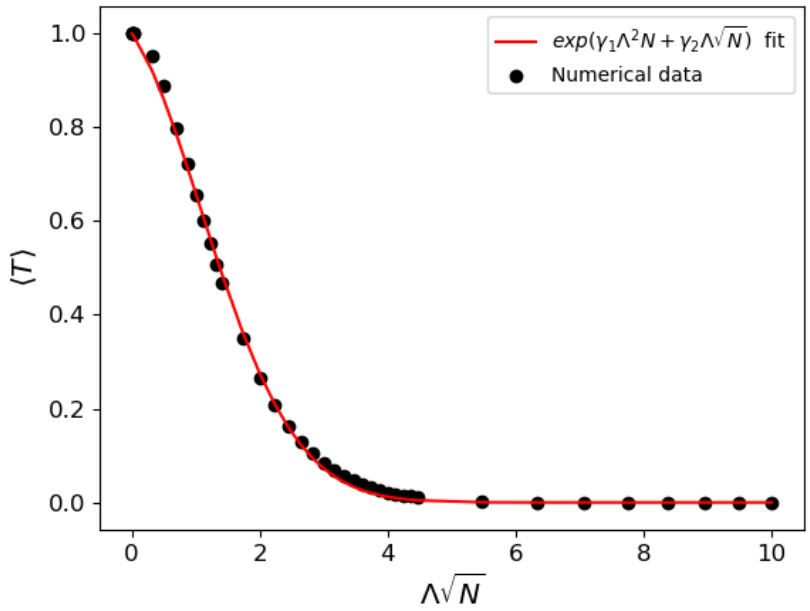


Figure 2.10: Average transmission calculated for different values of $\Lambda\sqrt{N}$ (scatter plot). Since the average transmission depends solely uppon Λ and N, this plot defines the average transmission for the entire phase-space of the model. Observe that, interestingly, the average transmission for the intermediary regime can also be described (2.45) (red plot), but with the parameters γ_1 and γ_2 assuming the values -0.22 and -0.18 respectively. This plot was generated by calculating the average transmission for a system 1000 impurities using different values of Λ .

[44, 53, 54], which indicates that, despite being a valid mechanism of suppression, the hyperfine interaction, by itself, is just too small to explain the deviations of quantum of conductance observed in 2DTI. Although, it's important to point out that here the directions of the nuclear spins were considered to be random and that the final result could have been different if some degree of ordering were considered for the nuclear spins.

2.7 Supression in the conductivity due to Mn magnetic impurities

The effect of locally breaking time reversal symmetry has also been reported in the context of HgTe topological insulators doped with Mn impurities [32]. In

Table 2.1: Estimates of the effective hyperfine couplings between helical edge states and the different isotopes present in HgTe. It is also shown their respective concentration and spin. Values extracted from [63]

Isotope	^{199}Hg	^{201}Hg	^{123}Te	^{125}Te
Prop.	17%	13%	1%	7%
Spin	1/2	3/2	1/2	1/2
$A_{jn}^{Z}(\mu eV)$	1.1	-0.38	-12	-14
$A_{jn}^{\perp}(\mu eV)$	0.30	-0.11	-3.5	-4.2

this case, time reversal symmetry is locally broken by the local magnetic moments of the Mn impurities, which can be responsible for spin-flipping scattering processes. This system has been reported to exhibit different regimes: at sufficiently low temperatures, the average conductance approaches the quantized value $\mathcal{G}_0$, indicating the absence of scatterings As the temperature increases above a certain value, a decrease in the conductance is observed. This result has been interpreted as a manifestation of the Kondo effect. At sufficiently low temperatures, the magnetic moments of the Mn impurities are completely screened by the surrounding electrons. As the temperature increases above the so-called Kondo temperature, the screening effect would disappear, allowing spin-flipping scatterings to occur. The experimental curve supporting these assertions is presented in the figure 2.11c, showing a plot of average conductance for different temperatures. The average conductance, denoted as G_{av}, was calculated by averaging the conductance over energies within the bulk band gap (inset), an energy interval where the contribution comes solely from the edge states. From this figure, it's also possible to see that as the temperature increases beyond T_K, which was estimated to be $T_K \approx 3K$ for this experiment, the conductance reaches a minimum. Afterward, it slowly increases with temperature before a rapid rise takes place. The regime of rapid increasce happens at a temperature T $15K$ and can be explained on the basis of thermal activation of the bulk band states, which can be estimated by $\propto exp(-E_g/2k_BT)$, depicted by the gray dashed line.

The same experiment leading to Fig 2.11 when performed in the absense of Mn impurities results in a flat average conductance $\mathcal{G}_0$ up to the temperature of $15K$, further indicating that the minimum observed is a direct consequence of the effects of Mn impurities. Assuming the minimum to be a consequence of the backscatterings between the electrons of the edge states and the Mn magnetic impurities, we are going to apply the previously described methodology to quantitatively de-

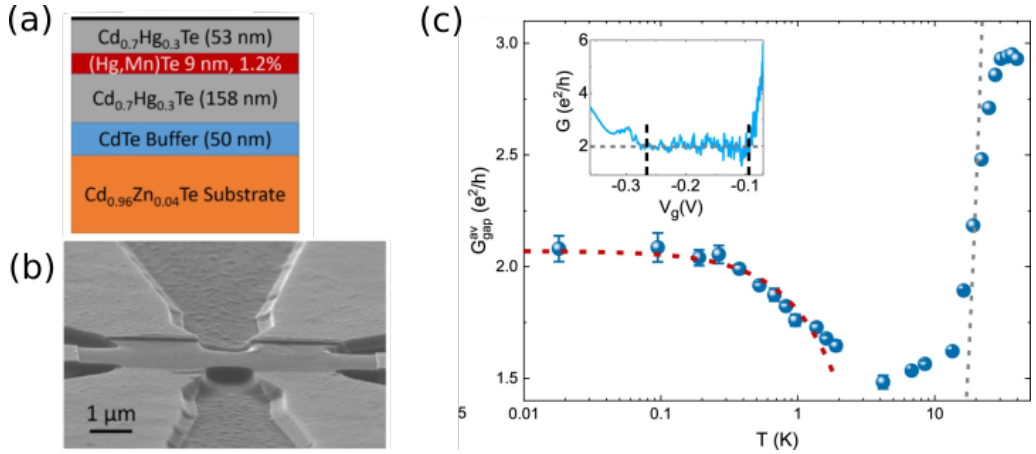


Figure 2.11: (a) Schematic of the layer stack showing the (Hg,Mn)Te quantum well sandwiched between two $Cd_{0.7}Hg_{0.3}Te$ barriers on a $Cd_{0.96}Zn_{0.04}Te$ substrate. (b) Scanning electron micrograph of a typical Hall bar used for measurements. (c) The average conductance in the quantum spin hall regime G^{av}_{gap} as a function of temperature T. The blue points are the experimental data and the red dashed line shows the power-law Kondo fit. The gray dashed line shows the expected thermally activated conductance [$\propto exp(-E_g/2k_bT)$] for a band gap of $E_g = 10meV$. The inset shows a typical G-V_g dependence from which G^{av}_{gap} (shown by dashed horizontal line) is calculated by averagin over the conductance values in the plateau region between the dashed vertical lines. The average conductance displays a minimum value of 1.483 $\mathcal{G}_0$ (0.741 $\mathcal{G}_0$ per channel) at the temperature of 4.2K. Figure adapted from [32]

.

scribe the systems transport properties. At the level of modeling, we will consider the exchange interaction between the electrons spin and the Mn magnetic moment proposed by [27], according to whom the interaction Hamiltonian is given by

$$H_{int} = \frac{1}{2\nu}\mathcal{J}_{ij}I_i\sigma_j\delta(y - y_0) \tag{2.49}$$

where $\mathcal{J}$ is the dimensionless matrix of coupling constants given by

$$\mathcal{J} = \frac{2\nu}{\xi}e^{-2|x_0|/\xi}\begin{pmatrix} J_m & 0 & 2J_0 \\ 0 & J_m & 0 \\ 0 & 0 & J_z \end{pmatrix} \tag{2.50}$$

Where $\nu = 1/(2\pi\hbar v_0)$ and ξ denotes the characteristic width of the edge states. As we can see, in the homogeneous case, this Hamiltonian is the same as (2.23) with the exception of an extra term proportional to $\mathbf{I}_x\sigma_z$, which we are going to

dismiss in this analysis. For a (001) CdTe/HgTe/CdTe QW with width close to the critical one, the exchange couplings $|J_m|$, $|J_z|$ and $|J_0|$ were estimated to be of the order of 0.1 $eV.nm^2$. Considering the estimates $\nu \simeq 0.5eV^{-1}nm^{-1}$ and $\xi \simeq 40nm$, a dimensionless constant $\mathcal{J}_{ij}$ of the order of 10^{-3} was obtained by [27], which leads to $\Lambda \approx \pi.10^{-3}$. Together with the atomic linear density of $10^7 atoms/\mu m$ provided by [63] and considering the concentration of 1.2% Mn atoms among Hg used in the experiment [32], the localization lengths can be readily calculated:

$$\xi_S = \frac{1}{\gamma_1 \Lambda^2 \rho_S} \approx 17\mu m \tag{2.51}$$

$$\xi_A = \frac{1}{\gamma_2^2 \Lambda^2 \rho_S} \approx 4.2\mu m \tag{2.52}$$

It is interesting to note that, with these parameter values, at an Mn concentration of 2.7%, the predicted anomalous localization length is $1.9\mu m$, which matches the length of the device used in the experiment. This result suggests the potential for constructing devices operating in the anomalous localization regime, thereby opening the door to experimental studies of anomalous localization phenomena.

In addition to the localization lenghts we can calculate the expected average conductance by calculating the number of impurities across the edge state, given by $N = \rho_S L$, being L the systems length. With this value we can calculate $\Lambda\sqrt{N} = 1,05$ which, according to plot presented in figure 2.10 leads to an average transmission of $\langle T \rangle = 0.63$. This value corresponds to the transmission per channel, therefore, the predicted conductance for two helical edge states will be $1.26(e^2/h)$. This result is shows an outstanding agreement with the experimentally observed value of $1.48(e^2/h)$, $0.741(e^2/h)$ per channel, presented in figure 2.11.

2.8 Conclusions

In summary, using the method of transfer matrix, a quantitative analysis of the effect of magnetic moments in the electronic transport properties of 2DTI was performed. The numerical calculations showed that the interaction with magnetic moments can indeed lead to a suppression of the conductance of the, otherwise, topologically protected states. Two different transport regimes were identified: one that was characterized by keeping the azimunthal angle of the magnetic moment fixed while having the polar angle disordered, and other in which we considered disorder in both angles. In the first regime, for a large number of scatterers, the

average transmission was shown to be momentum-invariant, with the exception of some specific values where the dimensionless momentum kl equates to an integer multiple of $\pi/2$. For these values, the average transmission was shown to be described by a non-exponential decay on the number of scatters. In the second regime, the average transmission was observed to numerically equivalent to the average transmission of the first, with the difference of being flat with respect to momentum. The exponential decay for this regime, however, was observed to be anomalous in the sense that it was characterized by having an extra contribution in the exponent proportional to square root of the number of scatters, in contrast to the standard Anderson localization for which the dependence is purelly proportional to the number of scatters. The existence of this annomalous behavior leads to the definition of a annomalous localization length which, together with the standard localization legth, can be used to describe the localization regime.

Grounded in [63], It was shown how the problem of the hyperfine interaction with nuclear magnetic moments can be effectively modeled by a Hamiltonian of massless Dirac particle subjected to a set of delta-like potential of localized magnetic moments, which allowed us to apply the derived methodology to study the effect of the hyperfine interaction. The analysis showed that, despite being a valid mechanism of suppression, the hyperfine interaction with the nuclear magnetic moments is not strong enough to have any impact in the conductance of the HgTe 2DTI systems, since the estimated localization lengths are orders of magnitude larger than lengths of devices used in experiments.

In addition to the study of effects of HI, the developed methodology was also used to calculate the conductance of a HgTe 2DTI device with $1.9\mu m$ of length and dopped with a dilute concentration of 1.2% of Mn magnetic impurities. The predicted result of $1.26(e^2/h)$, has shown a remarkable agreement with the experimentally observed value of $1.48(e^2/h)$, highlighting the accuracy of the method for 2DTI with a diluted number of magnetic impurities. In addition to the conductance calculation we also made the prediction that increasing the Mn concentration to 2.7% leads to an anomalous localization length of $1.9\mu m$, the same length as the experimental device. This result shows that these devices opens the possibility for experimentally studying the phenomena of anomalous localization in electronic systems, a phenomena still unexplored experimentally.

Chapter 3

Green's Function And Many-body Techniques

3.1 Introduction

When the system to be described is characterized by the absence of interaction between its particles, or when this interaction can be modeled by an effective potential, the description of the entire system can be achieved based on quantities defined for a single-particle system. In other words, the description of this class of systems is confined to the Hilbert space of a single particle, denoted as $\mathcal{H}$. One significant advantage of this approach is that in this space, all physical observables can be described in terms of square matrices, and the dynamic equation reduces to a problem of finding the eigenvalues and eigenvectors of the Hamiltonian, where the eigenvectors are the stationary states and the eigenvalues are their corresponding energies. This approach enables the study of a large number of systems. In fact, a significant portion of modern Physical Chemistry is based on calculations using Density Functional Theory [77, 78], a technique in which a quantum many-body problem is mapped into a single-particle one. For the more general case where particles undergo scatterings due to many-body interactions, the Hilbert space of the system is represented not by $\mathcal{H}$ but by the 'junction' (mathematically expressed through the tensor product) of spaces with different numbers of particles, known as the Fock space [79]: $\mathcal{F}_\nu(\mathcal{H}) = \bigotimes^\infty n = 0 S\nu\mathcal{H}^{\otimes n}$, where S_ν is the symmetrization operator accounting for particle indistinguishability. In this case, physical observables cannot be represented by square matrices, and the dynamic equation does not reduce to a diagonalization problem, thus requiring the use of different approaches for the calculation of physical quantities. In this context, the Green's function formalism will be introduced. Here I am going to

present how the Green's function provides a framework not only to deal with many-body interacting systems but also to be extended to more general cases, such as thermal and out-of-equilibrium quantum systems.

3.2 Real Time GF

Within the Green's Functions formalism, there are special types of correlations with specific time boundary conditions, known as real-time Green's Functions. Depending on the boundary condition, different types of real-time Green's Functions can be defined, namely, the retarded, advanced, lesser, and greater, which are respectively given by:

$$G^r_{\mu\nu}(t,t') = -i\theta(t-t')\langle\{a_\mu(t), a^\dagger_\nu(t')\}\rangle; \tag{3.1}$$

$$G^a_{\mu\nu}(t,t') = i\theta(t'-t)\langle\{a_\mu(t), a^\dagger_\nu(t')\}\rangle; \tag{3.2}$$

$$G^<_{\mu\nu}(t,t') = i\langle a^\dagger_\nu(t')a_\mu(t)\rangle; \tag{3.3}$$

$$G^>_{\mu\nu}(t,t') = -i\langle a_\mu(t)a^\dagger_\nu(t')\rangle. \tag{3.4}$$

$$\tag{3.5}$$

where we are already considering the formalism of second quantization[80, 81] in which the operators $a^\dagger_\mu$ and a_μ create and annihilate electrons in the quantum state μ and $\{,\}$ corresponds to anti-commutator[1].

The interest in real-time Green's Functions comes from the fact that these quantities can provide valuable information about the system, and beyond that, they can be directly related to the values of physical observables. One example is the case of a system subjected to a small time-dependent perturbation $V(t)$. In this case, the Kubo equation allows calculating the expected value of an observable in the linear response regime, which is given by:

$$\langle\hat{A}(t)\rangle = \langle\hat{A}\rangle_0 + \int_{-\infty}^{\infty} dt' G^r_{\hat{A}\hat{V}}(t,t'), \tag{3.6}$$

where $\langle\hat{A}\rangle_0$ is the expected value of the observable $\hat{A}$ in the absence of perturbation. From equation (3.6), we can see that the Kubo formula allows us to calculate the

[1]While the formalism can be defined for both Fermions and Bosons, here I will only focus on Fermions, as the formulation can result in significantly different phenomena

value of physical observables out of equilibrium from quantities calculated at equilibrium. One of these quantities is the response function, which is nothing more than the retarded Green's function $G^r_{\hat{A}\hat{V}}(t,t')$.

One of the greatest advantages of the Green's Functions formalism is that it is possible to define systematic perturbative and non-perturbative methods for calculating properties. The retarded and advanced Green's Functions, for example, may be calculated by employing the equation of motion technique (EOM)[80] in which an infinite hierarchy of dynamic equations coupling the desired Green's Function with other higher-order Green's Functions in the Hamiltonian H is obtained. To understand the method, one should note that by the equation for time evolution in the Heisenberg picture we have:

$$i\frac{\partial G^r_{\mu\nu}(t,t')}{\partial t} = \delta(t-t')\langle\{a_\mu(t), a^\dagger_\nu(t')\}\rangle + G^r_{[a_\mu,\hat{H}]a^\dagger_\nu}(t,t'). \tag{3.7}$$

So, to solve the above equation and find $G^r_{\mu\nu}(t,t')$, it is necessary to know $G^r_{[a_\mu,\hat{H}]a^\dagger_\nu}(t,t')$. We should then consider the equation for $G^r_{[a_\mu,\hat{H}]a^\dagger_\nu}(t,t')$:

$$i\frac{\partial G^r_{[a_\mu,\hat{H}]a^\dagger_\nu}(t,t')}{\partial t} = \delta(t-t')\langle\{[a_\mu(t), H], a^\dagger_\nu(t')\}\eta\rangle + G^r_{[[a_\mu,\hat{H}],\hat{H}]a^\dagger_\nu}(t,t'). \tag{3.8}$$

This process is then repeated in such a way as to couple all Green's functions of the form:

$$G^r_{a_\mu,a^\dagger_\nu}(t,t'); G^r_{[a_\mu,\hat{H}]a^\dagger_\nu}(t,t'); G^r_{[[a_\mu,\hat{H}],\hat{H}]a^\dagger_\nu}(t,t') \ldots \tag{3.9}$$

in increasing order of $\hat{H}$. For a system subjected to a one-body potential (potential bilinear in creation and annihilation operators), the Green's function can be obtained without major problems. However, for most physical systems, solving this system of equations is simply not feasible. This impossibility lies in the fact that if the physical system is subjected to a many-body potential, the higher-order Green's functions in $\hat{H}$ will have an increasing number of creation and annihilation operators, thus making it impossible to decouple the infinite set of equations.

In general, to find the Green's function, some sort of approximation must be made to decouple the system of equations. One that is quite effective in certain regimes is the so-called mean-field approximation[80, 82]. This approximation is valid when some correlations in the system can be neglected, allowing the interaction of one particle with the others to be modeled through the interaction with an effective mean field. This enables the system's Hamiltonian to be written

as a one-body operator, thus facilitating the decoupling of equations.

Despite its usefulness, the Equation of Motion (EOM) technique doesn't allow us to develop a perturbative approach for calculating the Green's function. To do so, we must define the temporal ordered or causal Green's function as follows:

$$G_{\mu\nu}(t,t') = \langle T\{a_\mu(t), a_\nu^\dagger(t')\}\rangle, \tag{3.10}$$

where we define the temporal ordering operator

$$T\{a_\mu(t)a_\nu^\dagger(t')\} = \theta(t-t')a_\mu(t)a_\nu^\dagger(t') + \theta(t'-t)a_\nu^\dagger(t')a_\mu(t). \tag{3.11}$$

The particular Green's function in equation (3.10) is also known as a two-point correlation function since it involves two different times. However, following the same structure, N-points correlation functions can also be defined. Before delving into the perturbative expansion of the causal Green's function, let's recall the most commonly employed representation pictures of quantum mechanics:

- Schrodinger picture: As solutions of the Schrodinger equation, the vector states evolve in time, while the observables are static. The evolution of the states are given by the evolution operator $U(t,t') = e^{-iH_S(t-t')/\hbar}$: $|\Psi_S(t)\rangle = U(t,t')|\Psi_S(t')\rangle$.

- Heisenber picture: The vector states are static and the operators evolve according to the Heisenberg equation. The evolution of an generic observable A can be written in terms of the evolution operator as $A_H(t) = U^\dagger(t,t')A_H(t')U(t,t')$.

- Interaction, or Dirac picture: The systems Hamiltonian is divided in two parts: An solvable "non-interacting" part H_0 and the "interacting" part H_I, being the last part the one preventing the full Hamiltonian from being diagonalizable.[2] In the interaction picture both the states and observables evolves according to the unitary evolution operator associated to the non-interacting Hamiltonian H_0: $|\Psi_I(t)\rangle = U_0(t,t')|\Psi_I(t')\rangle$ and $A_I(t) = U_0^\dagger(t,t')A_I(t')U_0(t,t')$. Where $U_0(t,t') = e^{-iH_0(t-t')/\hbar}$.

In the interaction picture the evolution operator reads

$$U_I(t,t') = U_0^\dagger(t,t_0)U(t,t')U_0(t',t_0). \tag{3.12}$$

[2]This separation of the Hamiltonian is arbitrary and it's employed according to the problem. In the case where H_I is a two-body operator, for example, the interaction picture will lead to a perturbative expansion in H_I.

From which we can deduce it's equation of motion as

$$\begin{aligned} i\hbar\frac{dU_I}{dt} &= i\hbar\frac{dU_0^\dagger}{dt}U(t,t') + i\hbar U_0^\dagger(t,t')\frac{dU}{dt} \\ &= -U_0^\dagger(t,t')H_0U(t,t') + U_0^\dagger(t,t')HU(t,t') \\ &= \hat{H}_I U_I(t,t'). \end{aligned} \tag{3.13}$$

It can be easily checked that, considering the contour condition $U_I(t,t) = \mathbb{I}$, equation (3.13) has the following solution

$$U_I(t,t') = \mathbb{I} - \frac{i}{\hbar}\int_{t'}^{t} \hat{H}_I(\tau)U_I(\tau,t')d\tau. \tag{3.14}$$

This expression can be conveniently rewritten as

$$U_I(t,t') = T\{e^{-\frac{1}{\hbar}\int_{t'}^{t}\hat{H}_I(\tau)d\tau}\}. \tag{3.15}$$

Once we have a general solution to the evolution operator in the Dirac picture we may turn to the problem of calculating Greens functions. Let's now consider a general interacting system at zero temperature, from equation (3.10) the causal Green function will be given by:

$$G_{\mu\nu}(t,t') = \langle T\{a_\mu(t), a_\nu^\dagger(t')\}\rangle = \langle\psi_0|T\{a_\mu(t), a_\nu^\dagger(t')\}|\psi_0\rangle \tag{3.16}$$

Being $|\psi_0\rangle$ the ground state of the complete Hamiltonian. In the form of equation (3.16) the causal Green function has little use since, in general, the interacting ground state is unknown. In order to calculate (3.16) we are going to use the Gell-Mann and Low theorem, which allow us to relate the non-interacting ground state with the interacting one. In order to derive this result, we can consider the situation of adiabatically turning on and off the interaction:

$$H = H_0 + e^{-\varepsilon|t|}H_I. \tag{3.17}$$

By doing so, we guarantee the asymptotic states to be eigenstates of the non-interacting Hamiltonian. Now, lets consider the evolution of the non-interacting ground state $|\phi_0\rangle$ from the asymtotic limits, in the infinite past and infinite future,

to a time t:

$$|\psi\rangle = \lim_{T\to\infty}[U(t,t-T)|\phi_0\rangle], \tag{3.18}$$

$$\langle\psi| = \lim_{T\to\infty}[\langle\phi|U(t+T,t)]. \tag{3.19}$$

The completeness relation from the basis of eigenstates of the full Hamiltonian tells us that

$$\mathbb{I} = |\psi_0\rangle\langle\psi_0| + \sum_{n\neq 0}|\psi_n\rangle\langle\psi_n|, \tag{3.20}$$

where $H|\psi_j\rangle = \epsilon_j$. Now observe that

$$\mathbb{I}|\psi\rangle = \lim_{T\to\infty}\left[|\psi_0\rangle\langle\psi_0|\phi_0\rangle e^{-i\epsilon_0 T} + \sum_{n\neq 0}|\psi_n\rangle\langle\psi_n|\phi_0\rangle e^{-i\epsilon_n T}\right], \tag{3.21}$$

where one assumes a non-degenerate ground state. In order to eliminate the excited states of the right side of (3.21) we will perform a small rotation of T in the imaginary plane:

$$T \to Te^{-i\epsilon} \approx T(1-i\epsilon) \quad 0 < \epsilon << 1, \tag{3.22}$$

from where we define

$$|\psi\rangle_\epsilon = \lim_{T\to\infty(1-i\epsilon)}|\psi_0\rangle\langle\psi_0|\phi_0\rangle e^{-i\epsilon_0 T} + \sum_{n\neq 0}|\psi_n\rangle\langle\psi_n|\phi_0\rangle e^{-i\epsilon_n T}] \tag{3.23}$$

If the above limit exists, since $\epsilon_0 < \epsilon_n \forall n$, the first term from the right side of (3.23) will have a much greater contribution than the rest, such that

$$|\psi\rangle_\epsilon = \lim_{T\to\infty(1-i\epsilon)}|\psi_0\rangle\langle\psi_0|\phi_0\rangle e^{-i\epsilon_0 T} = \lim_{T\to\infty(1-i\epsilon)}|\psi_0\rangle\langle\psi_0|U(t,t-T)|\phi_0\rangle \tag{3.24}$$

which leads us to

$$|\psi_0\rangle = \lim_{T\to\infty(1-i\epsilon)}\frac{U(t_0,t_0-T)|\phi_0\rangle}{\langle\psi_0|U(t_0,t_0-T)|\phi_0\rangle}. \tag{3.25}$$

Analogously, applying the same procedure it is possible to show that

$$\langle\psi_0| = \lim_{T\to\infty(1-i\epsilon)}\frac{\langle\phi_0|U(t_0+T,t_0)}{\langle\phi_0|U(t_0+T,t_0)|\psi_0\rangle} \tag{3.26}$$

With equations (3.26) and (3.25) we are now ready to define an expression for the

causal GF in the particular case of zero temperature, where the density matrix becomes the projector operator into the ground state. Considering a reference time t_0 where the initial conditions are defined, the equation (3.16) becomes:

$$G_{\mu\nu}(t,t') = \langle\psi_0|T\{U^\dagger(t,t_0)a_\mu(t_0)U(t,t_0), U^\dagger(t',t_0)a_\nu^\dagger(t_0')U(t',t_0)\}|\psi_0\rangle \tag{3.27}$$

Using equations (3.25) and (3.26), for the case where $t > t'$ we have

$$G_{\mu\nu}(t,t') = \lim_{T\to\infty(1-i\epsilon)} \frac{\langle\phi_0|U(t_0+T,t_0)U^\dagger(t,t_0)a_\mu(t_0)U(t,t_0)U^\dagger(t',t_0)a_\nu^\dagger(t_0)U(t',t_0)U(t_0,t_0-T)|\phi_0\rangle}{\langle\phi_0|U(t_0+T,t_0)|\psi_0\rangle\langle\psi_0|U(t_0,t_0-T)|\phi_0\rangle}. \tag{3.28}$$

The denominator of the above equation may be calculated by imposing normalization on the state $|\psi_0\rangle$:

$$\langle\psi_0|\psi_0\rangle = \lim_{T\to\infty(1-i\epsilon)} \frac{\langle\phi_0|U(t+T,t)U(t,t-T)|\phi_0\rangle}{\langle\phi_0|U(t_0+T,t_0)|\psi_0\rangle\langle\psi_0|U(t_0,t_0-T)|\phi_0\rangle} = 1. \tag{3.29}$$

That leads us to

$$\langle\phi_0|U(t_0+T,t_0)|\psi_0\rangle\langle\psi_0|U(t_0,t_0-T)|\phi_0\rangle = \lim_{T\to\infty(1-i\epsilon)} \langle\phi_0|U_I(T,-T)|\phi_0\rangle e^{-2i\varepsilon_0 T} \tag{3.30}$$

Where ε_0 is the energy eigenvalue of $|\phi_0\rangle$. So

$$G_{\mu\nu}(t,t') = \lim_{T\to\infty(1-i\epsilon)} \frac{\langle\phi_0|U(t_0+T,t)a_\mu(t_0)U(t,t')a_\nu^\dagger(t_0)U(t',t_0-T)|\phi_0\rangle}{\langle\phi_0|U_I(T,-T)|\phi_0\rangle e^{-2i\varepsilon_0 T}} \tag{3.31}$$

Now observe that, from the definition of equation (3.12)

$$\begin{aligned}
&\langle\phi_0|U(t_0+T,t)a_\mu(t_0)U(t,t')a_\nu^\dagger(t_0')U(t',t_0-T)|\phi_0\rangle = \\
&\langle\phi_0|U_0(t_0+T,t_0)U_I(t_0+T,t)U_0^\dagger(t,t_0)a_\mu(t_0)U_0(t,t_0)U_I(t,t')U_0^\dagger(t',t_0)a_\nu^\dagger(t_0)U_0(t',t_0) \\
&U_I(t',t_0-T)U_0(t_0-T,t_0)|\phi_0\rangle = \\
&= \langle\phi_0|T\{U_I(t_0+T,t)a_\mu(t)U_I(t,t')a_\nu^\dagger(t')U_I(t',t_0-T)\}|\phi_0\rangle e^{-2i\varepsilon_0 T} \\
&= \langle\phi_0|T\{a_\mu(t)a_\nu^\dagger(t')U_I(t_0+T,t_0-T)\}|\phi_0\rangle e^{-2i\varepsilon_0 T} \\
&= \langle\phi_0|T\{a_\mu(t)a_\nu^\dagger(t')U_I(T,-T)\}|\phi_0\rangle e^{-2i\varepsilon_0 T}
\end{aligned} \tag{3.32}$$

where the last passage is always valid for a closed system, for which the evolution operator has the general solution of equation (3.15). Substituting equation (3.32)

in equation (3.31) we get

$$G_{\mu\nu}(t,t') = \lim_{T\to\infty(1-i\epsilon)} \frac{\langle\phi_0|T\{a_\mu(t)a_\nu^\dagger(t')S\}|\phi_0\rangle}{\langle\phi_0|S|\phi_0\rangle} \tag{3.33}$$

where the scattering operator S is introduced as

$$S \equiv \lim_{T\to\infty(1-i\epsilon)} U_I(T,-T). \tag{3.34}$$

Equation (3.33) is of utmost importance in the Green's function formalism because it allows us to calculate the interacting Green's function in terms of the non-interacting ones. In fact, by expanding the exponential in equation (3.15) in powers of H_I, different non-interacting N-points correlation functions will appear in the expression, which, by means of Wick's Theorem[80, 83], can then be written in terms of the non-interacting two-points correlation function. This process usually leads to complicated equations for the interacting Green's function; however, the calculations can be made simpler by employing the Feynman diagrams technique. This method provides a graphical representation for the perturbative expansion of the Green's function, where mathematical terms are replaced by diagrams. This perturbative methodology for calculating the Green's function will be applied in a practical example in Chapter 5.

In addition to (3.33), another very important relation can be deduced. The so-called Dyson equation is a mathematical expression relating the interacting Green's function to the non-interacting one and to a quantity known as the self-energy, usually represented by Σ. In matrix notation, the Dyson equation can be written as

$$G(t,t') = G_0(t,t') + \int\int dt_1 dt_2 G_0(t,t_1)\Sigma(t_1,t_2)G(t_2,t') \tag{3.35}$$

where G_0 is the Green's function calculated using the non-interacting Hamiltonian H_0, known as the non-interacting Green's function. Since the Green's function depends only on the difference in time for closed systems, in the frequency domain, the Dyson equation can be written as

$$G(\omega) = G_0(\omega) + G_0(\omega)\Sigma(\omega)G(\omega) \;\rightarrow\; G(\omega) = \frac{1}{\omega - H_0 - \Sigma(\omega)} \tag{3.36}$$

As we can see from the above equation, the self-energy can be seen as a way to

account for the effect of many-body scattering in the form of a dynamic potential. It can be defined in terms of Feynman diagrams as the sum of all possible irreducible diagrams [80, 84].

In addition to the previous relations, the Green's functions of systems in thermodynamic equilibrium must also obey another very important relation reflecting the fluctuation-dissipation theorem [85]. Indeed, using the Källén-Lehmann spectral representation [80], it is possible to show that

$$G^{<}(\omega) = -(G^{r}(\omega) - G^{a}(\omega))f(\omega) = G^{r}(\omega)(\Sigma^{r}(\omega) - \Sigma^{a}(\omega))G^{a}(\omega)f(\omega) \quad (3.37)$$

Being $f(\omega)$ the Fermi-Dirac distribution function. Considering the diagonal components of $G^{<}$, this expression allows us to calculate the projected density of states(PDOS) ρ_i onto a state i, in terms of the imaginary part of the retarded Green's function:

$$\rho_i(\omega) = -\frac{1}{\pi} Im\{G^{r}_{ii}\} \quad (3.38)$$

3.3 Non-Equilibrium Greens Functions Formalism

One of the great strengths of the Green's function formalism is that the techniques can be generalized to describe even more complex systems, in particular, systems with many-body interactions at finite temperature. In this case the density matrix is no longer a projection into the ground state, however we can take advantage of its form

$$\rho = \frac{e^{\beta H}}{Z}, \quad (3.39)$$

being $Z = Tr\{e^{\beta H}\}$ the partition function, to define a imaginary time perturbation theory. Here, it is possible to define an imaginary time Green's function also known as Matsubara Greens function and, similarly to the zero temperature case, it's possible to perform a pertubative expansion to which an analogous version of the Wick theorem allows the expansion to be written in terms of finite temperature Green's functions calculated using non-interacting density matrix $\rho_0 = e^{\beta H_0}/Z$. Once calculated, the Matsubara GF can be used to calculate the real-time GF, which has a direct relationship with physical observables.

So far it has been shown that the GF technique can be used to study quantum systems at zero and finite temperatures, however given the generality of the method we might wonder if it can be applicable to the most general case of systems with time dependent interactions. The description of these systems poses a major challenge since they're out of thermodynamic equilibrium. Indeed, in this case the density matrix is not a projector into the ground state nor has an exponential form, therefore restricting the use of the previous methods to define a perubation theory.

An extension of GF formalism to the more general case of time-dependent Hamiltonian was proposed independently by Keldysh and Schwinger[18, 86]. In order to understand their solution it's instructive to see where the limitations of the Gell-Man Low theorem starts to appear. One of the key steps in the derivation of (3.15) lies in the turning on and off of the inteactions, which guarantees asymptotic free states not only in the infinite past but also in the infinite future. After turning on a time dependent interaction there's no guarantee of the state in the infinite future being an eigenstate of the non-interacting Hamiltonian, which prevents us to evolve backwards in time from the non-interacting ground state in the infinite future like what was done in equation (3.26). In order to circumvent this problem, observe that equation (3.28) can be written in terms of the states in the interacting picture as

$$G_{\mu\nu}(t,t') = \langle\phi(\infty)|_I T\{a_{mu}(t)a^\dagger_{nu}(t')U_I(\infty,-\infty)\}|\phi_0(-\infty)\rangle_I \tag{3.40}$$

where the state in the infinite future $|\phi(\infty)\rangle_I$ relates to the state in the infinite past $|\phi(-\infty)\rangle_I$ by a phase shift $|\phi(\infty)\rangle_I = \langle\phi_0|U_I(\infty,-\infty)|\phi_0\rangle_I|\phi(-\infty)\rangle_I$. In the case where the Hamiltonian is time dependent, these states are no longer related solely by a phase shift, therefore preventing the derivation of equation (3.33).

Keldysh overcome the problem in the time dependent case by avoiding any reference to the state in the infinite future, which he did by defining the state in the infinite future in terms of the state in the infinite past:

$$|\phi(\infty)\rangle_I = U_I(\infty,-\infty)|\phi(-\infty)\rangle_I \tag{3.41}$$

which lead equation (3.40) to

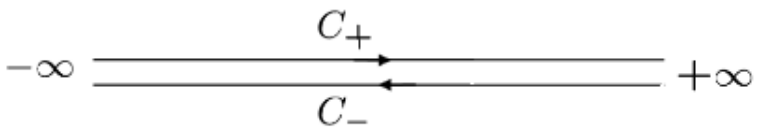
$$G_{\mu\nu}(t,t') = \langle\phi(-\infty)|_I U_I(-\infty,\infty)T\{a_{mu}(t)a^\dagger_{nu}(t')U_I(\infty,-\infty)\}|\phi_0(-\infty)\rangle_I \tag{3.42}$$

In this case the term $U_I(-\infty,\infty)$ can not simply be moved inside the temporal ordering operator, and the adopted strategy is to define a contour ordered Green function with two different branches, as depicted in figure 3.1. In this way the Keldysh Green function is defined as

$$G^K_{\mu\nu}(t,t') = \langle\phi(-\infty)|_I T_c\{U^c_I(-\infty,-\infty)a_\mu(\tau)a^\dagger_\nu(\tau')\}|\phi_0(-\infty)\rangle_I \tag{3.43}$$

where we defined the contour ordered operator, T_c, which orders the operators according to their appearance in the contour and

$$U^c_I \equiv T_c\, exp\left(-i\oint_C \mathrm{d}\tau_1 H'(\tau_1)\right). \tag{3.44}$$



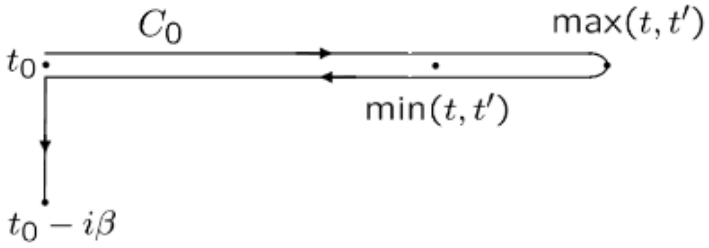
$$C = C_+ \cup C_-$$

Figure 3.1: Schwinger-Keldysh countour. Figure obtained from [87]

.

The Keldysh-Schwinger contour is specifically suitable for describing systems with no memory effect, in other words, systems for which the initial correlations play no major role on its dynamics. A large number of systems fall into this category, in particular those where a non-equilibrium steady state is reached after some time, which is the case in the majority of transport problems. Besides the Keldysh-Schwinger different contours can be defined, one example is the Kadanoff-Baym[19] contour presented in figure 3.2, which can be viewed as a generalization of Keldysh-Schwinger in the sense that it can be used to describe non-equilibrium systems in the transient regime and also because it can be used to derive the Keldysh-Schwinger one.

One of the great advantages of equation (3.43) is that all the tecniques and methods derived for the real time GF can be extended to the Keldysh Green's functions, including the perturbative expansion, the machinary of Feynman diagrams



$$C^* = C_0 \cup [t_0, t_0 - i\beta]$$

Figure 3.2: Kandanoff-Baym countour. In this case, the contour is defined in terms of the time when the time-dependent interaction is activated, t_0, the maximum and minimum time of the Green's function, $max(t,t')$ and $min(t,t')$, and the temperature $T = 1/\beta$. Figure obtained from [87]

.

and the Dyson equation. It is important to point out however that, differently from the real time GF, the ones defined in the contour can not be directly related to physical observables, and some technique must be defined to calculate the real time GF from the contour ordered one. This problem can be solved by performing an analytic continuation of the contour to the real axis and, depending on what branch the times τ and τ' are located, different GF are obtained:

$$G_{\mu\nu}(\tau,\tau') = \begin{cases} G^T_{\mu\nu}(\tau,\tau') = -i\langle T\{a_\mu(\tau)a^\dagger_\nu(\tau')\}\rangle \text{ if } \tau,\tau' \in C_+ \\ G^<_{\mu\nu}(\tau,\tau') = i\langle a^\dagger_\nu(\tau')a_\mu(\tau)\rangle \text{ if } \tau \in C_+, \tau' \in C_- \\ G^>_{\mu\nu}(\tau,\tau') = -i\langle a_\mu(\tau)a^\dagger_\nu(\tau')\rangle \text{ if } \tau \in C_-, \tau' \in C_+ \\ G^{\tilde{T}}_{\mu\nu}(\tau,\tau') = -i\langle \tilde{T}\{a_\mu(\tau)a^\dagger_\nu(\tau')\}\rangle \text{ if } \tau,\tau' \in C_- \end{cases} \tag{3.45}$$

where G^T is the time-ordered Green function (3.16), and $\tilde{T}$ is an anti-time ordering operator which orders operators in the opposite way compared to T, so that $G^{\tilde{T}}$ is the anti-time-ordered GF. From the definitions it's possible to see that

$$G^r = G^T - G^< = G^> - G^{\tilde{T}}, \tag{3.46}$$

$$G^a = G^T - G^> = G^< - G^{\tilde{T}}, \tag{3.47}$$

$$G^r - G^a = G^> - G^<. \tag{3.48}$$

The above relations shows us that there are only three independent real-time Green's functions, and along the next chapters we are going to choose to work mostly with the retarded, advanced and lesser GFs.

An additional challenge might appear when performing the analytic continuation of the contour ordered GF, this happens because the perturbative expansion is usually written in terms of convolution integrals of the type

$$C(\tau_1, \tau_1') = \int d\tau_2 A(\tau_1, \tau_2) B(\tau_2, \tau_1'). \tag{3.49}$$

In such cases the analytic continuation can be performed using the Langreth theorem [88] which consists in a set rules defined for convolutions. Using a matrix notation for the integrals, $C = AB$ in the equation above, some of the Langreth rules can be defined:

$$(AB)^{<(>)} = A^r B^{<(>)} + A^{<(>)} B^a, \tag{3.50}$$

$$(AB)^{r(a)} = A^{r(a)} B^{r(a)}, \tag{3.51}$$

$$(ABC)^{<(>)} = A^r B^r C^{<(>)} + A^r B^{<(>)} C^a + A^{<(>)} B^a C^a, \tag{3.52}$$

$$(ABC)^{r(a)} = A^{r(a)} B^{r(a)} C^{r(a)}. \tag{3.53}$$

An important relation for the lesser component can be derived from applying equation (3.52) to the Dyson equation:

$$G^< = G^r \Sigma^< G^a. \tag{3.54}$$

This is known as the Keldysh equation (3.54) defines the dependence of $G^<$ on $\Sigma^<$ in the non-equilibrium regime. It is possible to observe that in thermodynamic equilibrium this equation recovers the fluctuation dissipation theorem.

3.4 General current equation

The Keldysh Green's function formalism provides a powerful tool for studying nonequilibrium quantum transport in nanoscale systems, such as quantum dots[89, 90], and molecular junctions. It is widely used in the field of mesoscopic Physics and quantum transport, providing insights into the dynamics of charge carriers in nonequilibrium situations. As we already pointed out, the first successful microscopic theoretical description of electronic transport dates back to the late 1950s, when Landauer related the systems conductance to the quantum trans-

mission of so called conduction channels. At first, the Landauer transmission was based on a phenomenological approach, but it was latter put on solid grounds by means of a transport theory developed by Meir and Wingreen [91] using Keldysh Green's functions. The Meir-Wingreen transport theory is grounded in a general current equation derived for systems composed by three different regions: two metalic leads in thermodynamic equilibrium, each one acting as a heat and particle reservoir characterized by a fixed temperature and chemical potential. Bridging the leads, there is a mesoscopic region characterized by a nonequilibrium distribution where the scattering takes place.

In order to derive the general equation, following the work of Meir and Wingreen, our starting point is the Hamiltonian

$$H = \sum_{k,\alpha\in L,R} \varepsilon_{k\alpha} c^{\dagger}_{k\alpha} c_{k\alpha} + H_{int}(\{d^{\dagger}_{n}; d_{n}\}) + \sum_{k,\alpha\in L,R} (V_{k\alpha,n} c^{\dagger}_{k\alpha} d_{n} + H.c) \tag{3.55}$$

with $c^{\dagger}_{k\alpha}(c_{k\alpha})$ the creation (annihilation) operator for an electron with momentum k in a channel α either in the right or left lead, and $d^{\dagger}_{n}(d_{n})$ is the creation (annihilation) operator for an electron in a state of the scattering region described by the quantum number n(in general n can comprise a set of quantum numbers). It is important to observe that since we are considering metallic leads, many-body interactions within the leads and between the leads and the scattering region are strongly screened and can be neglected, allowing the description in terms of propagating waves while the electrons in the scattering region are described by an interacting Hamiltonian with a general many-body interaction. The last term of (3.55) is responsible for the coupling between the leads and scattering region states.

The electronic current can be calculated by

$$J_L = -e\langle \dot{N}_L \rangle = \frac{-ie}{\hbar}\langle [H, N_L] \rangle \tag{3.56}$$

$$= \frac{-e}{\hbar} \sum_{k,\alpha\in L;\ n} (V_{k\alpha,n}\langle c^{\dagger}_{k\alpha} d_{n}\rangle - V^{*}_{k\alpha,n}\langle d^{\dagger}_{n} c_{k\alpha}\rangle) \tag{3.57}$$

$$= \frac{e}{\hbar} \sum_{k,\alpha\in L;\ n} \int_{-\infty}^{\infty} \frac{d\omega}{2\pi} [V_{k\alpha,n} G^{<}_{n,k\alpha} - V^{*}_{k\alpha,n} G^{<}_{k\alpha,n}] \tag{3.58}$$

which in terms of Green functions becomes

$$J_L = \frac{e}{\hbar} \sum_{k,\alpha\in L;\ n} \int_{-\infty}^{\infty} \frac{d\omega}{2\pi} [V_{k\alpha,n} G^{<}_{n,k\alpha}(\omega) - V^{*}_{k\alpha,n} G^{<}_{k\alpha,n}(\omega)]. \tag{3.59}$$

The Green functions $G_{n,k\alpha}$ and $G_{k\alpha,n}$ can be found by the Dyson equation for the system:

$$\left[I\omega - \begin{pmatrix} H_{LL} & H_{LD} & 0 \\ H_{LD}^{\dagger} & H_{DD} + \Sigma_{int} & H_{RD}^{\dagger} \\ 0 & H_{RD} & H_{RR} \end{pmatrix}\right] \begin{pmatrix} G_{LL} & G_{LD} & G_{LR} \\ G_{DL} & G_{DD} & G_{DR} \\ G_{RL} & G_{RD} & G_{RR} \end{pmatrix} = \begin{pmatrix} I_{LL} & 0 & 0 \\ 0 & I_{DD} & 0 \\ 0 & 0 & I_{RR} \end{pmatrix} \tag{3.60}$$

with the indices L,R and D referring to the states in the left lead, right lead and scattering region respectively, and the letters H, G, Σ and I corresponding to the Hamiltonian, Green function, Self-Energy and Identity operator respectively. Observe that the Self-Energy is only nonzero in the scattering region, where the many-body scattering happens. Solving for G_{LD} and G_{DL} we get, in matrix notation

$$G_{LD}(\omega) = \mathcal{G}_{LL}(\omega) H_{LD} G_{DD}(\omega), \tag{3.61}$$

$$G_{DL}(\omega) = G_{DD}(\omega) H_{DL} \mathcal{G}_{LL}(\omega). \tag{3.62}$$

Where we defined the so called surface GF

$$\mathcal{G}_{LL} = \frac{1}{\omega - H_{LL}} \tag{3.63}$$

which is nothing more than the GF of the interface between the lead and the scattering region. Now, applying the Langreth rules defined in equations (3.50) to (3.61) and (3.62) one obtains

$$G_{LD}^{<}(\omega) = \mathcal{G}_{LL}^{r}(\omega) H_{LD} G_{DD}^{<}(\omega) + \mathcal{G}_{LL}^{<}(\omega) H_{LD} G_{DD}^{a}(\omega), \tag{3.64}$$

$$G_{DL}^{<}(\omega) = G_{DD}^{r}(\omega) H_{DL} \mathcal{G}_{LL}^{<}(\omega) + G_{DD}^{<}(\omega) H_{DL} \mathcal{G}_{LL}^{a}(\omega). \tag{3.65}$$

$$\tag{3.66}$$

Substituting in (3.59) we get

$$J_L = \frac{e}{\hbar} \int_{-\infty}^{\infty} \frac{d\omega}{2\pi} Tr\{H_{LD}[G_{DD}^{r}(\omega) H_{DL} \mathcal{G}_{LL}^{<}(\omega) + G_{DD}^{<}(\omega) H_{DL} \mathcal{G}_{LL}^{a}(\omega)] - H_{DL}[\mathcal{G}_{LL}^{r}(\omega) H_{LD} G_{DD}^{<}(\omega) + \mathcal{G}_{LL}^{<}(\omega) H_{LD} G_{DD}^{a}(\omega)]\}. \tag{3.67}$$

Since the leads are in thermodynamic equilibrium, from the fluctuation-dissipation

theorem we have that $\mathcal{G}^<_{LL}(\omega) = -f_L(\omega)(\mathcal{G}^r(\omega) - \mathcal{G}^a(\omega))$, which lead us to

$$J_L = \frac{ie}{\hbar}\int_{-\infty}^{\infty}\frac{d\omega}{2\pi}Tr\{\Gamma_L(\omega)[G^<_{DD}(\omega) + (G^r(\omega)_{DD} - G^a(\omega)_{DD})f_L(\omega)]\} \tag{3.68}$$

where $\Gamma_L = iH_{DL}(\mathcal{G}^r_{LL} - \mathcal{G}^a_{LL})H_{LD}$ is a quantity related to the lifetime of the electrons in the scattering region due to the coupling with the leads.

In the framework of (3.68), the Landauer approach can be obtained by considering the non-interacting regime. In order to derive the so called Landauer-Butiker transmission, observe that solving (3.60) for G_{DD} we obtain

$$G_{DD}(\omega) = \frac{1}{\omega - H_{DD} - \Delta_L(\omega) - \Delta_R(\omega) - \Sigma_{int}(\omega)} \tag{3.69}$$

where Δ_L and Δ_R are the hybridization function with the left and right leads, which are given respectively by

$$\Delta_L(\omega) = H_{DL}\mathcal{G}_{LL}(\omega)H_{DL}, \tag{3.70}$$

$$\Delta_R(\omega) = H_{DR}\mathcal{G}_{RR}(\omega)H_{DR}. \tag{3.71}$$

The hybridization function appears as a component of the self-energy that accounts for the effect of hybridization between the states of the scattering region and leads, it must be differentiated from Σ_{int} which accounts for the effect of many-body scatterings due to many-body interactions. The lesser component of the total self-energy Σ_{DD}, which ultimately measures scattering rate of the levels in the central region, can be written as

$$\Sigma^<_{DD}(\omega) = \Delta^<_L + \Delta_R < +\Sigma^<_{int} = i\Gamma_L f_L + i\Gamma_R f_R + \Sigma^<_{int}. \tag{3.72}$$

Now observe that in the non-interacting regime, $\Sigma_{int} = 0$, the Keldysh equation leads to

$$\begin{aligned} G^<(\omega) &= iG^r(\Gamma_L f_L + \Gamma_R f_L)G^a \\ &= iG^r\Gamma_R G^a(f_R - f_L) + iG^r(\Gamma_L + \Gamma_R)G^a f_L \\ &= iG^r\Gamma_R G^a(f_R - f_L) - (G^r - G^a)f_L \end{aligned} \tag{3.73}$$

where by substituting equation (3.73) into equation (3.68) we obtain

$$J_L = \frac{e}{h}\int_{-\infty}^{\infty} d\omega T_{BL}(\omega)\big(f_L(\omega) - f_R(\omega)\big) \tag{3.74}$$

where is defined the Landauer-Buttiker transmission

$$T_{BL}(\omega) = Tr\{\Gamma_L G^r_{DD}\Gamma_R G^a_{DD}\} \tag{3.75}$$

can be defined. This gives in terms of GFs the transmission probability of an electron with energy ω.

Both equations (3.68) and (3.75) are very powerful statements since they establish an electronic transport theory in terms of the formalism of Keldysh GFs. In the next section we are going to explore how the Keldysh formalism can be used beyond electronic transport in the study of thermometric phenomena. For the sake of simplicity, we are going to drop the indices DD used to refer to the scattering states.

3.5 Thermoeletric transport properties

In the previous section we studied the electronic charge transport between two leads of different chemichal potential. We might then wonder about the transport of heat in the case of a gradient of temperature present between the leads. In this situation a heat current between the leads will be estabilished, and it will be carried not only by electrons but also by phonons, being the latter the quanta of the systems vibrations. The total heat current will be given by

$$I_Q = I_{Q,ph} + I_{Q,el}, \tag{3.76}$$

where $I_{Q,el}$ and $I_{Q,ph}$ are the heat current due to electrons and phonons respectively. Both currents can be calculated using the transport theory derivated from the Keldysh formalism however, since we are mostly interested in describing the thermometric transport properties, we will focus in the heat current due to electrons. The equation for the eletronic heat transfer can be obtained straight from equation (3.68). In fact we just need to replace the electrons charge by the

energy it carries relative to the chemical potential μ:

$$J_L = \frac{i}{\hbar}\int_{-\infty}^{\infty}\frac{d\omega}{2\pi}(E-\mu)Tr\{\Gamma_L(\omega)[G^<(\omega)+(G^r(\omega)-G^a(\omega))f_L(\omega)]\}. \quad (3.77)$$

In the regime characterized by the absence of many-body interactions the Landauer-Büttiker transmission allows us to calculate not only the charge but the heat current as well. The calculation of the heat current due to phonons is not that straightforward in the sense that it depends on other parameters related to the systems structure.

One of the effects of a gradient of temperature between the leads is the appearance of a flow of charge carriers which may induce an electric field within the system. Named after Thomas Johann Seebeck for its discovery in 1821, the so called Seebeck[92] effect describes the appearance of a gradient in the electrostatic potential due to the rearrangement of charges occasioned by a gradient of temperature. This effect can be quantitatively described by the Seebeck coeficient S, which measures the difference in temperature ΔT between two regions required to induce a difference in potential ΔV:

$$S = \frac{\Delta V}{\Delta T}\Big|_{I=0} \quad (3.78)$$

In addition to the Seebeck effect there are also the Peltier[93] and the Thomson[94] effects. The first is effectively the inverse of Seebeck effect in the sense that it happens when a gradient of temperature is induced by a potential difference, while the second describes the heating and cooling of a material given a gradient of temperature. Only the Seebeck effect will be addressed in this work.

Within the linear response regime, small voltage and small temperature differences between the leads, the term $f_L - f_R$ in the electrical current can be Taylor expanded to obtain

$$\Delta I = \left[\frac{2e^2}{h}\int_{-\infty}^{\infty}\mathcal{T}(E)\left(-\frac{\partial f}{\partial E}\right)dE\right]\Delta V + \left[\frac{2e}{h}\int_{-\infty}^{\infty}\mathcal{T}(E)\left(-\frac{\partial f}{\partial E}\right)(E-\mu)dE\right]\frac{\Delta T}{T}. \quad (3.79)$$

In this regime the conductance G and the Seebeck coefficient S are given by [95, 96],

$$G = \lim_{\Delta V\to 0}\left(\frac{\Delta I}{\Delta V}\right)_{\Delta T=0} = e^2K_0, \quad (3.80)$$

$$S = \lim_{\Delta T\to 0}\left(\frac{\Delta V}{\Delta T}\right)_{\Delta I=0} = -\frac{1}{eT}\frac{K_1}{K_0} \quad (3.81)$$

where the intermediate function K_n is defined as

$$K_n(\mu, T) = \frac{2}{h} \int_{-\infty}^{\infty} \mathcal{T}(E) \left(-\frac{\partial f(E, \mu)}{\partial E} \right) (E - \mu)^n dE. \tag{3.82}$$

Moreover, the electron thermal conductance is defined as

$$\kappa_e = \frac{1}{T} \left(K_2 - \frac{K_1^2}{K_0} \right). \tag{3.83}$$

These effects find useful applications in the generation of thermoelectric devices, the Seebeck effect in particular can be used to produce thermal generators capable of converting thermal into electrical energy. These devices are ultimately thermal machines and, as such, they are all characterized by an intrinsic efficiency. The maximum theoretical efficiency of an thermoelectric device can be quantitatively described by the dimensionless figure of merit ZT which, in the case of a thermal generator, allows to calculate the maximum efficiency by the expression

$$\eta_{max} = \frac{T_H - T_C}{T_H} \left(1 - \frac{1 + T_C/T_H}{\sqrt{1 + ZT} + T_C/T_H} \right) \tag{3.84}$$

Being T_H and T_C the temperature of the hot and cold region respectively and T the average absolute operating temperature. The quantity Z can be calculated by

$$Z = \frac{GS^2}{\kappa_{ph} + \kappa_{el}} \tag{3.85}$$

Chapter 4

Gate-voltage enhancement of thermoelectric transport in graphene nanoribbons quantum dots

4.1 Introduction

Significant advances regarding the synthesis and fabrication of novel materials– reached over the last decade– have allowed for the advent of nanostructures with improved physical and chemical properties that may potentially enhance performance in optoelectronics, photovoltaics, catalysis and thermoelectrics devices.[97, 98, 99, 100] Thermoelectric materials are of particular importance for power generation applications as they are able to convert heat into electricity. Their performance is measured by the figure of merit ZT(presented in the previous chapter) which, due to the convoluted relation of the parameters controlling the figure of merit, only a reduced number of bulk and two-dimensional materials have been shown to provide optimal ZT values[101, 102, 103]. Thus, the search for alternative materials with improved figure of merit have sparked the theoretical and experimental characterization of 1D and 0D systems for thermoelectric applications.[104, 105, 98, 106] In particular, semiconducting 1D nanostructures have proven to be of particular interest as they offer more opportunities to reduce the phonon thermal conductance and, at the same time, allow the tunability of their electronic properties thanks to quantum confinement effects.[107, 108, 109, 110] Therefore, phosphorus, transition metal dichalcogenides and carbon based nanoribbons, to mention a few, have been widely examined and proposed as alternative thermoelectric materials.[111, 112, 113, 114, 115, 116] In the same line, several strategies that include edge engineering (disorder, defect, passivation) and gate-voltage application have been proposed as alternatives to reduce the thermal conductivity while preserving the electrical conductivity and thermoelectric power in these

nanostructures[112, 111, 117, 118, 119, 120].

Within that class of materials, graphene nanoribbons are ideal candidates due to their interesting properties.[121, 122, 123, 124] Recently, atomically precise edge GNRs have been successfully fabricated from bottom-up approaches based on metal surface-assisted assembly of appropriate molecular precursors.[125, 126] This novel method enables the synthesis of ribbons with a variety of edge shapes and widths whose electronic and optical properties make them appealing candidates for a range of applications.[127, 128, 129] More interestingly, this approach has also been used to realize tunable graphene quantum dots (GQD) which are formed due to the lateral junction of small armchair graphene nanoribbon segments with different widths[33, 130]. Thus, the electronic and transport properties of the resulting GQDs, have been predicted to be highly tunable allowing a smooth transition from an antiresonant to a resonant transport regime that scales with the structure length.[131] This set of predicted features suggests the potential use of these GQDs for thermolectric applications as it combines the electronic of graphene with the presence of molecular levels[132, 133]. Although, the electronic and transport properties of GQDs have been previously investigated, a comprehensive study of their thermoelectric properties is still lacking.

In this chapter, we combine density functional theory (DFT) with the, previously described, non-equilibrium Green's functions (NEGF) methods[134] to investigate the electronic and thermoelectric properties of a recently sinthesized GQD known as 7-14-7 AGQD.[33] Our results indicate that the electronic states at the band edge are highly localized in the inner region of the GQD, instead of the borders, and can be shifted to higher energies by applying a gate voltage. Moreover, at zero voltage-gate and room temperature, we find the lower bound of ZT to be 0.25. By increasing the applied gate voltage, the lower bound is further tuned to exceed unity. A schematic represenation of the system under study is shown in figure 4.1

4.2 Methodology

The device we simulate is constituted by three spatial regions, namely two semi-infinite pristine graphene sheets acting as leads (L/R), and a central scattering

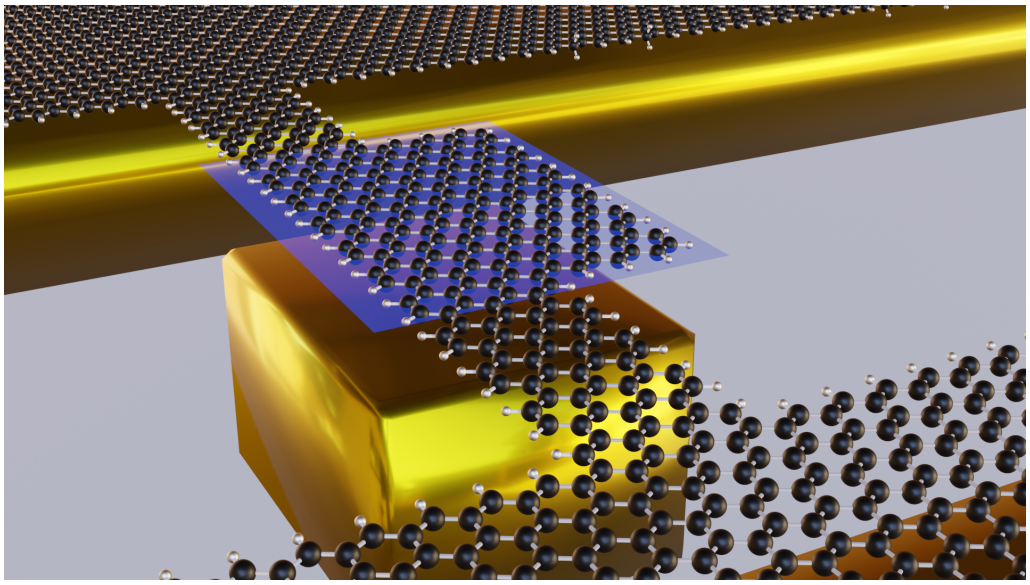


Figure 4.1: Schematic representation of the system under study: A 7-14-7 AGQD bridging two semi-infinite graphene leads and a gate electrode (centered golden bar) capable of creating an electrostatic field in a rectangular region of cross-section depicted in blue.

region (S), as shown in Figure 4.2b. The scattering region of the device consists in a heterostructure which is assembled from a small 14-AGNR segment that is laterally sandwiched by two 7-AGNRs segments as depicted in Figure 4.2a. This results in a nanostructure with variable width going from 7 to 14 and back to 7 carbon atoms along the ribbon axis, that is labeled as 7-14-7 AGQD. The

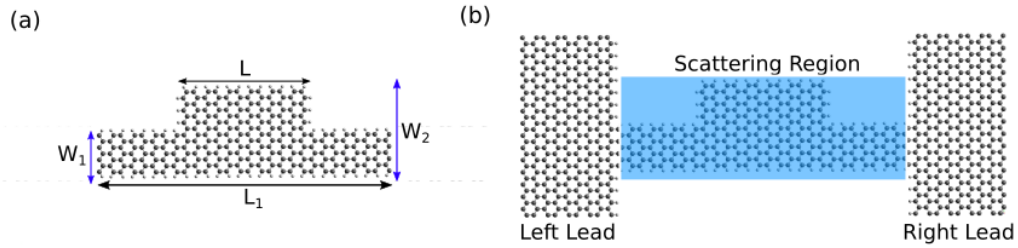


Figure 4.2: (a) Schematic representation of a 7-14-7 AGQD. The inner (outer) part of the quantum dot possess a width $W_2 \approx 16$ ($W_1 \approx 7.4$ Å) that correspond to a 14-AGNR (7-AGNR) segment. (b) Schematic representation of the system used for modeling the transport problem under gate voltage V_g. The central scattering region is described by the Hamiltonian H_S

system's electronic properties were computed using density functional theory (DFT),[135, 136] as implemented in the SIESTA[1] code[139]. An energy mesh cutoff

[1]For a brief discussion of Density Functional Theory and the SIESTA implementation we suggest

of 250 Ry with only Γ-point k-sampling for the transport calculation, while a $1 \times 1 \times 30$ k-grid was used in the calculation of the leads. The supercell size of the scattering region is set to $100 \times 37 \times 98.29$. The generalized gradient approximation (GGA) for the exchange correlation functional, using a double-ζ basis set with polarization orbitals was employed. The atomic coordinates of all structures were optimized using a conjugate gradient (CG) algorithm considering a residual force threshold of 0.01 eV/Å. A vacuum region of 100 Å was used in the directions perpendicular to the 7-14-7 AGQD to avoid interaction between periodic images. We applied an external gate voltage by fixing the potential in a specific region of space. The external gate is modeled by setting the potential V_g in a region 25.9× 29 Å wide and 10 Å above the the AGQD, as depicted in 4.3. The potential drops exponentially with a half-length of 4 Å and with a 20 Å cutoff.

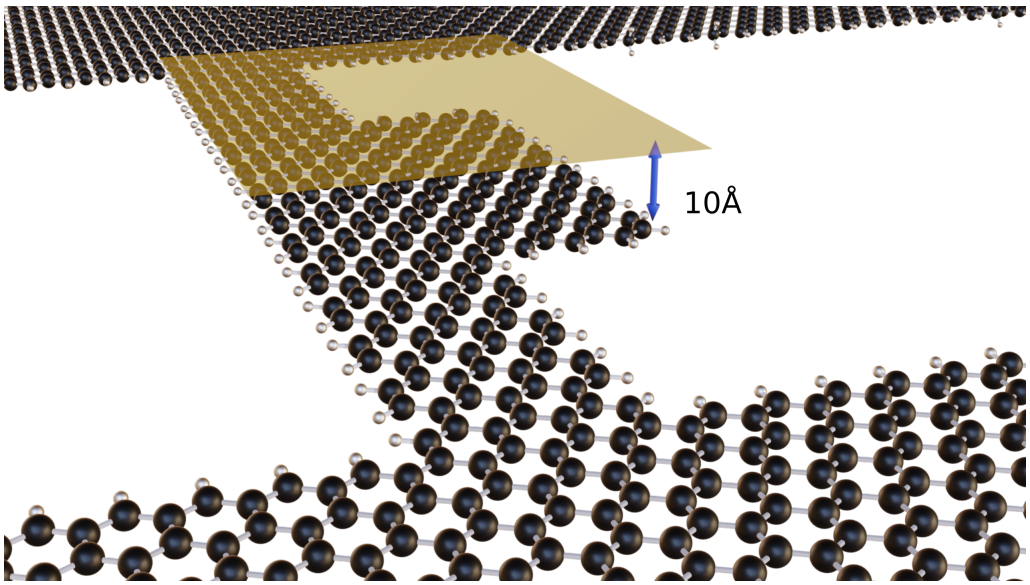


Figure 4.3: Lateral view of the system. The blue arrow indicates the 10Å distance between the 7-14-7 AGQD and the gate surface.

The transport calculations rely on the non-equilibrium Green's functions formalism as implemented in the Smeagol package.[134] Within this theoretical framework where the basis set is not orthogonormal, the energy-dependent retarded Green's function is given by

$$G^r(E) = \lim_{\eta \to 0^+} \left[(E + i\eta)S_S - H_S - \Delta_L(E) - \Delta_R(E)\right]^{-1}, \tag{4.1}$$

where H_S and S_S are the Hamiltonian and overlap matrices for the scattering

the references [77, 137, 138].

region, and $\Delta_{L(R)}$ represent the hybridization functions accounting for the coupling with the leads. The density of states (DOS) and projected density of states (PDOS) onto an atomic orbital i were obtained directly from the Green's function,

$$PDOS(E) = -\frac{1}{\pi} Im\{[G_S S_S]_{ii}\}, \tag{4.2}$$

$$DOS(E) = -\frac{1}{\pi} Im\{Tr\,[G_S S_S]\}. \tag{4.3}$$

Quantities such as the differential conductance G, the electronic thermal conductance κ_{el} and the Seebeck effect can be calculated from equations (3.80), (3.81) and (3.83). The efficiency of the thermoelectric device can be obtained from the figure of merit presented in equation (3.85), however, in this work we initially consider the upper limit of ZT, which is obtained by disregarding the phonon contribution in the thermal conductivity. Thus, substituting equations (3.80), (3.81) and (3.83) into equation (3.85) we obtain a reduced expression for the figure of merit,

$$ZT = \left(\frac{K_0 K_2}{K_1^2} - 1\right)^{-1} \tag{4.4}$$

It is worth mentioning that our methodology allows us to simulate the effect of a finite voltage-gate on the figure of merit as we discuss in the next section.

4.3 Discussion

We begin our discussion by investigating the electronic structure of the system at zero temperature and zero voltage-gate. In figure 4.4a, we present the density of states of a 7-14-7 AGQD. As expected, due to quantum confinement, localized levels can be observed around the Fermi level. In order to provide further insights regarding the origin of these states, we also show the density of states of a pristine 7-AGNR (black dotted-line). We can clearly see that six prominent electronic states of the 7-14-7 AGQD reside inside the energy gap of the pristine ribbon. Wang *et al* suggested that two of these states can be related to interface states between the 7- and 14-GNR segments while the other 4 states are directly related to the 14-GNR segments[33]. In Figure 4.4b, we depict the electronic wave function at the band edge which are labeled as 1 and 2. One can clearly see that the wave function

is symmetrically distributed in the central region of the AGQD, demonstrating its direct relation with the 14-AGNR segment. It is interesting to note that the strong electron localization in the inner region induces a weak coupling between the 7-14-7 AGQD states and the leads. This channel-lead coupling effect for GQDs of different widths and lengths has been widely addressed and their drastic effects on the transport gap have been recently reported.[131]

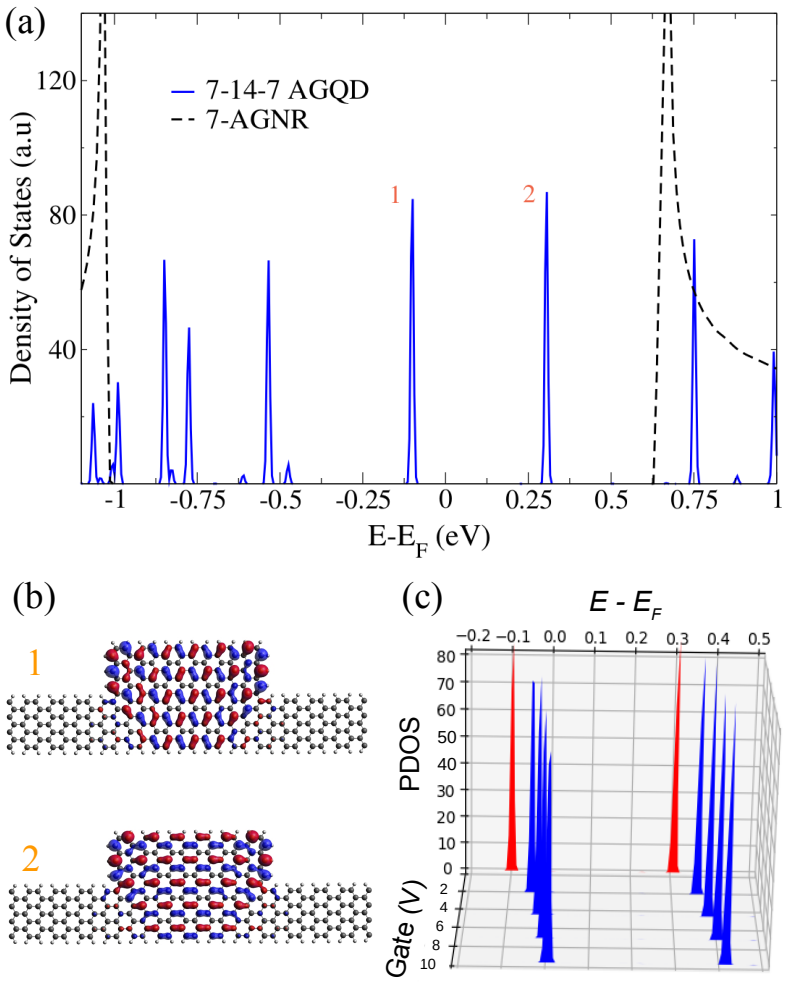


Figure 4.4: (a) Density of states of the 7-14-7 quantum dot AGNR (blue lines) and the pristine 7-AGNR (black-dashed lines). (b) Electronic wave function at the band edge. The upper (lower) figure correspond to the highest (lowest) state in the valence (conduction) band. (c) Evolution of the edge states due to the presence of a gate voltage. The red curve indicates the case in which the external gate potential is zero.

We now explore the effects of the gate voltage on the edge states of the 7-14-7 AGQD. As shown in Figure 4.4c, a finite gate voltage shifts the edge states towards higher values. Consequently, the electronic state close to the Fermi level, the

relevant one for the conduction, possesses a reduced $|E - E_F|$ value compared with the case in which the $V = 0$. Close inspection of eq. (9), allows us to anticipate that the reduction of $|E - E_F|$, which strongly weights K_1 and K_2, will induce a considerable enhancement of the thermopower.

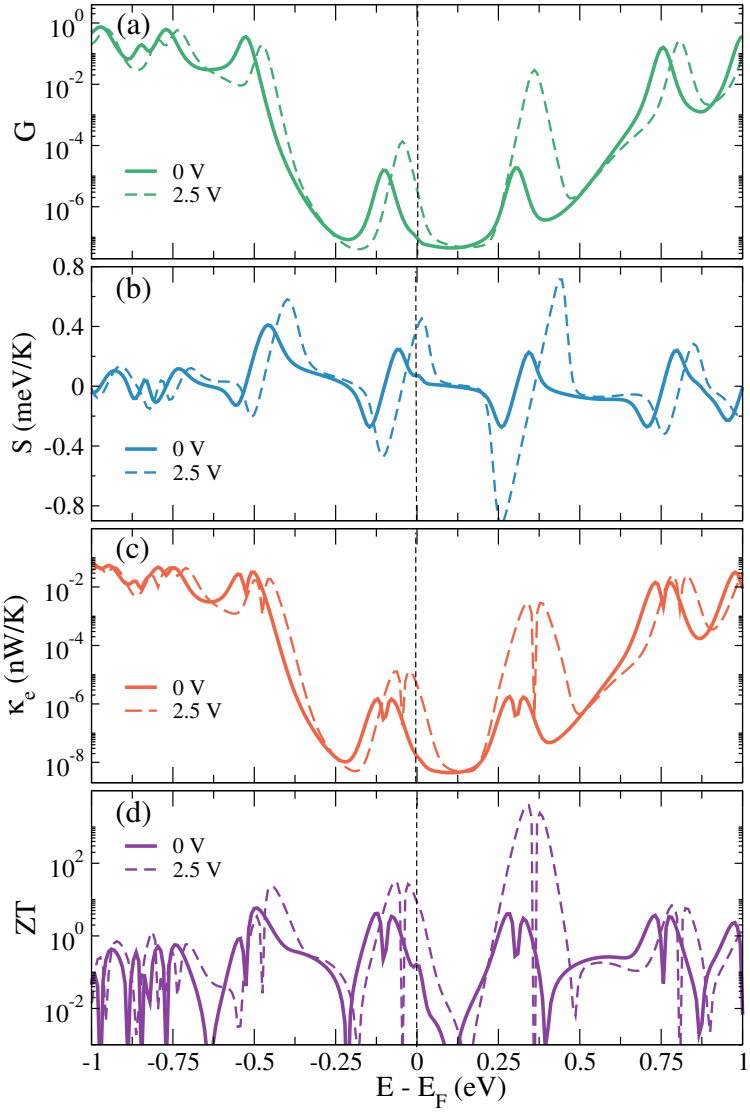


Figure 4.5: Thermoelectric properties of the 7-14-7 AGQD as a function of the energy, calculated at 100 K and for zero gate voltage (solid lines) and finite gate voltage of 2.5 V (dashed lines). From top to bottom, a) the conductance G, b) the Seebeck coefficient S, c) the electronic thermal conductivity k_e, and d) the figure of merit ZT.

We then proceed by analyzing the parameters that define the thermoelectic performance. In order to make our analysis easier, we initially avoid broad features due to temperature effects by considering the low temperature case (T=100 K). In Figure 4.5, for a finite gate voltage (2.5 V), all the thermoelectric parameters that

define ZT around the band edge, gets broader and significantly increases with respect the zero gate case. As mentioned above, the enhancement of the Seebeck coefficient with the voltage is a direct consequence of the reduction of the $|E - E_F|$ with the voltage. It is important to point out that the inclusion of an external gate is equivalent to an effective shift of the levels of 100 meV. Nonetheless, we can clearly see that the effect of the gate not only shifts the levels but significantly changes the electronic structure due to charge rearrangements. In fact, the conductance peaks around the Fermi level, for instance, are enhanced. Although the electron thermal conductivity enhances around the Fermi level– an undesirable trend– this effect is compensated by a considerable increase in the conductance. The competition between the parameters mentioned above, causes the overall increase of ZT around the Fermi level, presenting a surprising upper performance in the energy range from 0.25 - 0.5 eV above the Fermi level. This suggests that *n*-doped AGQDs may have significantly enhanced ZT values.

The effect of a finite gate voltage at the Fermi level is presented in Figure 4.6. Clearly, as V_g increases, the conductance in the channel increases. This rise on the conductance suggest that the conducting GQD states in the channel hybridize with those from the leads, which strengthen the channel-to-lead coupling. To gain further insight about this phenomenon, in [140], we analyzed the conductance as a function of energy for different gate voltages. There, one can clearly see that as the gate voltage increases, the conductance curve around the Fermi level gets broader, a clear signature of the enhancement of the channel-to-lead coupling. Moreover, we notice that the effect of increasing the gate voltage on GQDs resembles the effect of reducing the channel length, a phenomenon that has been recently demonstrated in a variety of GQDs formed by lateral junction of small AGNRs.[131]

On the other hand, the Seebeck coefficient reaches its maximum at low-voltage regime ($V_g \leq 2.5V$). In addition, the electron thermal conductivity tends to rapidly increase as the gate-voltage increases. In the optimal range for the thermopower, its enhancement is about two orders of magnitude, however this undesirable behavior is compensated by the increase in the conductance.

Finally, in Figure 4.6d, we present the temperature effects on the figure of merit. Given that our calculations do not include the phonon contribution to the thermal conductivity, our estimated values must be treated as the upper limit for ZT. Nevertheless, previous theoretical studies in AGNR found that the phonon contribution to the thermal conductivity can be as high as 65 % (98 %) for 6-AGNR[141] (15-AGNR),[142, 143] nanostructures with similar widths as the ones

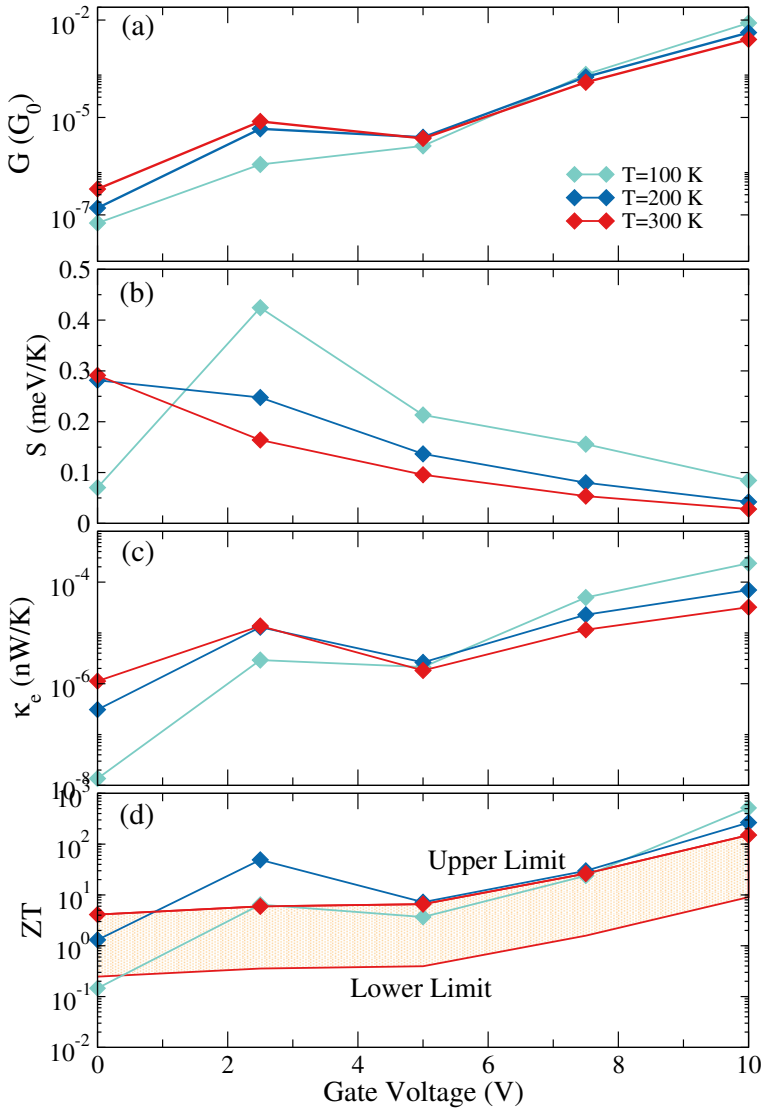


Figure 4.6: Thermoelectric parameters of the 7-14-7 AGQD, evaluated at the Fermi energy, as a function of the applied gate voltage V_g for different temperatures. From top to bottom, a) the conductance G, b) the Seebeck coefficient S, c) the electronic thermal conductivity k_e, and d) the figure of merit ZT showing its upper and lower limit at $T = 300$ K.

that constitute the AGQD studied here. Based on these theoretical results, we are able to establish the lower limit for ZT by assuming the ratio, $\kappa_e/\kappa = 0.06$, which implies that the phonon contribution to the thermal conductivitity is as high as 94 %.

As can be seen from Figure 4d, at zero voltage, the increase of temperature causes a significant enhancement in the maximum value of ZT, which can undergo changes in more than one order of magnitude, i.e, from 0.15 at low-temperatures to ≈ 4 at room temperature. While the upper limit of ZT can be enhanced up to

two orders of magnitude when increasing the gate voltage, it is interesting to note that the lower limit follows the same trend. In fact, at room temperature and V_g = 0 V, the lower bound of ZT is ≈ 0.25. By changing the gate voltage smoothly up to 5 V one can increase this value up to 0.4. More strikingly, for a gate voltages of 7.5 V, the lower bound of ZT can be enhanced up to 1.58, and even more for a gate voltage of 10 V. This set of results clearly highlights the potential that 7-14-7 AGQD may hold for thermoelectric applications.

4.4 Conclusions

In summary, based on *ab initio* calculations and the Green's function formalism, we provided a comprehensive theoretical description of the electronic and thermoelectric properties of the so-called 7-14-7 quantum dot in graphene nanoribbon. We show that the electronic states at the band edge are highly localized in the inner region of the quantum dot, instead of the borders as observed in graphene nanoribbons. At zero voltage-gate and room temperature, we estimate the lower bound for ZT to be 0.25. The lower bound can be tuned by applying a gate voltage, which allow to reach a surprising value of $ZT \approx 1.5$ at V = 7.5 V. The overall results suggest that quantum dots in graphene nanoribbons might be promising candidates for thermoelectric applications.

Chapter 5

Generalized Landauer-Buttiker formula: Effective transmission for systems with many-body interactions

As we mentioned before, given a quantum system that can be approximated by a non-interacting Hamiltonian, the system's conductance can be readily calculated by the Landauer-Buttiker or the equivalent Fisher-Lee [144] approach. However, when many-body interactions are present, the definition of such quantity is not as straightforward as in the non-interacting case, and any proposed effective transmission must account for both coherent and incoherent scattering. There are in the literature one exact (Meir-Wingreen transmission) and other ansatz-based proposals for an effective transmission capable of accounting for many-body effects. All of them, however, with a restricted range of applicability.

In this work, by using the method of Non-Equilibrium Green Functions, it will be shown how the conservation of flux of charge can be used to deduce an equation constraining the lesser component of the self-energy and the anti-Hermitian part of the retarded component. This constraint equation will then be used to present a proposal for an effective transmission probability capable of dealing with the most general interacting case. In addition to the general transmission equation, the limiting case of incoherent transport is also studied. At this point, the equations for incoherent transport proposed by Meir-Wingreen [35] and Beenakker [36] are derived as a limiting case of a more general incoherent transport theory.

5.1 Introduction

Within the general transport theory the electrical current and other transport

properties can be directly related to real time components of Non-Equilibrium Green Functions, as is shown by the general current equation (3.68). The problem greatly simplifies in the particular case where the nanostructure is described by a non-interacting Hamiltonian. In this case it is possible to find a closed form for the reduced density matrix of the system, which can then be used to write the current in terms of a transmission function, as was proposed in the Landauer-Buttiker approach and already demonstrated in chapter 3.

In the presence of many-body interactions the degree of complexity of the problem increases significantly, for now, the flow o electrons throught the nanostructure becomes correlated. In this case the relationship between the system's ocupation and its electronic structure is not as clear as in the non-interacting case, making the task of defining an generalized transmission function much more cumbersome.

In their seminal paper [145], Meir and Wingreen partially solved this problem by deriving a transmission function for interacting systems from the proposed general transport equation. The obtained transmission, however, is only valid in the so-called proportional coupling case, *i.e.* only when the coupling to left and right electrodes for any given energy varies by a constant factor.

Since then, attempts have been made to find a prescription for calculating a generalized transmission for interacting systems. In essence, the concept of a transmission function is purely non-interacting as it can be directly related to the quantum transmission probability amplitudes in the non-interacting case. So, the extension of such a concept to the interacting regime must be performed carefully, for now, it must account for both coherent and incoherent processes and elastic and inelastic scatterings, e.g. electron-electron and electron-phonon interactions. However, the description of transport in terms of an effective transmission gives a deeper insight into the problem, since it allows to define and visualize effective conduction channels and, as pointed by Ferretti et al. [146], it allow us to study the linear response regime based solely on equilibrium quantities.

In order to define an effective transmission it is necessary to have information on how the systems reduced density matrix relates to the retarded single particle Green functions. In this direction, studies have been carried out by focusing in the single level case considering both the low and finite bias regime [147], and also attempts were made to generalize these descriptions to the multilevel interacting problem [146, 148, 149].

In this chapter, we will present the issues faced by previous methodologies

and show how the steady state conservation of flux of charge may be used to constraint the functional dependence of the lesser interacting self-energy on the anti-Hermitean part of the retarded component. This constrain will latter be used to define a generalized effective transmission and an uncorrelated approximation. In order to elucidate the consequences of our analytical results, numerical calculations will be performed for the single and double Anderson impurity model in equilibrium. We will show the effect of asymmetric coupling and study the limiting cases of symmetric and strongly asymmetric couplings. The limiting case of sequential tunneling is also extensively studied.

The chapter has the following structure: In section 5.2 we present the exact Meir-Wingreen effective transmission and the Ng ansatz-based effective transmission, where we also show their respective range of application. In section 5.3 we demonstrate how the charge flux conservation can be used to deduce an equation relating the lesser, retarded and advanced components of the interacting self-energy. This relation is, then, used to define a generalized effective transmission. In section 5.4, in order to get a deeper physical insight into the transport problem, a theory of uncorrelated transport is proposed. In section 5.5 we study the regime of sequential tunneling, where we show how the differential conductance equation defined in the literature can be obtained as an approximation of the differential conductance equation reached from the general effective transmission and the uncorrelated effective transmission. In section 5.6 the derived expressions will be used to calculate the transmission for the single and double Anderson model.

5.2 Meir-Wingreen and the ansatz based effective transmission

By employing the Keldysh formalism of non-equilibrium Green's functions (already presented in chapter 3), Meir and Wingreen obtained the general current equation (3.68) which can be written for both the left and right leads as

$$J_\beta = \frac{ie}{\hbar}\int \frac{d\omega}{2\pi} Tr\{\Gamma_\beta(\omega)[G^<(\omega) + (G^r(\omega) - G^a(\omega))f_\beta(\omega)]\}. \quad \beta = L;R \tag{5.1}$$

Equation (5.1) can also be written in terms of the interacting self-energy Σ_{int}:

$$J_\beta = \frac{ie}{\hbar}\int \frac{d\omega}{2\pi}[Tr\{\Gamma_\beta G^r \Gamma_{\bar{\beta}} G^a\}(f_{\bar{\beta}} - f_\beta) + Tr\{\Gamma_\beta G^r(\Sigma^<_{int} + (\Sigma^r_{int} - \Sigma^a_{int})f_\beta)G^a\}]. \tag{5.2}$$

From the above equation it can be easily seen that the current calculation reduces to the Buttiker-Landauer expression (3.74) for the non-interacting case

$$J_\beta = \frac{ie}{\hbar}\int \frac{d\omega}{2\pi} Tr\{\Gamma_\beta G^r \Gamma_{\bar{\beta}} G^a\}(f_{\bar{\beta}} - f_\beta); \quad \beta = L, R. \tag{5.3}$$

For the most general case where strong correlations due to many-body interactions are present the above equation no longer holds, and the calculation of $G^<$ and G^r poses both theoretical and computational challenges. However, even for these cases, a further simplification of (5.1) may be obtained if the interacting region couples proportionally to both leads. This condition can be mathematically expressed as $\Gamma_R = \lambda\Gamma_L$, a situation known as proportional coupling. To simplify equation (5.1) in the proportional coupling regime first note that the charge conservation allows us to write

$$J_L = -J_R \;\rightarrow\; J_L = (1+x)J_L + xJ_R\,; \quad x \in \mathbb{R}. \tag{5.4}$$

So, in order to eliminate the lesser Green's function from the equation for the current, we may choose x such that $x + (1+x)\lambda = 0$. In this case we obtain

$$T(\omega, V) = Tr\left\{\left(\frac{\Gamma_L\Gamma_R}{\Gamma_L + \Gamma_R}\right)(-2iIm[G^r(\omega)])\right\} \tag{5.5}$$

This is the widely used Meir-Wingreen transmission and it may be very useful when we are dealing with interacting systems[150, 151]. However, it has its drawbacks. First of all it is important to observe that the condition of proportional coupling can be generalized to accommodate centrosymmetric systems (shown in appendix C) however, even with this generalization, this condition constitutes a strongly restrictive regime. It also can't be generally applied for systems out of equilibrium, as the applied bias may break the inversion symmetry.

Attempts of generalizing this result to the non-proportional coupling regime was proposed by Ferretti et al. [146] and Sergueev et al. [149]. Their solution was based on an ansatz proposed by Ng [147] in which the lesser(greater) component of the single level scalar self-energy Σ is related to the lesser(greater) component

of the hibridization function Σ_0:

$$\Sigma^{<} = \Sigma_0^{<}\Lambda, \tag{5.6}$$

$$\Sigma^{>} = \Sigma_0^{>}\Lambda, \tag{5.7}$$

where

$$\Sigma_0 = \Delta_R + \Delta_L, \tag{5.8}$$

$$\Sigma = \Sigma_0 + \Sigma_{int}. \tag{5.9}$$

Substituting equations (5.6) and (5.7) into the general relation

$$\Sigma^{>} - \Sigma^{<} = \Sigma^{r} - \Sigma^{a}, \tag{5.10}$$

and solving for $\Sigma^{<}$ we obtain

$$\Sigma^{<} = \Sigma_0^{<}\Lambda = (\Gamma_R f_R + \Gamma_L f_L)\Big(1 + \frac{1}{\Gamma_R + \Gamma_L + 2\delta}\Gamma_{ee}\Big), \tag{5.11}$$

where $\Gamma_{ee} = i(\Sigma^r - \Sigma^a)$ and δ is an infinitesimal matrix used to guarantee that $\Gamma_R + \Gamma_L$ has an inverse for all energies. From the above expression the interacting lesser self-energy can be readily identified:

$$\Sigma_{int}^{<} = (\Gamma_R f_R + \Gamma_L f_L)\frac{1}{\Gamma_R + \Gamma_L + 2\delta}\Gamma_{ee}. \tag{5.12}$$

Once we have (5.12), the current may be readily calculated from (5.2)

$$J_\beta = \frac{ie}{\hbar}\int \frac{d\omega}{2\pi} Tr\{\Gamma_\beta G^r \Gamma_{\bar{\beta}} \Lambda G^a\}(f_{\bar{\beta}} - f_\beta); \quad \beta = L, R, \tag{5.13}$$

where we can define a Landauer-like effective transmission

$$T = Tr\{\Gamma_\beta G^r \Gamma_{\bar{\beta}} \Lambda G^a\} \tag{5.14}$$

Equations (5.12) and (5.14) constitute two important results: i) the former may be viewed as a generalization of the fluctuation-response theorem to the non-equilibrium case and ii) the latter is a derived effective transmission for the many-body interacting case. As pointed out by Ferretti et al. [146], (5.14) indicates that the addition of many-body interactions not only renormalize the Green's

functions used for transport calculations but also introduces Λ in the effective transmission. That can be seen as an "renormalization" of coupling between the interacting region and the leads: $\Gamma_R \to \Gamma_R\Lambda$.

The ansatz used to derive equations (5.12) and (5.14) are supported by the fact that it leads to a conserved flux of charge, that it is exact in the absense of interactions and also at thermodynamic equilibrium, recovering the fluctuation-dissipation theorem. It is also important to observe that the effective transmission (5.14) is equivalent to the exact one obtained by Meir-Wingreen for the case of proportional coupling.

Differently from the non-interacting case, where (5.11) leads to the exact Buttiker-Landauer equation, the exactness of the ansatz in equilibrium doesn't necessarily imply the validity of (5.14) at zero bias. Indeed, observe that the lesser interacting self-energy is an anti-Hermitean matrix for both equilibrium and non-interacting cases and we may expect this property to hold for the most general case since it guarantees a positive definite spectral intensity, however, this property is only met for the ansatz in the single level and proportional coupling regimes. Therefore, we can not expect the ansatz to be valid beyond these two limiting cases. The same problem appears in the derived transmission function due to the non-Hermiticity of the renormalized coupling $\Lambda\Sigma_R$, which allows for an imaginary transmission.

5.3 Charge Flux Conservation and the Effective Transmission

Still focusing on the two-probe problem, we move to propose a generalized effective transmission function capable of dealing with the most general multilevel non-proportional coupling regime. The first step in this direction consists of observing that the charge flux conservation condition leads us to an equation which imposes a constraint between functionals of the lesser, greater and advanced components of the systems Green's functions. To see this, observe that from equation (5.1) and (5.4) we have

$$\int \frac{d\omega}{2\pi} Tr\{(\Gamma_R + \Gamma_L)(\omega)G^<(\omega) + (\Gamma_L f_L + \Gamma_R f_R)(G^r(\omega) - G^a(\omega))\} = 0 \quad (5.15)$$

The integrand of (5.15), which will be denoted by $A(\rho_{LL}, \rho_{RR}, H)$, is a function of the independent operators $\rho_{LL(RR)}$ and H that correspond respectively, to left(right) leads density of states, and the systems scattering region Hamiltonian. Note that these independent operators completely define the problem and that $A(\rho_{LL}, \rho_{RR}, H)$ depends on them via $G^<, G^r, G^a, \Gamma_L$ and Γ_R.

Equation (5.15) defines an important relation between the lesser, retarded and advanced components of the Green's function, however, this relation is in integral form. In order to establish a direct relation between these quantities we will define the functional

$$S \equiv \int \frac{d\omega}{2\pi} A(\rho_{LL}, \rho_{RR}, H). \tag{5.16}$$

Now, observe that by making an infinitesimal variation in one of the defining parameters of the model, lets say $[\rho_{LL}]_{ij}$, we obtain:

$$[\rho'_{LL}(\omega)]_{mn} = [\rho_{LL}(\omega)]_{mn} + \delta_{m,i}\delta_{n,j}\delta\rho(\omega), \tag{5.17}$$

being $\delta\rho(\omega)$ an arbitrary infinitesimal function. Then the response in the functional will be given by[152]

$$\delta S(\rho_{LL}, \rho_{RR}, H) = \int \frac{d\omega}{2\pi} \frac{\partial\big(A(\rho_{LL}, \rho_{RR}, H)\big)}{\partial[\rho_{LL}]_{ij}} \delta\rho(\omega). \tag{5.18}$$

We may now use the arbitrariness of $\delta\rho(\omega)$ to define it such that

$$\delta\rho(\epsilon) \begin{cases} = 0 \text{ for } \omega < \omega_0 \\ = \eta(\omega)\epsilon \text{ for } \omega_0 \leq \omega \leq \omega_1 \\ = 0 \text{ for } \omega_1 < \omega \end{cases}, \tag{5.19}$$

with ϵ an infinitesimal number and $\eta(\omega)$ an arbitrary diferentiable function, with $\eta(\omega_0) = \eta(\omega_1) = 0$. In this case, equation (5.18) becomes

$$\delta S = \epsilon \int_{\omega_0}^{\omega_1} \frac{d\omega}{2\pi} \frac{\partial\big(A(\rho_{LL}, \rho_{RR}, H)\big)}{\partial[\rho_{LL}]_{ij}} \eta(\omega). \tag{5.20}$$

Note that equation (5.15) is a consequence of the assumption of steady state conservation of flux of charge and, as such, is valid independently of the system for which it is applied, so:

$$S(\rho'_{LL}, \rho_{RR}, H) = S(\rho_{LL}, \rho_{RR}, H) = \delta S = 0. \tag{5.21}$$

By substituting equation (5.21) in equation (5.20), and considering the continuity of the functions $G^<(\omega)$ (density of occupation) and $G^r(\omega) - G^a(\omega)$ (density of states) on the real axis, from the fundamental lemma of calculus of variations we have that [152]

$$\left.\frac{\partial\big(A(\rho_{LL},\rho_{RR},H)\big)}{\partial[\rho_{LL}]_{ij}}\right|_{(\rho_{LL},\rho_{RR},H)} = 0, \tag{5.22}$$

which is valid in the arbitrary closed domain (ω_0,ω_1). Integrating equation (5.22) with relation to $[\rho_{LL}]_{ij}$ yields:

$$A(\rho_{LL},\rho_{RR},H) = g([\rho_{LL}]_{mn},[\rho_{RR}]_{pq},H);\ \ (mn)\neq(ij). \tag{5.23}$$

This same procedure can be repeated for any of the independent parameters such that $g(\rho_{LL},\rho_{LL(RR)},H)$ must be a constant. Note however that, in this case, the only function f which satisfies equation (5.15) is $g=0$, leading us to

$$A(\rho_{LL},\rho_{RR},H) = 0 \tag{5.24}$$

Equation (5.24) is a very important relation, as it allows us to impose a constraint directly in the functional dependence of $G^<$ on the functions G^r, G^a, Γ_L and Γ_R. This equation can be written in terms of the interacting self-energy by using

$$G^< = G^r\Sigma^<G^a = G^r(i\Gamma_R f_R + i\Gamma_L f_L + \Sigma^<_{int})G^a, \tag{5.25}$$

and

$$G^r - G^a = G^r(-i\Gamma_R - i\Gamma_L - i\Gamma_{ee})G^a. \tag{5.26}$$

Substituting equation (5.25) and (5.26) in equation (5.24) we obtain

$$\begin{aligned} Tr\big\{i(\Gamma_R+\Gamma_L)G^r(\Gamma_L f_L+\Gamma_R f_R)G^a - (\Gamma_L f_L+\Gamma_R f_R)G^r(\Gamma_R+\Gamma_L)G^a\big\}+ \\ Tr\big\{(\Gamma_R+\Gamma_L)G^r\Sigma^<_{int}G^a - i(\Gamma_L f_L+\Gamma_R f_R)G^r\Gamma_{ee}G^a\big\} = 0, \end{aligned} \tag{5.27}$$

Thus, the first term of equation (5.27) cancel out, leading to:

$$Tr\big\{(\Gamma_R+\Gamma_L)G^r\Sigma^<_{int}G^a - i(\Gamma_L f_L+\Gamma_R f_R)G^r\Gamma_{ee}G^a\big\} = 0. \tag{5.28}$$

Despite being more restrictive than Equation (5.27) due to the assumption of microscopic time reversal symmetry, Equation (5.28) has the same level of importance of the former as it directly constrains the functional dependence of $\Sigma^<_{int}$ on Σ^r_{int}

and Σ^a_{int}.

It's important to point out that, despite being a strong constraint, equation (5.28) doesn't completely fixes $\Sigma^<_{int}$ for the most general case. However, for the special cases of single level and proportional coupling this equation leads to an exact expression for the interacting self-energy. In the single level case equation (5.28) can be exactly solved for $\Sigma^<_{int}$, leading to

$$\Sigma^<_{int} = i\frac{(\Gamma_L f_L + \Gamma_R f_R)}{(\Gamma_R + \Gamma_L)}\Gamma_{ee}. \tag{5.29}$$

For the special case of the proportional coupling regime ($\Gamma_R = \lambda\Gamma_L$),

$$\Sigma^<_{int} = i\frac{(f_L + \lambda f_R)}{1+\lambda}\Gamma_{ee}. \tag{5.30}$$

In the general case, $\Sigma^<_{int}$ can only be solved if additional constraints are imposed. In order to do so, we will list general properties expected to hold for the interacting self-energy:

$$\Sigma^<_{int} = -[\Sigma^<_{int}]^\dagger, \tag{5.31}$$

$$\Sigma^<_{int}\big|_{f_L=f_R=f_0} = -(\Sigma^r_{int} - \Sigma^a_{int})f_0, \tag{5.32}$$

$$\Sigma^<_{int}\big|_{non-interacting} = 0, \tag{5.33}$$

$$\lim_{\Gamma_{L(R)}\to 0} \Sigma^<_{int} = -(\Sigma^r_{int} - \Sigma^a_{int})f_{R(L)}, \tag{5.34}$$

$$\Sigma^>_{int} - \Sigma^<_{int} = \Sigma^r_{int} - \Sigma^a_{int}. \tag{5.35}$$

Condition (5.31) assures a positive definite spectral intensity, while condition (5.32) is nothing but the fluctuation dissipation theorem. Condition (5.33) ensures a null $\Sigma^<_{int}$ for non-interacting systems, while condition (5.34) ensures the recovery of thermodynamic equilibrium in case one of the leads is disconnected. Finally, Equation (5.35) guarantees that $\Sigma^<_{int}$ solved from Equation (5.28), and $\Sigma^>_{int}$ solved from an analogously derived equation

$$Tr\{(\Gamma_R + \Gamma_L)G^r\Sigma^>_{int}G^a - i(\Gamma_L(f_L - 1) + \Gamma_R(f_R - 1))G^r\Gamma_{ee}G^a\} = 0 \tag{5.36}$$

obeys the general property of Equation (5.10). Observe now that Equation (5.28)

may be writen as

$$Tr\left\{(\Gamma_R+\Gamma_L)G^r\Sigma^<_{int}G^a - i\left((\Gamma_L-\Gamma_R)\frac{(f_L-f_R)}{2}+(\Gamma_R+\Gamma_L)\frac{(f_R+f_L)}{2}\right)G^r\Gamma_{ee}G^a\right\}=0 \tag{5.37}$$

In this form, equation (5.37) allows for a clear distinction between the contributions to $\Sigma^<_{int}$ comming from the average and the difference of the Fermi-Dirac distributions of each lead. It's interesting to observe that the term containing the average of the distributions is also related to the average of the coupling $\Gamma_+ = \frac{\Gamma_L+\Gamma_R}{2}$, while the term containing the difference of distributions also contains the difference of the coupling $\Gamma_- = \frac{\Gamma_L-\Gamma_R}{2}$. One solution of $\Sigma^<_{int}$ to (5.37) satisfying all the requirements is

$$\begin{aligned}\Sigma^<_{int} &= -(\Sigma^r_{int}-\Sigma^a_{int})\frac{f_R+f_L}{2}\\ &+i\left[(\Gamma_L+\Gamma_R)^{\frac{1}{2}}G^r\right]^{-1}\left[\Gamma_L^{\frac{1}{2}}G^r\Gamma_{ee}G^a\Gamma_L^{\frac{1}{2}}-\Gamma_R^{\frac{1}{2}}G^r\Gamma_{ee}G^a\Gamma_R^{\frac{1}{2}}\right]\left[G^a(\Gamma_L+\Gamma_R)^{\frac{1}{2}}\right]^{-1}\frac{f_L-f_R}{2}\end{aligned} \tag{5.38}$$

Equations (5.27) and (5.38) are both results of significant importance in this chapter. The former constitutes an exact constraint on different components of the interacting self-energy from which it is possible to derive exact expressions for $\Sigma^<_{int}$ in the single level and proportional coupling regimes. The latter constitutes a solution (not necessarily unique) to $\Sigma^<_{int}$ in the general case which, can be viewed as a generalization of the fluctuation response theorem to the non-equilibrium regime, and can also be used to define a generalized transmission function:

$$\begin{aligned}T = Tr\{\Gamma_R G^r\Gamma_L G^a\} &+ \frac{1}{2}Tr\left\{\Gamma_L^{1/2}(\Gamma_R+\Gamma_L)^{-1/2}\Gamma_R(\Gamma_R+\Gamma_L)^{-1/2}\Gamma_L^{1/2}G^r\Gamma_{ee}G^a\right\}\\ &+\frac{1}{2}Tr\left\{\Gamma_R^{1/2}(\Gamma_R+\Gamma_L)^{-1/2}\Gamma_L(\Gamma_R+\Gamma_L)^{-1/2}\Gamma_R^{1/2}G^r\Gamma_{ee}G^a\right\}\Big\}\end{aligned} \tag{5.39}$$

Where (5.39) can be obtained by substituting (5.38) in (5.2) for J_R.

5.4 Uncorrelated Transport

In equilibrium, the fluctuation-dissipation theorem implies in Equation (5.32).

In this case, we can observe that the relation between lesser and anti-Hermitean components of the self-energy is component-wise and has a clear physical interpretation,

$$[\Sigma^{<}_{int}]_{ii}(\epsilon) = \underbrace{[\Gamma_{ee}(\epsilon)]_{ii}}_{\tau^{-1}} \cdot \underbrace{f_{FD}(\epsilon)}_{\text{ocupation}} . \tag{5.40}$$

The first term is a measure of the scattering rate of particles at energy ϵ due to level i, which is proportional to the thermal occupation and inversely proportional to the lifetime of a particle of energy e due to level i. The simplicity of this equation comes from the fact that, in equilibrium, the average occupation is dictated only by thermal fluctuations.

In the non-equilibrium regime the situation becomes much more cumbersome. In that case, elastic coherent tunneling between different levels of the scattering region will induce correlations in the occupations of these levels in such a way that the scattering rate of a particle at energy ϵ due to a level j will depend not only on the contributions coming from the lifetime of the level j but also from the others levels. In other words, the dependence of the lesser component on the anti-Hermitean component will no longer be component-wise, as is shown by Equation (5.38).

On the other hand, if we neglect the correlations between the coherent tunneling processes and the incoherent inner scatterings within the scattering region, the only difference between the equilibrium and non-equilibrium regime will be a change in the average occupation appearing in Equation (5.40). In other words, we may expect the relation between the lesser and anti-Hermitean parts of the self-energy to be componentwise,

$$[\Sigma^{<}_{int}]_{ij} \equiv h([\Gamma_{ee}]_{ij}). \tag{5.41}$$

This can be used to completely solve the constraint Equation (5.28) and the solution to $\Sigma^{<}_{int}$ is obtained for this approximation as

$$[\Sigma_{int}]^{<}_{ij} = i\frac{[G^r(\Gamma_R f_R + \Gamma_L f_L)G^a]_{ij}}{[G^r(\Gamma_R + \Gamma_L)G^a]_{ij}}[\Gamma_{ee}]_{ij}. \tag{5.42}$$

The physical meaning of Equation (5.42) becomes clear when we look at the diagonal elements. The terms $[G^r(\Gamma_R f_R + \Gamma_L f_L)G^a]_{ii}$ and $G^r(\Gamma_R + \Gamma_L)G^a]_{ii}$ represent, respectively, the density of ocupation and the density of states arising from the coupling with the leads, both projected o level "i". So, the ratio between these two

quantities corresponds to the fraction of occupation projected on the respective level.

Now we can see that, in this uncorrelated approximation, the out-of-equilibrium regime is described by a distribution function which accounts not only for the thermal fluctuations but also for the population imbalance caused by the tunneling events at different chemical potentials. We also note that since the strenght of coupling with the leads is a property of the level, the distribution will be level dependent:

$$f_{FD} \rightarrow [f_{NE}]_{ij} \equiv \frac{[G^r(\Gamma_R f_R + \Gamma_L f_L)G^a]_{ij}}{[G^r(\Gamma_R + \Gamma_L)G^a]_{ij}} \tag{5.43}$$

Using equation (5.42) it is possible to define a simpler uncorrelated transport theory. Indeed, by substituting this equation in Equation (5.2), the following expression for the transmission is obtained

$$T = Tr\{\Gamma_R G^r \Gamma_L G^a\} + \sum_{ij} \frac{[G^r \Gamma_L G^a]_{ij}[G^r \Gamma_R G^a]_{ij}}{[G^r(\Gamma_R + \Gamma_L)G^a]_{ij}} [\Gamma_{ee}]_{ij}. \tag{5.44}$$

Observe that in the limiting case of $\Gamma_{ee} >> (\Gamma_L + \Gamma_R)$ and diagonal Γ_{ee}, the previous equation reduces to:

$$T = \sum_i \frac{[\Gamma_L]_{ii}[\Gamma_R]_{ii}}{[(\Gamma_R + \Gamma_L)]_{ii}} (G^r_{ii} - G^a_{ii}). \tag{5.45}$$

This limiting case will be studied in the next section.

5.5 Sequential Tunneling Transport

In this section we are going to show how the transport equations for the, so called, sequential tunneling regime can be obtained both from the general equation (5.39) and the uncorrelated approximation (5.45). This regime is characterized by the assumption that the time between tunneling events is the largest time scale in the problem. In other words, the time spent in the scattering region is much larger than the dephasing time due to many-body scatterings.

The description of the transport properties in this regime can be performed by the diferential conductance equations proposed by Beenaker [36] and Meir-Wingreen [35]. Both equations were proposed in the context of describing the conductance in weakly coupled quantum dots, but the first was proposed as a solution to the master equation while the latter was proposed using NEGF. In

addition to the assumption of incoherent tunneling in and out of the dot, in both formulations any lead-induced coherence among the energy levels of the scattering region was also neglected.

The diferential conductance formula proposed by Meir-Wingreen in this regime is:

$$\sigma = \frac{e^2}{h}\sum_i \int d\epsilon f'_{FD}(\epsilon)\frac{[\Gamma_L]_{ii}(\epsilon)[\Gamma_R]_{ii}(\epsilon)}{[\Gamma_R(\epsilon)+\Gamma_L(\epsilon)]_{ii}}(G^r_{ii}-G^a_{ii}). \tag{5.46}$$

This same equation can be derived from general transmission (5.39) if we apply the same assumptions used to propose (5.46). Indeed, the assumption of long time between tunneling events implies that $\Gamma_{ee} >> \Gamma_L + \Gamma_R$ and this condition can be used to write:

$$G^r - G^a = iG^r(\Gamma_R + \Gamma_L + \Gamma_{ee})G^a \approx iG^r\Gamma_{ee}G^a \tag{5.47}$$

In addition to that, neglecting the lead-induced coherence among the dots energy levels implies in zero tunneling-induced transition rate between these level. In other words, any out-of-diagonal element of the $\Gamma_{R(L)}$ matrices are being neglected,

$$\Gamma_{R(L)} \rightarrow \tilde{\Gamma}_{R(L)};\ \ [\tilde{\Gamma}_{R(L)}]_{ij} = \delta_{ij}[\Gamma_{R(L)}]_{ii} \tag{5.48}$$

By considering equations (5.47) and (5.48) in Equation (5.39) we obtain the following expression for transmission

$$T = \sum_i \frac{[\Gamma_L]_{ii}[\Gamma_R]_{ii}}{[(\Gamma_R+\Gamma_L)]_{ii}}(G^r_{ii}-G^a_{ii}). \tag{5.49}$$

which will result in the Meir-Wingreen expression for the differentail conductance (5.46). It can be easily shown that this same expression for the differential conductance is obtained when we further assume a diagonal interacting self-energy in the transmission equation of uncorrelated transport, a condition that is usually met for Anderson-like models described in [35].

5.6 Applications: The single and Double Impurity Anderson Model

In order to explore the validity and potential applications of the proposed general effective transmission, we are going to study the transport properties of an electron-electron interacting system modeled by Anderson impurity model [20]. Firstly, we will concentrate on the single impurity model (SIAM). The Hamiltonian of this problem is given by

$$H_{SIAM} = \varepsilon(\hat{d}^{\dagger}_{\uparrow}\hat{d}_{\uparrow} + \hat{d}^{\dagger}_{\downarrow}\hat{d}_{\downarrow}) + U\hat{n}_{\uparrow}\hat{n}_{\downarrow} + \sum_{k\sigma}(\gamma_k \hat{a}^{\dagger}_{k\sigma}\hat{d}_{\sigma} + \gamma^{*}_{k}\hat{d}^{\dagger}_{\sigma}\hat{a}_{k\sigma}) + \sum_{k\sigma}\epsilon_k \hat{a}^{\dagger}_{k\sigma}\hat{a}_{k\sigma}, \quad (5.50)$$

where $\hat{d}^{\dagger}_{\alpha}(\hat{d}_{\alpha})$ corresponds to the creation(annihilation) of an impurity electron with quantum number α, $\hat{a}^{\dagger}_{\alpha}(\hat{a}_{\alpha})$ corresponds to the creation(annihilation) of one electron of the bath with quantum number α and $\hat{n}_{\alpha} = \hat{d}^{\dagger}_{\alpha}\hat{d}_{\alpha}$ refers to the number occupation operator. The parameters $\varepsilon, \epsilon_k, U$ and γ_k corresponds respectively to the energy of the impurity level, value of the energy level of the bath with quantum number k, value of the double occupation energy and the value of the coupling between the levels of the impurity and the levels of the bath. Later, the double impurity Anderson model will be taken into consideration. The main difference between the two is the fact that we are considering two impurities $d = \{1, 2\}$. Here we will consider the simple case whereby the two impurities are decoupled and $U_{ijkl} = U\delta_{ij}\delta_{kl}$. The approach can be generalized to include the more complex structure for the interaction, but it will not change our discussion.

$$H_{DIAM} = \sum_{d\sigma}\varepsilon_d(\hat{d}^{\dagger}_{d\uparrow}\hat{d}_{d\uparrow} + \hat{d}^{\dagger}_{d\downarrow}\hat{d}_{d\downarrow}) + U\sum_{d}\hat{n}_{d\uparrow}\hat{n}_{d\downarrow} + \sum_{dk\sigma}(\gamma_{kd}\hat{a}^{\dagger}_{k\sigma}\hat{d}_{d\sigma} + \gamma^{*}_{kd}\hat{d}^{\dagger}_{d\sigma}\hat{a}_{k\sigma}) + \sum_{k\sigma}\epsilon_k\hat{a}^{\dagger}_{k\sigma}\hat{a}_{k\sigma} \quad (5.51)$$

These models are widely used as a standard prototype in the investigation of the effects of many-body interactions, specially for the case where the many-body term can not be treated by standard pertubation theory. Even the SIAM, despite its simplicity, is highly non-trivial as there is no general method for solving the model in the entire range of the parameter space. In what concerns the temperature, the SIAM is characterized by the so called Kondo temperature T_K [21]. This quantity may be used to differentiate two distinct regimes: the hight temperaure ($T >> T_K$)

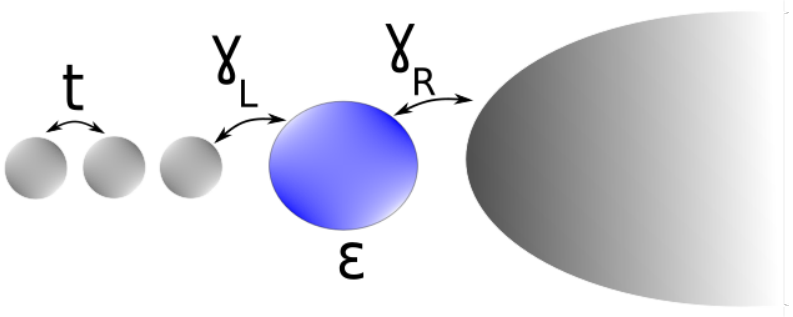


Figure 5.1: Single Anderson impurity coupled to a tight-binding semi-infinite wire (left electrode) and a single-band metal (right electrode).

and low temperaure ($T << T_K$) regimes. In this work we are going to focus in the high temperature regime but, since no assumption has been made in order to derive the effective transmission, it could be applied to the low temperature regime as well. In fact, we are going to restrict our analysis of the SIAM and DIAM to high temperature regime due to a limitation of the employed solver, and not the effective transmission.

There are different methods for solving the AIM [153], here we are going to employ the slave bosons technique [154]. This method is suited for the cases where the impurities are weakly coupled to the electron bath compared to the interaction, and it works by the principle that the isolated impurity Hamiltonian can be exactly diagonalized in terms of a basis of many-body states:

$$H_{IMP}|\alpha\rangle = E_\alpha \tag{5.52}$$

In the case of the SIAM, for instance, we have the following basis of eigenstates:

$$|0\rangle, |\uparrow\rangle, |\downarrow\rangle, |\uparrow\downarrow\rangle, \tag{5.53}$$

and the respective eigenenergies: 0, ε, ε, $2\varepsilon + U$. The creation and annihilation operators of these so called pseudo-particles can be related to the real electron creation and annihilation operators by

$$\hat{d}^\dagger_\sigma = \hat{s}^\dagger_\sigma \hat{b} + \hat{d}^\dagger_{\bar{\sigma}\sigma}\hat{s}_{\bar{\sigma}}, \tag{5.54}$$

where $\hat{b}^\dagger$, $\hat{s}^\dagger_\sigma$, $\hat{d}^\dagger_{\bar{\sigma}\sigma}$ are pseudoparticle creation operators responsible for creating over the $|vac\rangle$ the states $|0\rangle$, $|\sigma\rangle$, $|\bar{\sigma}\sigma\rangle$.

Equation (5.54) can then be used to rewrite the SIAM in the pseudo-particle

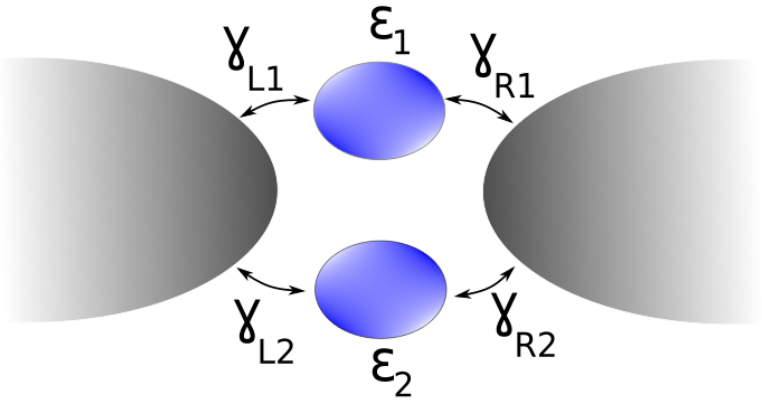


Figure 5.2: Two Anderson impurities coupled to two single-band metallic electrodes. For both electrodes is assumed the wide band approximation.

basis:

$$H_{SIAM} = \sum_{k\sigma} \epsilon_k \hat{a}^{\dagger}_{k\sigma}\hat{a}_{k\sigma} + \sum_{\sigma} \varepsilon \hat{s}^{\dagger}_{\sigma}\hat{s}_{\sigma} + (2\varepsilon + U)\hat{d}^{\dagger}_{\bar{\sigma}\sigma}\hat{s}_{\bar{\sigma}\sigma} + \sum_{k\sigma}(\gamma_k \hat{s}^{\dagger}_{\sigma}\hat{b}\hat{a}_{k\sigma} + H.c.) + \sum_{k\sigma}(\gamma_k \hat{d}^{\dagger}_{\bar{\sigma}\sigma}\hat{s}_{\bar{\sigma}}\hat{c}_{k\sigma} + H.c.) \quad (5.55)$$

By looking at (5.55), we can clearly see the advatages of writing the Hamiltonian in this basis: the non-perturbative many-body Hamiltonian disappeared and its parameter U was incorporated into bilinear terms in the creation and annihilation operators. The price paid is that, in this basis, the coupling term has a more complicated form. However, since we are in the regime of weak coupling, we may employ Green's function-based perturbative methods and, once the pseudo-particles Green's functions are calculated, we may then use (5.54) to obtain the relations between the real electron and the pseudo-particle Green's function.

There are several approximation schemes for calculating the pseudo-particle Green functions. Here we are going to use the non-crossing approximation (NCA) [155]. In appendix C, the auxiliary bosons technique together with the NCA approximation is used to derive expressions for the calculation of the pseudo-particle Green's functions of the multilevel Anderson impurity model in the non-equilibrium regime [1]. Here we are interested in the particular case of SIAM in the equilibrium regime, for which the pseudo-particle self-energies are approximated

[1] Again, we stress that the methodology we ahve developed is method-independent, and thus, does not rely on the type of approximation used to obtain the e-e self-energy.

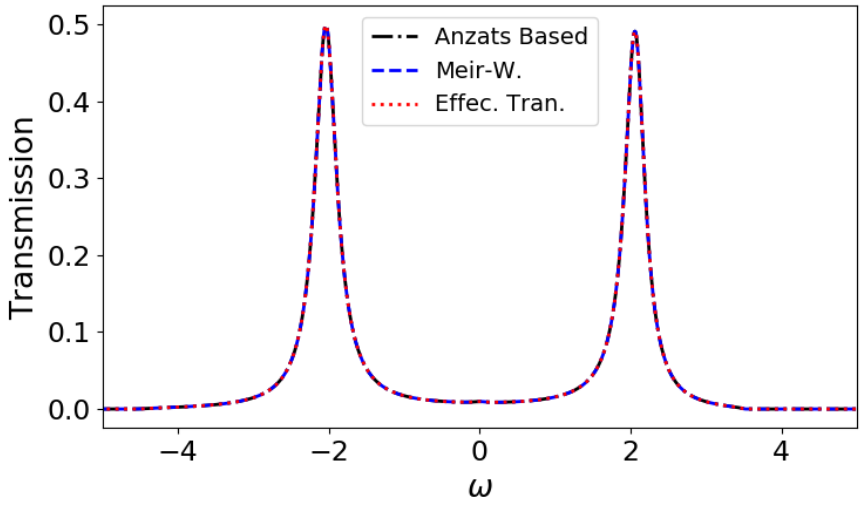


Figure 5.3: Different effective transmissions calculated for the SIAM. There is an agreement among all introduced transmissions for the single impurity even in the case where the proportional coupling condition is not met (the parameters of the calculations are specified in text).

by

$$\Sigma_b(\omega) = \int_{\infty}^{\infty} \frac{d\epsilon}{\pi} f(\epsilon) \sum_{\sigma} \delta_{\sigma}(\epsilon) G_{s_\sigma}(\epsilon+\omega) \Lambda_{\sigma}^{(0)}(\omega,\epsilon), \tag{5.56}$$

$$\Sigma_{s_\sigma}(\omega) = \int_{-\infty}^{\infty} \frac{d\epsilon}{\pi} f(\epsilon)[\Delta_{\sigma}(-\epsilon) G_b(\epsilon+\omega) + \Delta_{\bar{\sigma}} G_{d_{\sigma\bar{\sigma}}}(\epsilon+\omega)], \tag{5.57}$$

$$\Sigma_{d_{\sigma\bar{\sigma}}}(\omega) = \int_{-\infty}^{\infty} \frac{d\epsilon}{\pi} f(\epsilon)[\Delta_{\sigma}(-\epsilon) G_{s_{\bar{\sigma}}} + \Delta_{\bar{\sigma}}(-\epsilon) G_{s_\sigma}]. \tag{5.58}$$

Where $\Delta_\sigma = \sum_k -2\pi|\gamma_k|^2 Im[\mathcal{G}_{kk}]$ is the hybridization function and G_b, G_{s_σ}, G_d the pseudo-particle propagators that are defined in terms of the self-energies according to

$$G_b(\omega) = (\omega - \Sigma_b(\omega))^{-1}, \tag{5.59}$$

$$G_{s_\sigma}(\omega) = (\omega - \varepsilon_0 - \Sigma_{s_\sigma}(\omega))^{-1}, \tag{5.60}$$

$$G_d(\omega) = (\omega - 2\varepsilon_0 - U - \Sigma_d(\omega))^{-1}, \tag{5.61}$$

Equations (5.57)-(5.61) are used to define a self-consistent procedure to calculate the pseudo-particle Green's functions. Once calculated, these functions are then used to calculate the real particle Green's functions via relation (5.54). This method has been extensively used for dealing with SIAM and has shown to be capable of

providing a good description in the high temperature regime [153].

Using this methodology we study a system comprised of a single Anderson impurity coupled to large metalic lead and a semi-infinity tight-binding wire, as depicted in Figure 5.1. For the SIAM we considered an onsite energy $\varepsilon = -2eV$ and Coulomb repulsion $U = 4eV$. For the metalic lead we employed the wide band approximation, where $Im\{\mathcal{G}_{\mathcal{R}}\}$ is set to $-0.5\ 1/eV$ and $\gamma_R(\omega) = 0.3eV$. For the semi-infity wire, we considered an onsite energy of $\varepsilon_{wire} - 0.5eV$ and a hopping term of $t = 2eV$, the coupling between the wire and the impurity is set to be $\gamma_L = 0.3eV$.

The results of the calculation are presented in Figure 5.3. Observe that, as previously pointed out, for the single level case all the introduced transmissions are equivalent and observe the validity of Meir-Wingreen transmission (5.5), that remains correct even beyond the proportional coupling condition. In order words, since we can write $\Gamma_L(\varepsilon) = \lambda(\varepsilon)\Gamma_R(\varepsilon)$, the scalar coupling is energy-wise proportional and Equation (5.5) still holds. This is an important result that is already included in the Ng ansatz and that we highlight here. We can also observe the splitting of the single energy level into two conduction channels because of the energy cost of double occupancy due to the Coulomb interaction; a standard result in the AIM.

The slave bosons technique, together with NCA approximation, can be extended to the multi-impurity Anderson Model. In this case, two Anderson impurities with single particle onsite energies $\varepsilon_1 = -2eV$ and $\varepsilon_2 = -1eV$ coupled to two single band metallic leads, as depicted in Figure 5.2. In order to understand the effect of coupling symmetry breaking in transport, two different calculations will be performed: One in which the system is symmetrically coupled, $\Gamma_L = \Gamma_R$ and another with a symmetry breaking in the coupling $\Gamma_L \neq \Gamma_R$. For both cases the wide band approximation is assumed to hold, with $Im\{\mathcal{G}_{\mathcal{R}(\mathcal{L})} = -0.5\}$ and where, for the symmetrical case, we assumed $\gamma_{1L} = \gamma_{2L} = \gamma_{1R} = \gamma_{2R} = 0.3eV$, while for the assymetrical case is assumed $\gamma_{1L} = \gamma_{1R} = \gamma_{2R} = 0.3eV$ and $\gamma_{2L} = 0.5eV$.

The results of the calculation for the symmetrically coupled system are presented in figure 5.4a. In the same way as the single level case, all the defined transmissions are equivalent, and it is also important to point out that, due to the form chosen for equation (5.51) , each level is independently affected by the Coulomb splitting. On the other hand, the result for the asymmetrically coupled system is presented in figure 5.4b. In this case the transmissions are no longer equivalent and the only transmission with any physical meaning is the one de-

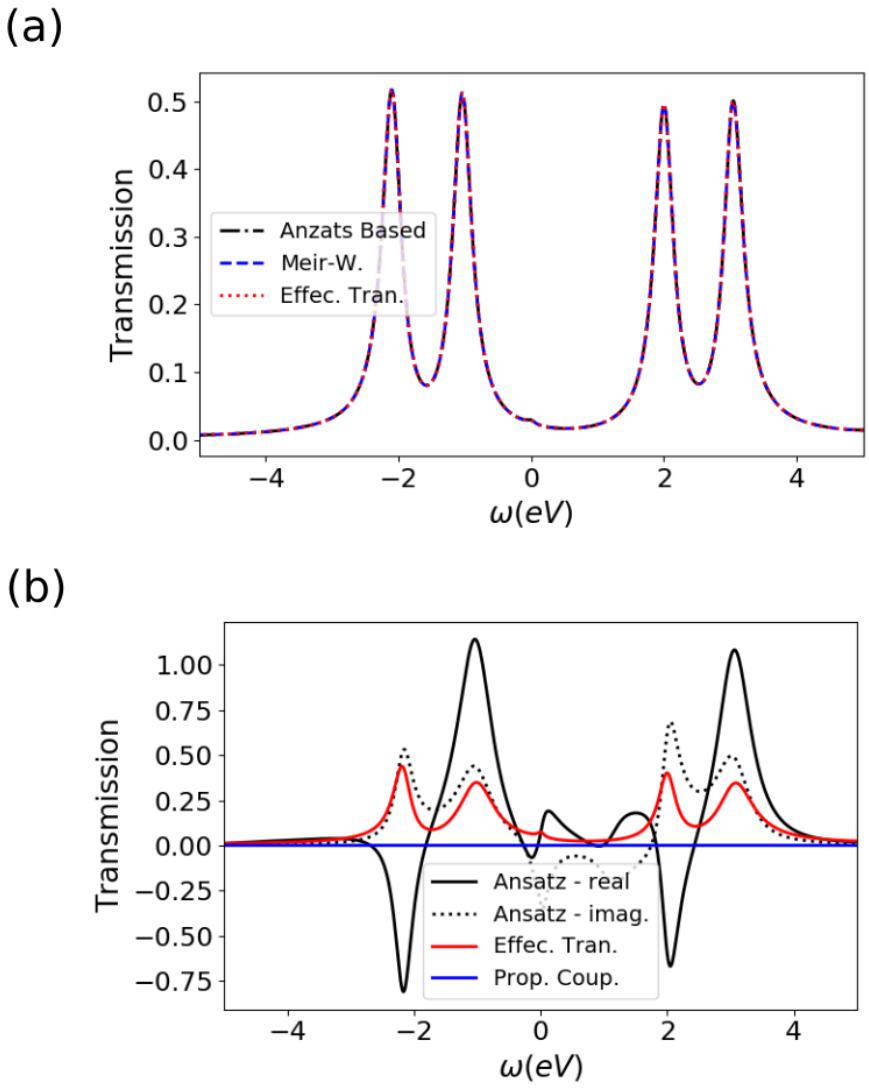


Figure 5.4: Comparison among different effective transmissions for DIAM in the symmetric (upper figure) and asymmetric (lower figure) cases. There is an agreement between between the transmissions in the symmetric case while the derived effective transmission is the only one to provide a reasonable physical transmission in the asymmetric case.

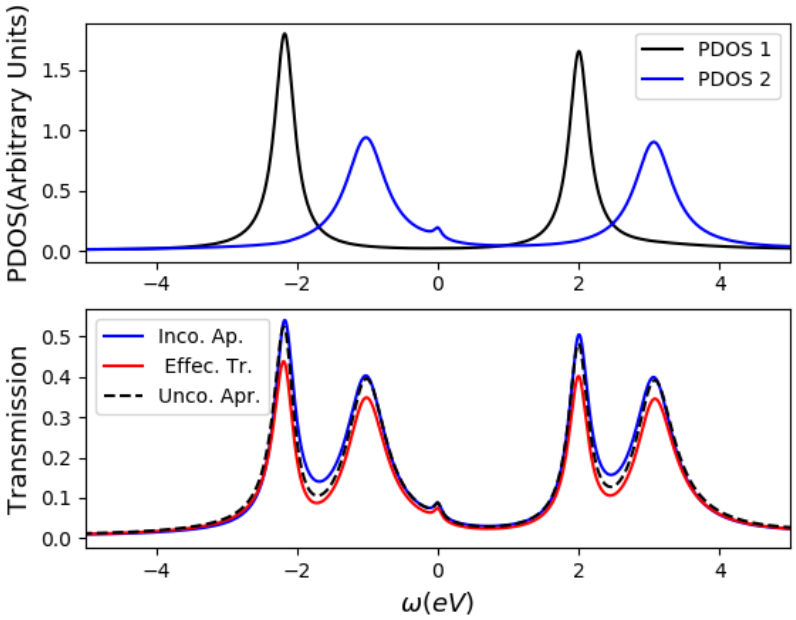


Figure 5.5: Plot of the transmission in the incoherent approximation (5.49), the effective transmission (5.39) and the uncorrelated approximation (5.44). Together with transmissions, in the upper graph is plotted the density of states projected on each energy level (PDOS) for DIAM. The obtained transmissions allows to specify the contribution of each energy level to overall transport and interpret the problem in terms of effective conduction channels.

rived in equation (5.39). In fact, we note that forcing the use of the equation for proportional coupling in a situation where it does not apply leads to a misleading result (a vanishing transmission in this case) while the Ng ansatz based transmission assumes nonphysical imaginary values. Our results on the other hand are consistent with the density of states.

In Figure 5.5 two plots are presented: the firt containing the systems projected density of states (PDOS) and in the second is presented a plot of the transmission in Meir-Wingreen incoherent transport approximation (5.46) together with a plot of the general effective transmission (5.39) and the uncorrelated approximation (5.44). From Figure 5.5 it's possible to observe that, as shown in section 5.4, the uncorrelated and the Meir-Wingreen incoherent approximation provides very similar results in the weak coupling regime. It's also possible to observe that, in this case, both transmission probabilities consist of a good approximation for the general effective transmission, with some small differences in the energies corresponding to the peaks of density of states.

It's very important to understand the effect of the Meir-Wingreen incoherent approximation when compared to the general effective transmission because this approximation is used in the literature not only for describing theoretical models [156], but also for defining phenomenological parameters in experimental works [157]. In Figure 5.5 we can also observe the advantages of defining an effective transmission for the general interacting case, since it allows us to specify the overall contribution of each energy level to transport.

At this point we can validate the idea that there is no reason to expect the anzats based transmission to be valid beyond the single level or the proportional coupling regime, which is exactly what is shown by the results presented in figures 5.3 and 5.4, where the ansatz-based transmission is exact in the single level and symmetrically coupled cases but yields an nonphysical imaginary transmission for the asymmetric case. The same restrictions in the range of applicability is valid for the Meir-Wingreen transmission as well.

5.7 Conclusions

In this work, by using the method of Non-Equilibrium Green Functions, it will be shown how the conservation of flux of charge can be used to deduce an equation

constraining the lesser component of the self-energy and the anti-Hermitian part of the retarded component.

In this chapter we showed how the relation between lesser component of the interacting self-energy and the anti-Hermitian part of the retarded component, imposed by the fluctuation dissipation theorem, can be extended to the non-equilibrium regime of a scattering region coupled to two different reservoirs. This was done by obtaining an exact equation constraining the dependence of these two quantities in the general non-equilibrium case. In addition to that, we used this relation to extend the concept of a quantum transmission function, valid for systems in absence of many-body interactions, to arbitrarily interacting systems.

The derived effective transmission was analytically and numerically compared to two other proposals for the transmission already defined in the literature, namely, the exact Meir-Wingreen transmission for proportional couling and the Ng anzats based transmission. It was shown that all of these transmissions are exact and equivalent for the single level and proportional copling cases. It was also shown that the anzats-based transmission fails to provide a physical result in the general multilevel case.

In addition to a general equation for $\Sigma_{int}^{<}$ a simpler and physically apealling relation was deduced from the constraint equation. It was deduced by neglecting the correlations between the coherent tunneling processes and inner scatterings of the dot. With this relation, $\Sigma_{int}^{<}$ has an equilibrium-like dependence on Γ_{ee} in the sense that each component of the lesser self-energy is proportional to the respective component of the anti-Hermitian self-energy, with the proportionality constant being a generalized out-of-equilibrium ocupation capable of accounting not only for the thermal fluctuations but for tunneling effects as well. With this new relation, it was possible to propose a transmission equation leading to a new theory of uncorrelated transport.

Finally, the incoherent transport equation of Meir-Wingreen and the uncorrelated equation were both numerically and analytically compared to the proposed general transport equation. We discussed the approximations performed in each of these approximated transport theories and it was also studied the case of a weakly coupled double impurity system. The results showed that, for the case studied, both incoherent and uncorrelated approximations furnishes reasonably good descriptions of the general transmission equation.

Chapter 6

General Conclusions

In conclusion, in this work we made an extensive study on the theory of electronic transport in condensed mattery systems. On our analysis, multiple methodologies with different levels of theoretical complexity were used to approach different condensed matter systems. In a first moment, we focused on the influence of magnetic moments on the electronic transport properties of two-dimensional topological insulators (2DTI). Within this realm, we've discerned two distinct transport regimes marked by specific azimuthal and polar angle characteristics of magnetic moments. Notably, an anomalous localization length has been identified, supplementing the standard concept of a localization length and providing a better understanding of the localization regime.

Expanding this analysis to include the hyperfine interaction with nuclear magnetic moments, we find that despite being a valid suppression mechanism, the hyperfine interaction impact on the conductance of HgTe 2DTI systems is negligible. Estimations of localization lengths reveal values with orders of magnitude larger than those observed in experimental devices. Therefore the reduction in transmission due to the hyperfine interaction is calculated to be of a magnitude that doesn't significantly affect the overall conductance.

On the other hand, when exploring the interaction with Mn magnetic impurities, our theoretical predictions, grounded in realistic estimations of model parameters, exhibit a notable decrease in conductance for HgTe topological insulators. Remarkably, our theoretical predictions align closely with experimental values, particularly evident in a system featuring a 1.2% concentration of Mn and a length of 1.9 m.

Shifting gears to our second set of findings, we've unraveled the electronic and thermoelectric properties of the 7-14-7 quantum dot in graphene nanoribbons. Employing *ab initio* calculations and the Green's function formalism, we've provided a comprehensive theoretical description of the system. Our revelations

include the highly localized nature of electronic states at the band edge within the quantum dot's inner region, as opposed to the borders observed in graphene nanoribbons. Importantly, we've demonstrated the tunability of the thermoelectric figure of merit (ZT) through the application of a gate voltage, showcasing promising prospects for quantum dots in graphene nanoribbons in thermoelectric applications.

Concluding our study, we move to non-equilibrium transport theory. We have presented an equation showing how the relation between the lesser and anti-Hermitian components of the interacting self-energy, imposed by the fluctuation-dissipation theorem, can be extended to the non-equilibrium regime of a scattering region coupled to two distinct reservoirs. This was achieved by deriving an exact equation that constrains the relationship between these two quantities in the general non-equilibrium case. Furthermore, we used this relation to extend the concept of a quantum transmission function, originally valid for non-interacting systems, to systems with arbitrarily many-body interactions.

The derived effective transmission was both analytically and numerically compared to two other transmission functions defined in the literature: the exact Meir-Wingreen transmission for proportional coupling, and the Ng ansatz-based transmission. It was shown that all three transmissions are exact and equivalent in the single-level and proportional-coupling cases. However, it was also shown that the ansatz-based transmission fails to provide physically meaningful results in the general multilevel case.

In addition to the more general equation for lesser component of the interacting self-energy, a simpler and more physically appealing relation was deduced from the constraint equation by neglecting correlations between coherent tunneling processes and internal scatterings in the scattering region, an approximation valid in the weak coupling regime. This relation gives the lesser component an equilibrium-like dependence on the anti-Hermitian part retarded interacting self-energy. The dependence is equilibrium-like in the sense that each component of the lesser self-energy is proportional to the corresponding component of the anti-Hermitian self-energy. The proportionality constant represents a generalized out-of-equilibrium occupation factor that accounts for both thermal fluctuations and tunneling effects. With this new relation, we were able to propose a transmission equation leading to a novel theory of uncorrelated transport.

Finally, the incoherent transport equation of Meir-Wingreen and the uncorrelated transport equation were both numerically and analytically compared to the

proposed general transport equation. We discussed the approximations involved in each of these transport theories and investigated a weakly coupled double-impurity system as a case study. The results showed that, for this particular case, both the incoherent and uncorrelated approximations provide reasonably accurate descriptions of the general transmission equation.

In sum, our study presents a comprehensive exploration of condensed matter physics, covering magnetic interactions in 2D topological insulators, thermoelectric properties in graphene quantum dots, and non-equilibrium transport theory. The detailed insights not only enhance our fundamental understanding but also offer practical implications for a range of applications.

Appendix A

Scientific Publications

- Mukim, S.,**Amorim, F. P.**, Rocha, A. R., Muniz, R. B., Lewenkopf, C., Ferreira, M. S. (2020). Disorder information from conductance: a quantum inverse problem. Physical Review B, 102(7), 075409.
- **Amorim, F. P.**, Torres, A., Villegas, C. E., Rocha, A. R. (2023). Gate voltage enhances the thermoelectric transport of quantum dots in graphene nanoribbons. Computational Materials Science, 227, 112207.
- **Amorim, F. P.**, Rocha, A. R., Lewenkopf, C. (Submitted). Generalized Landauer-Büttiker transmission for systems with many-body interactions.
- Santos, W. F., **Amorim, F. P.**, Rocha, A. R., (Submitted) Graphene-based Single-electron Transistors - Simulations of single-electron transistors based on carbon nanotube and graphene nanoribbon junctions
- **Amorim, F. P.**, Ferreira, M. S, Lewenkopf, C. Rocha, A. R. (Soon to be submitted). Conductance suppression of topologically-protected states induced by local magnetic impurities.

Appendix B

Transfer Matrix of Local Magnetic Moment

In this appendix we derive the transfer matrix of a local magnetic moment in a topological insulator, as described by the model:

$$\hat{H} = -\hbar v_0 i\partial_y \begin{pmatrix} 1 & 0 \\ 0 & -1 \end{pmatrix} + \lambda\delta(y) \begin{pmatrix} \cos\theta & e^{-i\phi}\sin\theta \\ e^{i\phi}\sin\theta & -\cos\theta \end{pmatrix} \tag{B.1}$$

Being θ and ϕ the polar and azimuthal angle respectively. The transfer matrix associated to this model can be calculated by relating the energy eigenstates in the regions $y < 0$ and $y > 0$. In order to obtain the energy eigenstates of the system we consider the following representation of $\delta(y)$:

$$\delta(y) = \left\{ \begin{array}{c} \frac{1}{\varepsilon_1+\varepsilon_2} \quad -\varepsilon_2 \leq y \leq \varepsilon_1 \\ 0 \;\; y \leq -\varepsilon_2, \varepsilon_1 \leq y \end{array} \right\} \tag{B.2}$$

The eigenvalue equation for this Hamiltonian is then written as

$$\left[\hbar v_0 i\partial_y \begin{pmatrix} -1 & 0 \\ 0 & 1 \end{pmatrix} + \frac{\lambda}{\varepsilon_1+\varepsilon_2} \begin{pmatrix} \cos(\theta) & e^{-i\phi}\sin(\theta) \\ e^{i\phi}\sin(\theta) & -\cos(\theta) \end{pmatrix}\right] \Psi = E\Psi \text{ for} -\varepsilon_2 \leq y \leq \varepsilon_1 \tag{B.3}$$

and

$$\hbar v_0 i\partial_y \begin{pmatrix} -1 & 0 \\ 0 & 1 \end{pmatrix} \Psi = E\Psi \; for \;\; 0 \;\; y \leq -\varepsilon_2, \varepsilon_1 \leq y \tag{B.4}$$

From Eq. (B.3), by taking the limit $\varepsilon_2 \to 0$ we have that:

$$\partial_y \Psi = \begin{pmatrix} \frac{i}{\hbar v_0}[E - \frac{\lambda\cos\theta}{\varepsilon_1}] & -\frac{i\lambda e^{-i\phi}\sin\theta}{\varepsilon_1\hbar v_0} \\ \frac{i\lambda e^{i\phi}\sin\theta}{\varepsilon_1\hbar v_0} & \frac{-i}{\hbar v_0}[E + \frac{\lambda\cos\theta}{\varepsilon_1}] \end{pmatrix} \Psi = (\frac{iE}{\hbar v_0}B - \frac{i\lambda}{\varepsilon_1\hbar v_0}A)\Psi \tag{B.5}$$

which has as solution

$$\psi(y) = e^{\frac{iE}{\hbar v_0}By - \frac{i\lambda}{\hbar v_0 \varepsilon_1}Ay} \tag{B.6}$$

where

$$A = \begin{pmatrix} \cos(\theta) & e^{-i\phi}\sin(\theta) \\ -e^{i\phi}\sin(\theta) & \cos(\theta) \end{pmatrix}. \tag{B.7}$$

Evaluating the the function at ε_1 and taking the limit $\varepsilon_1 \to 0$ we get:

$$\psi(0^+) = e^{-\frac{i\lambda}{\hbar v_0}A}\psi(0) \tag{B.8}$$

Now observe that

$$\begin{aligned} e^{-i\frac{\lambda}{\hbar v_0}A} &= \exp\left\{ -i\frac{\lambda\cos\theta}{\hbar v_0}\begin{pmatrix} 1 & 0 \\ 0 & 1 \end{pmatrix} - i\frac{\lambda\sin\theta}{\hbar v_0}\begin{pmatrix} 0 & e^{-i\phi} \\ -e^{i\phi} & 0 \end{pmatrix}\right\} \\ &= \exp\left\{ -i\frac{\lambda\cos\theta}{\hbar v_0}\begin{pmatrix} 1 & 0 \\ 0 & 1 \end{pmatrix}\right\} \exp\left\{ -i\frac{\lambda\sin\theta}{\hbar v_0}\begin{pmatrix} 0 & e^{-i\phi} \\ -e^{i\phi} & 0 \end{pmatrix}\right\} \end{aligned}$$

and

$$\exp\left\{ -i\alpha\begin{pmatrix} 1 & 0 \\ 0 & 1 \end{pmatrix}\right\} = (\cos(\alpha) + i\sin(\alpha))\begin{pmatrix} 1 & 0 \\ 0 & 1 \end{pmatrix}; \tag{B.9}$$

$$\exp\left\{ -\beta\begin{pmatrix} 0 & ie^{-i\phi} \\ -ie^{i\phi} & 0 \end{pmatrix}\right\} = \cosh(\beta)\begin{pmatrix} 1 & 0 \\ 0 & 1 \end{pmatrix} + \sinh(\beta)\begin{pmatrix} 0 & ie^{-i\phi} \\ -ie^{i\phi} & 0 \end{pmatrix}. \tag{B.10}$$

Where $\alpha = -\frac{-\lambda\cos(\theta)}{\hbar v_0}$ and $\beta = -\frac{\lambda\sin\theta}{\hbar v_0}$. Hence, the transfer matrix M due to a single delta-potential scatterer is given by

$$M_\delta = e^{\frac{-i\lambda}{\hbar v_0}A} = e^{i\alpha}\begin{pmatrix} \cosh(\beta) & ie^{-i\phi}\sinh(\beta) \\ -ie^{i\phi}\sinh(\beta) & \cosh(\beta) \end{pmatrix} \qquad \alpha = -\frac{-\lambda\cos(\theta)}{\hbar v_0},\ \beta = \frac{-\lambda\sin(\theta)}{\hbar v_0}. \tag{B.11}$$

Appendix C

Proportional coupling condition for systems with inversion symmetry

One important consideration made when deducing (5.1) is the assumption that the leads coupling with the scattering region does not alter its electronic properties. To fulfill this requirement the scattering region is defined to be the molecular system plus some small portion of the leads, which are just large enough to shield the leads from the effects of the molecular system.This definition of the scattering region is named extended molecule.

In many programs the basis used to describe the system consists of a set of atomic and/or molecular orbitals, for this reason we are going adopt the following basis:

$$B = \Big\{ \overbrace{...|\bar{\chi}_1^2\rangle, |\bar{\chi}_{M_L}^1\rangle ..., |\bar{\chi}_2^1\rangle, |\bar{\chi}_1^1\rangle}^{\text{Left lead atomic orbitals}}, \underbrace{|\chi_{N_L}\rangle ... |\chi_2\rangle, |\chi_1\rangle}_{\text{Left E.M. atomic orbitals}}, \overbrace{|\psi_1\rangle, |\psi_2\rangle, ... |\psi_D\rangle}^{\text{Interacting molecular orbitals}}, \underbrace{|\phi_1\rangle, |\phi_2\rangle, ... |\phi_{NR}\rangle}_{\text{Right E.M. atomic orbitals}}, \overbrace{|\bar{\phi}_1^1\rangle, |\bar{\phi}_2^1\rangle, ... |\bar{\phi}_{M_R}^1\rangle, |\bar{\phi}_1^2\rangle ...}^{\text{Right lead atomic orbitals}} \Big\} \quad \text{(C.1)}$$

As is denoted, the interacting molecular levels are described in terms of the orbitals $|\psi_i\rangle$, the left portion of the E.M. by the atomic orbitals $|\chi_j\rangle$ and the right portion by $|\phi_i\rangle$. In the basis B there is also the atomic orbitals $|\bar{\chi}_i^j\rangle$ and $|\bar{\phi}_i^j\rangle$ that describes the left and right leads respectively, note that each lead atomic orbital contains two indices, the upper indice denotes the supercell block and the lower denotes the level. In this basis the Hamiltonian may be written as

$$\hat{H} = \underbrace{\sum_{k=1}^{\infty}\sum_{i,j=1}^{M_L}[H^k_{K_LK_L}]_{ij}\hat{\bar{\chi}}_i^{k\dagger}\hat{\bar{\chi}}_j^k}_{\text{Left lead Hamiltonian}} + \underbrace{\sum_{k=1}^{\infty}\sum_{i,j=1}^{M_R}[H^k_{K_RK_R}]_{ij}\hat{\bar{\phi}}_i^{k\dagger}\hat{\bar{\phi}}_j^k}_{\text{Right lead Hamiltonian}} +$$
$$\underbrace{\sum_{i,j=1}^{N_L}[H_{LL}]_{ij}\hat{\chi}_i^\dagger\hat{\chi}_j + \sum_{i,j=1}^{D}[H_{DD}]_{ij}\hat{\psi}_i^\dagger\hat{\psi}_j + \sum_{i,j=1}^{N_R}[H_{RR}]_{ij}\hat{\phi}_i^{k\dagger}\hat{\phi}_j^k + \hat{H}_{MB}}_{\text{Extended molecule Hamiltonian}} +$$
$$\underbrace{\left(\sum_{i,j=1}^{M_L,N_L}[H^1_{K_LL}]_{ij}\hat{\bar{\chi}}_i^{1\dagger}\hat{\chi}_j + \sum_{i,j=1}^{M_R,N_R}[H_{K_RR}]_{ij}\hat{\bar{\phi}}_i^{1\dagger}\hat{\phi}_j + \sum_{i,j=1}^{N_LD}[H_{LD}]_{ij}\hat{\chi}_i^\dagger\hat{\psi}_j + \sum_{i,j=1}^{N_RD}[H_{RD}]_{ij}\hat{\phi}_i^\dagger\hat{\psi}_j + h.c.\right)}_{\text{Coupling Hamiltonian}} \tag{C.2}$$

$$\hat{H} = \underbrace{H_{K_LK_L}(\bar{\chi}_j)}_{\text{Left Lead Hamiltonian}} + \underbrace{H_{LL}(\chi_j)}_{\text{Left Portion E.M.}} + \underbrace{H_{DD}(\psi_j)}_{\text{Extended Interacting region}} + \underbrace{H_{RR}(\phi_j)}_{\text{Right Portion E.M.}}$$
$$+ \underbrace{H_{K_RK_R}(\bar{\phi}_j)}_{\text{Right Lead Hamiltonian}} + H_{\text{Coupling}} \tag{C.3}$$

Or in matrix form:

$$H = \begin{pmatrix} H_{K_LK_L} & H_{K_LL} & 0 & 0 & 0 \\ H^\dagger_{K_LL} & H_{LL} & H_{LD} & 0 & 0 \\ 0 & H^\dagger_{LD} & H_{DD} & H^\dagger_{RD} & 0 \\ 0 & 0 & H_{RD} & S_{RR} & H^\dagger_{K_RR} \\ 0 & 0 & 0 & H_{K_RR} & H_{K_RK_R} \end{pmatrix}. \tag{C.4}$$

where

$$H_{K_LK_L} = \begin{pmatrix} \ddots & \vdots & \vdots & \vdots \\ \dots & \mathcal{H}_L & \mathcal{V}_L & 0 \\ \dots & \mathcal{V}_L^\dagger & \mathcal{H}_L & \mathcal{V}_L \\ \dots & 0 & \mathcal{V}_L^\dagger & \mathcal{H}_L \end{pmatrix}; \quad H_{K_RK_R} = \begin{pmatrix} \mathcal{H}_R & \mathcal{V}_R & 0 & \dots \\ \mathcal{V}_R^\dagger & \mathcal{H}_R & \mathcal{V}_R & \dots \\ 0 & \mathcal{V}_R^\dagger & \mathcal{H}_R & \dots \\ \vdots & \vdots & \vdots & \ddots \end{pmatrix}. \tag{C.5}$$

Observe that, as a many-body operator, $\hat{H}_{MB}$ does not have any components in this single particle subspace, therefore the hamiltonian (C.4) comprises only the

non-interacting part of (C.3). In the calculation of single particle Green's function the many-body effects may be included by adding the single particle self-energy to (C.4). In this basis the single particle G.F. writes

$$G = \begin{pmatrix} \mathcal{G}_{K_L K_L} & \mathcal{G}_{K_L L} & \mathcal{G}_{K_L D} & \mathcal{G}_{K_L R} & \mathcal{G}_{K_L K_R} \\ \mathcal{G}_{L K_L} & G_{LL} & G_{LD} & G_{LR} & \mathcal{G}_{L K_R} \\ \mathcal{G}_{D K_L} & G_{LD} & G_{DD} & G_{RD} & \mathcal{G}_{D K_R} \\ \mathcal{G}_{R K_L} & G_{RL} & G_{RD} & G_{RR} & \mathcal{G}_{R K_R} \\ \mathcal{G}_{K_R K_L} & \mathcal{G}_{K_R L} & \mathcal{G}_{K_R D} & \mathcal{G}_{K_R R} & \mathcal{G}_{K_R R} \end{pmatrix}. \tag{C.6}$$

where G is used to denote G.F. of the E.M. levels and $\mathcal{G}$ to denote G.F. of the leads levels. Another important quantity is the overlap matrix, that may be represented by

$$S = \begin{pmatrix} S_{K_L K_L} & S_{K_L L} & 0 & 0 & 0 \\ S^{\dagger}_{K_L L} & S_{LL} & S_{LD} & 0 & 0 \\ 0 & S^{\dagger}_{LD} & S_{DD} & S^{\dagger}_{RD} & 0 \\ 0 & 0 & S_{RD} & S_{RR} & S^{\dagger}_{K_R R} \\ 0 & 0 & 0 & S_{K_R R} & S_{K_R K_R} \end{pmatrix}. \tag{C.7}$$

In the subspace of the E.M., the gamma matrix reads:

$$\Gamma_L = \begin{pmatrix} \Omega_L & 0 & 0 \\ 0 & 0 & 0 \\ 0 & 0 & 0 \end{pmatrix}; \Gamma_R = \begin{pmatrix} 0 & 0 & 0 \\ 0 & 0 & 0 \\ 0 & 0 & \Omega_R \end{pmatrix}. \tag{C.8}$$

where

$$\Omega_L = -2H^{\dagger}_{K_L L} Im\{\mathcal{G}_{K_L K_L}\} H_{K_L L} \tag{C.9}$$

$$\Omega_R = -2H^{\dagger}_{K_R R} Im\{\mathcal{G}_{K_R K_R}\} H_{K_R R} \tag{C.10}$$

In the absense of many-body interactions the form of G and $\Gamma_{L/R}$ for the extended molecule poses no problem since, given G^r, the current can be readily calculated by (3.74).In the case where many-body correlations are relevant, considering the situation in which the molecular system couples equally to both leads, the current could in principle be calculated by (5.5), however, due to the extended molecule structure $\Gamma_R \neq \lambda \Gamma_L$ and this equation no longer holds.

In face of this problem some authors just employ the Buttiker-Landauer equation to calculate the transmission, even it's not valid for kind of system. This is the

motivation of the present chapter, which has as its main objective to present an suitable and exact expression for for the current in the extended molecule.

In order to obtain a simpler transport equation lets write the current equation for the E.M. in its more general form, that according to (5.1), (C.6) and (C.8) corresponds to

$$J_L = \frac{ie}{\hbar}\int \frac{d\omega}{2\pi} Tr\{\Omega_L(\omega)[G^<_{LL}(\omega) + i(G^r(\omega)_{LL} - G^a_{LL}(\omega))f_L(\omega)]\}, \tag{C.11}$$

and

$$J_R = \frac{ie}{\hbar}\int \frac{d\omega}{2\pi} Tr\{\Omega_R(\omega)[G^<_{RR}(\omega) + i(G^r(\omega)_{RR} - G^a_{RR}(\omega))f_R(\omega)]\}. \tag{C.12}$$

Now the problem with the E.M. strucuture becomes explicit: the left and right current depends on different components of the G.F.. With this in mind we may try to relate both G_{LL} and G_{RR} to G_{DD}. To accomplish this task observe that the E.M. G.F. obeys

$$(S_{EM}\omega - H_{EM})G^r_{EM}(\omega) = I, \tag{C.13}$$

being S_{EM}, H_{EM} and G_{EM} the matrix blocks restricted to the E.M.:

$$S_{EM} = \begin{pmatrix} S_{LL} & S_{LD} & 0 \\ S^\dagger_{LD} & S_{DD} & S^\dagger_{RD} \\ 0 & S_{RD} & S_{RR} \end{pmatrix}; \; G_{EM} = \begin{pmatrix} G_{LL} & G_{LD} & G_{LR} \\ G_{DL} & G_{DD} & G_{DR} \\ G_{RL} & G_{RD} & G_{RR} \end{pmatrix}; \tag{C.14}$$

And

$$H_{EM} = \begin{pmatrix} H_{LL} + \Delta_L & H_{LD} & 0 \\ H^\dagger_{LD} & H_{DD} + \Sigma_{DD} & H^\dagger_{RD} \\ 0 & H_{RD} & H_{RR} + \Delta_R \end{pmatrix}. \tag{C.15}$$

Observe that, differently from (C.4), the leads degress of freedom were integrated out into H_{EM} through the hybridization functions Δ_L, Δ_R and the effect of the many-body interaction are being taken into account through the one-body self energy Σ_{DD}.

Solving equation (C.13) for G_{LL} (a more detailed proof may be find in the appendice I) we have that:

$$G_{LL} = \hat{G}_{LL} + \hat{G}_{LL}H_{LD}G_{DD}H^\dagger_{LD}\hat{G}_{LL}, \tag{C.16}$$

where

$$\hat{G}_{LL} = \frac{1}{[G^0_{LL}]^{-1} - H^{\dagger}_{K_L L}\mathcal{G}_{K_L K_L}H_{LK_L}}. \tag{C.17}$$

By the equation (C.16) it's possible to relate G_{LL} directly to the surface Green function $\hat{G}_{LL}$ and the dots Green function G_{DD}. The lesser Green function may be obtained means of the Langreth rules:

$$\begin{aligned} G^{<}_{LL} = \hat{G}^{<}_{LL} + \hat{G}^{r}_{LL}H_{LD}G^{r}_{DD}H^{\dagger}_{LD}\hat{G}^{<}_{LL} \\ + \hat{G}^{<}_{LL}H_{LD}G^{a}_{DD}H^{\dagger}_{LD}\hat{G}^{a}_{LL} + \hat{G}^{r}_{LL}H_{LD}G^{<}_{DD}H^{\dagger}_{LD}\hat{G}^{a}_{LL} \end{aligned} \tag{C.18}$$

and the retarded(advanced) Green function is

$$G^{r(a)}_{LL} = \hat{G}^{r(a)}_{LL} + \hat{G}^{r(a)}_{LL}H_{LD}G^{r(a)}_{DD}H^{\dagger}_{LD}\hat{G}^{r(a)}_{LL}. \tag{C.19}$$

Observing that $\hat{G}^{<}_{LL} = -2iIm\{\hat{G}^{r}\}f_L(\omega) = -(\hat{G}^{r} - \hat{G}^{a})f(\omega)$, equation (C.18) may be written as

$$G^{<}_{LL} = -2iIm\{G^{r}\}f_L(\omega) + \hat{G}^{r}_{LL}H_{LD}(G^{<}_{DD} + 2iIm\{G^{r}_{DD}\})H^{\dagger}_{LD}\hat{G}^{a}_{LL} \tag{C.20}$$

where the first term corresponds to the equilibrium component of $G^{<}$ while the second term corresponds to the non-equilibrium contribution. It's interesting to observe that the non-equilibrium component is directly related to the current in the quantum dot.

A interesting result can be derived from (C.20) by substituting this equation in (C.12) and (C.11) :

$$J_L = \frac{ie}{\hbar}\int\frac{d\omega}{2\pi}Tr\{\underbrace{H^{\dagger}_{LD}\hat{G}^{a}_{LL}\Omega_L\hat{G}^{r}_{LL}H_{LD}}_{\tilde{\Gamma}_L(\omega)}[G^{<}_{DD}(\omega) - i(G^{r}_{DD}(\omega) - G^{a}_{DD}(\omega))f_L(\omega)]\}. \tag{C.21}$$

and

$$J_R = \frac{ie}{\hbar}\int\frac{d\omega}{2\pi}Tr\{\underbrace{H^{\dagger}_{RD}\hat{G}^{a}_{RR}\Omega_R\tilde{G}^{r}_{RR}H_{RD}}_{\hat{\Gamma}_R(\omega)}[G^{<}_{DD}(\omega) - i(G^{r}_{DD}(\omega) - G^{a}_{DD}(\omega))f_R(\omega)]\}. \tag{C.22}$$

So, here we can see that the current equation for the extended molecule may be rewritten to have the same form of the general current equation (5.1), where the Green function is replaced by the dots projected Green function G_{DD} and the $\Gamma_{L(R)}$

is replaced by an effective $\tilde{\Gamma}_{L(R)}$. With this equation we overcome the problem of different G.F. components stated before. However, in order to obtain an equation similar to (5.5), we still need to prove that for symmetric systems the proportional coupling condition (in this case $\tilde{\Gamma}_L = \lambda\tilde{\Gamma}_R$) holds.

C.1 Recovering the proportional coupling regime for parity symmetric systems

If the system is symmetric under a parity transformation along the transport direction, considering the origin as the center of E.M., then it's reasonable to assume that the molecule couples equally to both leads. When this is the case it's expected that a simplified transport equation equivalent to (5.5) may be derived, independently of the E.M. structure.

When dealing with numerical calculations some attention should be paid to the necessary condition $\tilde{\Gamma}_L = \lambda^2\tilde{\Gamma}_R$. Since the form of $\tilde{\Gamma}_L$ and $\tilde{\Gamma}_R$ are basis dependent, the proportional coupling condition does not necessarily hold, even in the simetrical case.

One way to assure the proportional coupling to the simetrical case is to choose a basis that reflects the spatial symmetry of the system. Now we are going to prove that the basis B with an anditional constraint on the order of its elements does the job.

If the E.M. is symmetric with respect to a parity transformation along the transport direction, it means that for every atomic orbital $|\xi\rangle$ in the system there is an obital $|\zeta\rangle$ such that: $|\zeta\rangle = \hat{P}|\xi\rangle$, being $\hat{P}$ the parity operator. Now we are going to define the basis B such that

$$|\chi_i\rangle = \hat{P}|\phi_i\rangle, \tag{C.23}$$

$$|\bar{\chi}_i\rangle = \hat{P}|\bar{\phi}_i\rangle. \tag{C.24}$$

Note that the order of the elements $|\phi_i\rangle$ and $|\bar{\phi}_i\rangle$ are respectively determined by the order of $|\chi_i\rangle$ and $|\bar{\chi}_i\rangle$.

Differently from the atomic orbitals of the non-interacting levels, the interacting levels are usually described by a set of molecular orbitals, that means that they

are described not by one but by a linear combination of atomic orbitals. Now we claim that it's aways possible to choose a symmetric lienar combination such that the following relation holds

$$|\Psi_i\rangle = \hat{P}|\Psi_i\rangle \tag{C.25}$$

Using the relations (C.23) (C.24) and (C.25) we have that

$$[S_{K_R K_R}]_{ij} = \langle\bar{\phi}_i|\bar{\phi}_j\rangle = \langle\bar{\phi}_i|\hat{P}\hat{P}|\bar{\phi}_j\rangle = \langle\bar{\chi}_i|\bar{\chi}_j\rangle = [\tilde{\mathbb{I}}_M S_{K_L K_L}\tilde{\mathbb{I}}_M]_{ij} \tag{C.26}$$

$$[S_{RR}]_{ij} = \langle\phi_i|\phi_j\rangle = \langle\phi_i|\hat{P}\hat{P}|\phi_j\rangle = \langle\chi_i|\chi_j\rangle = [\tilde{\mathbb{I}}_N S_{LL}\tilde{\mathbb{I}}_N]_{ij} \tag{C.27}$$

$$[S_{K_R R}]_{ij} = \langle\bar{\phi}_i|\phi_j\rangle = \langle\bar{\phi}_i|\hat{P}\hat{P}|\phi_j\rangle = \langle\bar{\chi}_i|\chi_j\rangle = [\tilde{\mathbb{I}}_M S_{K_L L}\tilde{\mathbb{I}}_N]_{ij} \tag{C.28}$$

$$[S_{RD}]_{ij} = \langle\phi_i|\psi_j\rangle = \langle\phi_i|\hat{P}\hat{P}|\psi_j\rangle = \langle\chi_i|\psi_j\rangle = [\tilde{\mathbb{I}}_N S_{LD}]_{ij} \tag{C.29}$$

being $\tilde{\mathbb{I}}_F$ the antidiagonal square matrix of order F:

$$\tilde{\mathbb{I}}_F = \begin{pmatrix} 0 & 0 & 0 & 1 \\ \vdots & \vdots & \iddots & 0 \\ 0 & 1 & \dots & 0 \\ 1 & 0 & \dots & 0 \end{pmatrix}_{FxF} . \tag{C.30}$$

and the following relations hold:

$$\begin{aligned}
[H_{K_R K_R}]_{ij} &= \langle\bar{\phi}_i|\hat{H}|\bar{\phi}_j\rangle = \langle\bar{\phi}_i|\hat{P}\hat{P}\hat{H}\hat{P}\hat{P}|\bar{\phi}_j\rangle = \langle\bar{\chi}_i|\hat{H}|\bar{\chi}_j\rangle = [\tilde{\mathbb{I}}_M H_{K_L K_L}\tilde{\mathbb{I}}_M]_{ij} \\
[H_{RR}]_{ij} &= \langle\phi_i|\hat{H}|\phi_j\rangle = \langle\phi_i|\hat{P}\hat{P}\hat{H}\hat{P}\hat{P}|\phi_j\rangle = \langle\chi_i|\hat{H}|\chi_j\rangle = [\tilde{\mathbb{I}}_N H_{LL}\tilde{\mathbb{I}}_N]_{ij} \\
[H_{K_R R}]_{ij} &= \langle\bar{\phi}_i|\hat{H}|\phi_j\rangle = \langle\bar{\phi}_i|\hat{P}\hat{P}\hat{H}\hat{P}\hat{P}|\phi_j\rangle = \langle\bar{\chi}_i|\hat{H}|\chi_j\rangle = [\tilde{\mathbb{I}}_M H_{K_L L}\tilde{\mathbb{I}}_N]_{ij} \\
[H_{RD}]_{ij} &= \langle\phi_i|\psi_j\rangle = \langle\phi_i|\hat{P}\hat{P}\hat{H}\hat{P}\hat{P}|\psi_j\rangle = \langle\chi_i|\hat{H}|\psi_j\rangle = [\tilde{\mathbb{I}}_N H_{LD}]_{ij}
\end{aligned} \tag{C.31}$$

As is known, the surface green functions for the leads obeys the relations

$$\mathcal{G}^S_{K_L K_L} = \frac{1}{\omega\mathcal{S}_L - \mathcal{H}_L - \mathcal{V}_L^\dagger \mathcal{G}^S_{K_L K_L}\mathcal{V}_L} \tag{C.32}$$

and

$$\mathcal{G}^S_{K_R K_R} = \frac{1}{\omega\mathcal{S}_R - \mathcal{H}_R - \mathcal{V}_R^\dagger \mathcal{G}^S_{K_R K_R}\mathcal{V}_R}. \tag{C.33}$$

Now, observe that

$$[\mathcal{G}^S_{K_LK_L}]^{-1} = \omega\mathcal{S}_L - \mathcal{H}_L - \mathcal{V}_L^\dagger\mathcal{G}^S_{K_LK_L}\mathcal{V}_L = \tilde{\mathbb{I}}_M[\omega\underbrace{\tilde{\mathbb{I}}_M\mathcal{S}_L\tilde{\mathbb{I}}_M}_{\mathcal{S}_R} - \underbrace{\tilde{\mathbb{I}}_M\mathcal{H}_L\tilde{\mathbb{I}}_M}_{\mathcal{H}_R} - \underbrace{\tilde{\mathbb{I}}_M\mathcal{V}_L^\dagger\tilde{\mathbb{I}}_M}_{\mathcal{V}_R^\dagger}\tilde{\mathbb{I}}_M\mathcal{G}^S_{K_LK_L}\tilde{\mathbb{I}}_M\underbrace{\tilde{\mathbb{I}}_M\mathcal{V}_L\tilde{\mathbb{I}}_M}_{\mathcal{V}_R}]\tilde{\mathbb{I}}_M \tag{C.34}$$

or

$$\tilde{\mathbb{I}}_M[\mathcal{G}^S_{K_LK_L}]^{-1}\tilde{\mathbb{I}}_M = \omega\mathcal{S}_R - \mathcal{H}_R - \mathcal{V}_R^\dagger\tilde{\mathbb{I}}_M\mathcal{G}^S_{K_RK_R}\tilde{\mathbb{I}}_M\mathcal{V}_R, \tag{C.35}$$

so

$$\tilde{\mathbb{I}}_M\mathcal{G}^S_{K_LK_L}\tilde{\mathbb{I}}_M = \frac{1}{\tilde{\mathbb{I}}_M[\mathcal{G}^S_{LL}]^{-1}\tilde{\mathbb{I}}_M} = \frac{1}{\omega\mathcal{S}_R - \mathcal{H}_R - \mathcal{V}_R^\dagger\tilde{\mathbb{I}}_M\mathcal{G}^S_{K_RK_R}\tilde{\mathbb{I}}_M\mathcal{V}_R}. \tag{C.36}$$

Now, comparing (C.33) and (C.36) we conclude

$$\mathcal{G}^S_{K_LK_L} = \tilde{\mathbb{I}}\mathcal{G}^S_{K_RK_R}\tilde{\mathbb{I}} \tag{C.37}$$

Now, let's consider $\hat{G}^r_{LL}$ and $\hat{G}^r_{RR}$:

$$\hat{G}^r_{LL} = \frac{1}{\omega S_{LL} - H_{LL} - H^\dagger_{K_LL}\mathcal{G}^S_{K_LK_L}H_{K_LL}} \tag{C.38}$$

and

$$\hat{G}^r_{RR} = \frac{1}{\omega S_{RR} - H_{RR} - H^\dagger_{K_RR}\mathcal{G}^S_{K_RK_R}H_{K_RR}}. \tag{C.39}$$

Now observe that:

$$[\hat{G}^r_{RR}]^{-1} = \omega S_{RR} - H_{RR} - H^\dagger_{K_RR}\mathcal{G}^S_{K_RK_R}H_{K_RR} = \tilde{\mathbb{I}}_N[\omega\underbrace{\tilde{\mathbb{I}}_N S_{RR}\tilde{\mathbb{I}}_N}_{S_{LL}} - \underbrace{\tilde{\mathbb{I}}_N H_{RR}\tilde{\mathbb{I}}_N}_{H_{LL}} - \underbrace{\tilde{\mathbb{I}}_N H^\dagger_{K_RR}\tilde{\mathbb{I}}_N}_{H^\dagger_{K_LL}}\underbrace{\tilde{\mathbb{I}}_N\mathcal{G}^S_{K_RK_R}\tilde{\mathbb{I}}_N}_{\mathcal{G}^S_{K_LK_L}}\underbrace{\tilde{\mathbb{I}}_N H_{K_RR}\tilde{\mathbb{I}}_N}_{H_{K_LL}}]\tilde{\mathbb{I}}_N \tag{C.40}$$

or

$$[\tilde{\mathbb{I}}_N\hat{G}^r_{RR}\tilde{\mathbb{I}}_N] = \frac{1}{[\tilde{\mathbb{I}}_N[\hat{G}^r_{RR}]^{-1}\tilde{\mathbb{I}}_N]} = \frac{1}{\omega S_{LL} - H_{LL} - H^\dagger_{K_LL}[\mathcal{G}^S_{K_LK_L}]H_{K_LL}} \tag{C.41}$$

comparing (C.41) and (C.38) we get

$$\hat{G}^r_{LL} = (\tilde{\mathbb{I}}_N\hat{G}^r_{RR}\tilde{\mathbb{I}}_N) \tag{C.42}$$

Now, using the results (C.31) and (C.42) we may obtain:

$$\begin{aligned}\tilde{\Gamma}_L(\omega) &= -2H^{\dagger}_{LD}\hat{G}^a_{LL}H^{\dagger}_{K_LL}Im\{\mathcal{G}^R_{K_LK_L}\}H_{K_LL}\tilde{G}^r_{LL}H_{LD}\\ &= -2\underbrace{H^{\dagger}_{LD}\tilde{\mathbb{I}}_N}_{H^{\dagger}_{RD}}\underbrace{\tilde{\mathbb{I}}_N\hat{G}^a_{LL}\tilde{\mathbb{I}}_N}_{\hat{G}^a_{RR}}\underbrace{\tilde{\mathbb{I}}_NH^{\dagger}_{K_LL}\tilde{\mathbb{I}}_N}_{H^{\dagger}_{K_RR}}Im\{\underbrace{\tilde{\mathbb{I}}_N\mathcal{G}^S_{K_LK_L}\tilde{\mathbb{I}}_N}_{\mathcal{G}^L_{K_RK_R}}\}\underbrace{\tilde{\mathbb{I}}_NH_{K_LL}\tilde{\mathbb{I}}_N}_{H_{K_RR}}\underbrace{\tilde{\mathbb{I}}_N\hat{G}^r_{LL}\tilde{\mathbb{I}}_N}_{\hat{G}^{\dagger}_{RR}}\underbrace{\tilde{\mathbb{I}}_NH_{LD}}_{H_{LD}}\\ &= -2H^{\dagger}_{RD}\hat{G}^a_{RR}H^{\dagger}_{K_RR}Im\{\mathcal{G}^R_{K_RK_R}\}H_{K_RR}\tilde{G}^r_{RR}H_{RD} = \tilde{\Gamma}_R(\omega)\end{aligned} \quad (C.43)$$

Thus, we get

$$T(\omega,V) = \frac{-\lambda^2}{1+\lambda^2}Tr\{\tilde{\Gamma}_L[G^r_{DD}(\omega)-G^a_{DD}(\omega)]\} = Tr\left\{\left(\frac{\tilde{\Gamma}_L\tilde{\Gamma}_R}{\tilde{\Gamma}_L+\tilde{\Gamma}_R}\right)(-2iIm[G^r_{DD}(\omega)])\right\}. \quad (C.44)$$

Appendix D

Non-equilibrium multilevel Anderson model in the Non-crossing approximation

In the field of condensed matter physics, the Anderson model has been a fundamental tool for studying the behavior of magnetic impurities within metallic hosts in equilibrium conditions. However, the need to comprehend electronic transport in non-equilibrium scenarios has led to the development and application of the non-equilibrium Anderson model.

The equilibrium Anderson model describes a localized electron level with an occupancy of zero or one electron, coupled with an on-site Coulomb repulsion that governs the interaction with conduction electrons. Electrons can hop between the impurity and the conduction band with a hopping amplitude, forming the basis of the Anderson Hamiltonian.

The non-equilibrium Anderson model introduces a bias voltage , creating a potential difference between the leads and placing the system in a non-equilibrium state. To analyze electronic transport under these conditions, the nonequilibrium Green's function formalism is commonly employed. The Keldysh formalism, utilizing contour-ordered Green's functions, captures time evolution and correlation effects, providing a comprehensive understanding of non-equilibrium quantum transport.

Dynamical mean-field theory is often utilized within this framework, offering a self-consistent approach to account for local interactions and correlations. This proves essential for a detailed examination of the system's behavior in a non-equilibrium environment.

The non-equilibrium Anderson model enables the study of both transient

and steady-state electronic dynamics influenced by the applied bias voltage. It finds application in molecular electronics, particularly in the study of electronic transport through quantum dots, single molecules, and other nanostructures. Understanding the transport properties of electrons through interacting impurities becomes crucial for technological advancements at the nanoscale.

In experimental contexts, the non-equilibrium Anderson model contributes to deciphering electronic transport in various nanostructures subjected to a bias voltage. Its significance extends to molecular electronics, where it plays a pivotal role in unraveling the behavior of individual molecules within electronic circuits.

D.1 General multilevel Anderson impurity model

$$\mathcal{H} = \mathcal{H}_{imp} + \mathcal{H}_{bath} + \mathcal{H}_{hyb} \tag{D.1}$$

where

$$\mathcal{H}_{imp} = \sum_{\alpha\sigma} \epsilon_\alpha \hat{d}^\dagger_{\alpha\sigma}\hat{d}_{\alpha\sigma} + \frac{1}{2}\sum_{\substack{\alpha\beta,\alpha'\beta' \\ \sigma\sigma'}} U_{\alpha\alpha'\beta\beta'}\hat{d}^\dagger_{\alpha\sigma}\hat{d}^\dagger_{\alpha'\sigma'}\hat{d}_{\beta'\sigma'}\hat{d}_{\beta\sigma} \tag{D.2}$$

$$\mathcal{H}_{hyb} = \sum_{k\sigma\gamma}(V_{k\gamma,\alpha}\hat{d}^\dagger_{\alpha\sigma}\hat{c}_{k\sigma\gamma} + V^*_{k\gamma,\alpha}\hat{c}^\dagger_{k\sigma\gamma}\hat{d}_{\alpha\sigma}) \tag{D.3}$$

$$\mathcal{H}_{bath} = \sum_{k\sigma\gamma} \epsilon_{k\gamma}\hat{c}^\dagger_{k\sigma,\gamma}\hat{c}_{k\sigma,\gamma} \tag{D.4}$$

Now, we shall diagonalize the impurity part using the slave bosons method.

$$\mathcal{H}_{imp} = \sum_m E_m |m\rangle\langle m| \tag{D.5}$$

The many-body eigenstates $|m\rangle$ may be represented by Pseudo-particles operators:

$$|m\rangle \rightarrow \text{even number of electrons: } |m\rangle = \hat{b}^\dagger_m|0_{PP}\rangle \tag{D.6}$$

$$|n\rangle \rightarrow \text{odd number of electrons: } |n\rangle = \hat{f}^\dagger_n|0_{PP}\rangle \tag{D.7}$$

Being $|0_{PP}\rangle$ the Pseudo-particle Vacuum and $\hat{b}^\dagger_m$, $\hat{f}^\dagger_m$ operators wich obeys respectively the bosonic and fermionic comutation relations:

$$[\hat{b}_m, \hat{b}^\dagger_{m'}] = \delta_{m,m'} \tag{D.8}$$

$$\{\hat{f}_n, \hat{f}^\dagger_{n'}\} = \delta_{n,n'} \tag{D.9}$$

The physical creation and anihilation operators $\hat{d}^\dagger_{\alpha\sigma}$ and $\hat{d}_{\alpha\sigma}$ may be related to the PP operators by:

$$\hat{d}_{\alpha\sigma} = \sum_{m,n} (F^{\alpha\sigma}_{nm} \hat{b}^\dagger_n \hat{f}_m + F^{\alpha\sigma}_{mn} \hat{f}^\dagger_m \hat{b}_n) \tag{D.10}$$

where $F^{\alpha\sigma}_{nm} = \langle n|\hat{d}_{\alpha\sigma}|m\rangle$.

Now rewriting the Anderson Hamiltonian (D.1) in terms of the PP operators we get

$$\begin{aligned}\mathcal{H} = \hat{H}_{bath} + \sum_m \epsilon_m \hat{f}^\dagger_m \hat{f}_m + \sum_n \epsilon_n \hat{b}^\dagger_n \hat{b}_n + \\ \sum_{\substack{k\sigma\gamma \\ mn}} \left(V_{k\gamma,\alpha} [F^{\alpha\sigma}_{nm} \hat{c}^\dagger_{k\sigma\gamma} \hat{b}^\dagger_n \hat{f}_m + F^{\alpha\sigma}_{mn} \hat{c}^\dagger_{k\sigma\gamma} \hat{f}^\dagger_m \hat{b}_n] + V^*_{k\gamma,\alpha} [F^{*\alpha\sigma}_{nm} \hat{f}^\dagger_m \hat{b}_n \hat{c}_{k\sigma\gamma} + F^{*\alpha\sigma}_{mn} \hat{b}^\dagger_n \hat{f}_m \hat{c}_{k\sigma\gamma}]\right)\end{aligned} \tag{D.11}$$

Now the impurity part is diagonal and the price paid is that the hybridization term becomes more complicated. Moreover, in order to obtain a phisical solution the following constraint has to be applied:

$$Q = \sum_m \hat{f}^\dagger_m \hat{f}_m + \sum_m \hat{b}^\dagger_n \hat{b}_n = 1 \tag{D.12}$$

The non-equilibrium Green Functions are given by

$$G_m(t,t') = \frac{(-i) Tr(\rho_I T_C \{\hat{f}_m(t) \hat{f}^\dagger_m(t')\})}{Tr(\rho_I)}; \tag{D.13}$$

$$K_n(t,t') = \frac{(-i) Tr(\rho_I T_C \{\hat{b}_n(t) \hat{b}^\dagger_n(t')\})}{Tr(\rho_I)} \tag{D.14}$$

Being ρ_I the initial density matrix. In the Dirac picture

$$G_m(t,t') = \frac{(-i) Tr(\rho_I T_C \{\hat{S}_{hyb} \hat{f}_m(t) \hat{f}^\dagger_m(t')\})}{Tr(\rho_I T_C \{\hat{S}_{hyb}\})} \tag{D.15}$$

$$K_n(t,t') = \frac{(-i) Tr(\rho_I T_C \{\hat{S}_{hyb} \hat{b}_n(t) \hat{b}^\dagger_n(t')\})}{Tr(\rho_I T_C \{\hat{S}_{hyb}\})} \tag{D.16}$$

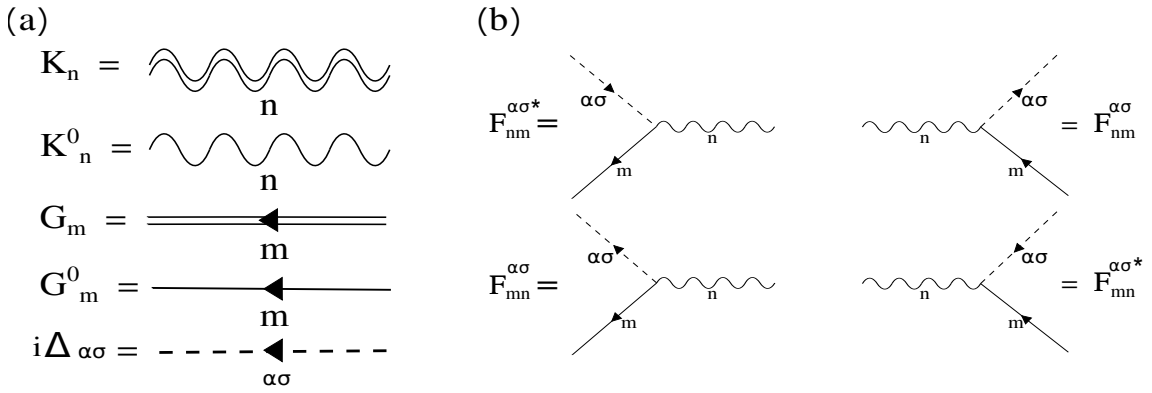


Figure D.1: a-Dressed propagators b-Interaction vertices

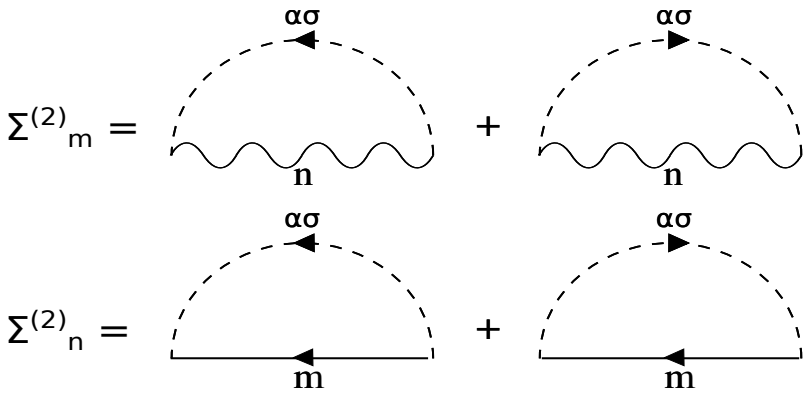


Figure D.2: Leading order diagrams to self-energy

where $S_{hyb} = e^{\int_C H_{hyb}(\tau)d\tau}$.

Expanding S_{hyb} and appying Wick Theorem (it's being considered Keldysh initial conditions), the first non-null leading order terms will be given by

$$G_m^{(2)}(t,t') = \int_C d\tau \int_C d\tau' \sum_{\substack{\alpha\sigma \\ n}} \Big[|F_{nm}^{\alpha\sigma}|^2 G_m^0(t,\tau) i\Delta_{\alpha\sigma,\alpha\sigma}(\tau',\tau) K_n^0(\tau,\tau') G_m^0(\tau',t') + |F_{mn}^{\alpha\sigma}|^2 G_m^0(t,\tau) i\Delta_{\alpha\sigma,\alpha\sigma}(\tau,\tau') K_n^0(\tau,\tau') G_m^0(\tau',t') \Big] \quad \text{(D.17)}$$

being $\Delta_{\alpha\sigma,\alpha\sigma}(t,t') = \mathcal{G}$ From this expansion we may define the Feynman rules, presented in D.1: Given the definition of single-particle self-energy as the sum of all one-particle irreducible diagrams without external legs, the leading order contribution to the fermionic and bosonic P.P. self-energies is shown in D.2. The

corresponding expressions are given by

$$\Sigma_m^{(2)}(t,t') = i\sum_{\substack{\alpha\sigma\\ n}} \left[|F_{nm}^{\alpha\sigma}|^2 \Delta_{\alpha\sigma,\alpha\sigma}(t,t') K_n^0(t,t') + |F_{mn}^{\alpha\sigma}|^2 \Delta_{\alpha\sigma,\alpha\sigma}(t',t) K_n^0(t,t') \right] \quad \text{(D.18)}$$

$$\Sigma_m^{(2)}(\tau,\tau') = i\sum_{\alpha\sigma,n} \left[|F_{nm}^{\alpha\sigma}|^2 \Delta_{\alpha\sigma,\alpha\sigma}(\tau,\tau') \mathcal{G}_n^0(\tau,\tau') + |F_{mn}^{\alpha\sigma}|^2 \Delta_{\alpha\sigma,\alpha\sigma}(\tau',\tau) \mathcal{G}_n^0(\tau,\tau') \right] \quad \text{(D.19)}$$

$$\Sigma_n^{(2)}(t,t') = i\sum_{\substack{\alpha\sigma\\ m}} \left[|F_{mn}^{\alpha\sigma}|^2 \Delta_{\alpha\sigma,\alpha\sigma}(t,t') G_m^0(t,t') + |F_{nm}^{\alpha\sigma}|^2 \Delta_{\alpha\sigma,\alpha\sigma}(t',t) G_m^0(t,t') \right] \quad \text{(D.20)}$$

This approximation for the self-energy may be improved if we replace the bare pseudo-particles propagators by the dressed ones. For the Greens functions this approximation corresponds to a resumation of all diagrams with non-crossing bath propagators, hence it's name: NCA approximation.

Once in the NCA approximation, the lesser and greater self-energy componentes may be find by:

$$\Sigma_m^{(2)<}(t,t') = i\sum_{\substack{\alpha\sigma\\ n}} \left[|F_{nm}^{\alpha\sigma}|^2 \Delta_{\alpha\sigma,\alpha\sigma}^{<}(t,t') K_n^{<}(t,t') + |F_{mn}^{\alpha\sigma}|^2 \Delta_{\alpha\sigma,\alpha\sigma}^{>}(t',t) K_n^{<}(t,t') \right] \quad \text{(D.21)}$$

$$\Sigma_n^{(2)<}(t,t') = i\sum_{\substack{\alpha\sigma\\ m}} \left[|F_{mn}^{\alpha\sigma}|^2 \Delta_{\alpha\sigma,\alpha\sigma}^{<}(t,t') G_m^{<}(t,t') + |F_{nm}^{\alpha\sigma}|^2 \Delta_{\alpha\sigma,\alpha\sigma}^{>}(t',t) G_m^{<}(t,t') \right] \quad \text{(D.22)}$$

and for the greater:

$$\Sigma_m^{(2)>}(t,t') = i\sum_{\substack{\alpha\sigma\\ n}} \left[|F_{nm}^{\alpha\sigma}|^2 \Delta_{\alpha\sigma,\alpha\sigma}^{>}(t,t') K_n^{>}(t,t') + |F_{mn}^{\alpha\sigma}|^2 \Delta_{\alpha\sigma,\alpha\sigma}^{<}(t',t) K_n^{>}(t,t') \right] \quad \text{(D.23)}$$

$$\Sigma_n^{(2)>}(t,t') = i\sum_{\substack{\alpha\sigma\\ m}} \left[|F_{mn}^{\alpha\sigma}|^2 \Delta_{\alpha\sigma,\alpha\sigma}^{>}(t,t') G_m^{>}(t,t') + |F_{nm}^{\alpha\sigma}|^2 \Delta_{\alpha\sigma,\alpha\sigma}^{<}(t',t) G_m^{>}(t,t') \right] \quad \text{(D.24)}$$

in the frequency domain, using the fact that

$$\Delta^{<}_{\alpha\sigma,\alpha\sigma}(\omega) = \sum_{k\sigma,\gamma} V_{k\gamma,\alpha}\mathcal{G}^{<}_{k\sigma}V^{*}_{k\gamma,\alpha} = f(\omega)\Delta^{''}_{\alpha\sigma,\alpha\sigma}(\omega) \tag{D.25}$$

$$\Delta^{>}_{\alpha\sigma,\alpha\sigma}(\omega) = \sum_{k\sigma,\gamma} V_{k\gamma,\alpha}\mathcal{G}^{>}_{k\sigma}V^{*}_{k\gamma,\alpha} = -f(-\omega)\Delta^{''}_{\alpha\sigma,\alpha\sigma}(\omega) = -(1-f(\omega))\Delta^{''}_{\alpha\sigma,\alpha\sigma}(\omega) \tag{D.26}$$

where $\Delta^{''}_{\alpha\sigma,\alpha\sigma}(\omega) = \Delta^{R}_{\alpha\sigma,\alpha\sigma}(\omega) - \Delta^{A}_{\alpha\sigma,\alpha\sigma}(\omega)$, the above equations becomes

$$\Sigma^{(2)<}_{m}(\omega) = i\sum_{\substack{\alpha\sigma \\ n}}\int\frac{du}{2\pi}\Big[|F^{\alpha\sigma}_{nm}|^2(f(u))\Delta^{''}_{\alpha\sigma,\alpha\sigma}(u)K^{<}_{n}(\omega-u) + |F^{\alpha\sigma}_{mn}|^2(-f(-u))\Delta^{''}_{\alpha\sigma,\alpha\sigma}(u)K^{<}_{n}(\omega-u)\Big] \tag{D.27}$$

$$\Sigma^{(2)<}_{n}(\omega) = i\sum_{\substack{\alpha\sigma \\ m}}\frac{du}{2\pi}\Big[|F^{\alpha\sigma}_{mn}|^2(f(u))\Delta^{''}_{\alpha\sigma,\alpha\sigma}(u)G^{<}_{m}(\omega-u) + |F^{\alpha\sigma}_{nm}|^2(-f(-u))\Delta^{''}_{\alpha\sigma,\alpha\sigma}(u)G^{<}_{m}(\omega-u)\Big] \tag{D.28}$$

and for the greater:

$$\Sigma^{(2)>}_{m}(\omega) = i\sum_{\substack{\alpha\sigma \\ n}}\frac{du}{2\pi}\Big[|F^{\alpha\sigma}_{nm}|^2(-f(-u))\Delta^{''}_{\alpha\sigma,\alpha\sigma}(u)K^{>}_{n}(\omega-u) + |F^{\alpha\sigma}_{mn}|^2(f(u))\Delta^{''}_{\alpha\sigma,\alpha\sigma}(u)K^{>}_{n}(\omega-u)\Big] \tag{D.29}$$

$$\Sigma^{(2)}_{m}(\omega) = \sum_{\substack{\alpha\sigma \\ n}}\frac{du}{2\pi}\Big[|F^{\alpha\sigma}_{nm}|^2(-f(-u))\Delta^{''}_{\alpha\sigma,\alpha\sigma}(u)\mathcal{G}^{(2)}_{n}(\omega-u) + |F^{\alpha\sigma}_{mn}|^2(f(u))\Delta^{''}_{\alpha\sigma,\alpha\sigma}(u)\mathcal{G}^{(2)}_{n}(\omega-u)\Big] \tag{D.30}$$

$$\Sigma_n^{(2)>}(\omega) = i\sum_{\substack{\alpha\sigma \\ m}} \frac{du}{2\pi}\Big[|F_{mn}^{\alpha\sigma}|^2(-f(-u))\Delta''_{\alpha\sigma,\alpha\sigma}(u)G_m^{>}(\omega-u) + |F_{nm}^{\alpha\sigma}|^2(f(u))\Delta''_{\alpha\sigma,\alpha\sigma}(u)G_m^{>}(\omega-u)\Big] \quad \text{(D.31)}$$

$$\Sigma_n^{(2)>}(\omega) = i\sum_{\substack{\alpha\sigma \\ m}} \frac{du}{2\pi}\Big[|F_{mn}^{\alpha\sigma}|^2(-f(-u))\Delta''_{\alpha\sigma,\alpha\sigma}(u)G_m^{>}(\omega-u) + |F_{nm}^{\alpha\sigma}|^2(f(u))\Delta''_{\alpha\sigma,\alpha\sigma}(u)G_m^{>}(\omega-u)\Big] \quad \text{(D.32)}$$

The retarded and advanced component may be obtained by:

$$\Sigma^R(\omega) = \int \frac{du}{2\pi}\theta(\omega-u)[\Sigma^{>}(u) - \Sigma^{<}(u)] = I + II \quad \text{(D.33)}$$

where

$$I = -i\sum_{\substack{\alpha\sigma \\ n}} \int \frac{du}{2\pi}\Big[|F_{nm}^{\alpha\sigma}|^2(f(-u))\Delta''_{\alpha\sigma,\alpha\sigma}(u)K_n^R(\omega-u)\Big] - i\sum_{\substack{\alpha\sigma \\ n}} \int \frac{du}{2\pi}\int \frac{dq}{2\pi}\theta(\omega-q-u)\Big[|F_{nm}^{\alpha\sigma}|^2\Delta''_{\alpha\sigma,\alpha\sigma}(u)K_n^{<}(\omega-u)\Big] \quad \text{(D.34)}$$

and

$$II = i\sum_{\substack{\alpha\sigma \\ n}} \int \frac{du}{2\pi}\Big[|F_{mn}^{\alpha\sigma}|^2(f(u))\Delta''_{\alpha\sigma,\alpha\sigma}(u)K_n^R(\omega-u)\Big] i\sum_{\substack{\alpha\sigma \\ n}} \int \frac{du}{2\pi}\int \frac{dq}{2\pi}\theta(\omega-q-u)\Big[|F_{mn}^{\alpha\sigma}|^2\Delta''_{\alpha\sigma,\alpha\sigma}(u)K_n^{<}(\omega-u)\Big] \quad \text{(D.35)}$$

Bibliography

[1] R. Landauer. Spatial variation of currents and fields due to localized scatterers in metallic conduction. *IBM Journal of Research and Development*, 1(3):223–231, 1957.

[2] P. W. Anderson. Absence of diffusion in certain random lattices. *Phys. Rev.*, 109:1492–1505, Mar 1958.

[3] Shinobu Hikami, Anatoly I Larkin, and Yosuke Nagaoka. Spin-orbit interaction and magnetoresistance in the two dimensional random system. *Progress of Theoretical Physics*, 63(2):707–710, 1980.

[4] Bo Zhao, Peihong Cheng, Haiyang Pan, Shuai Zhang, Baigeng Wang, Guanghou Wang, Faxian Xiu, and Fengqi Song. Weak antilocalization in cd3as2 thin films. *Scientific Reports*, 6(1):22377, 2016.

[5] Ilias Amanatidis, Ioannis Kleftogiannis, Fernando Falceto, and Víctor A Gopar. Conductance of one-dimensional quantum wires with anomalous electron wave-function localization. *Physical Review B*, 85(23):235450, 2012.

[6] CM Soukoulis and EN Economou. Off-diagonal disorder in one-dimensional systems. *Physical Review B*, 24(10):5698, 1981.

[7] Rafael A Molina and Victor A Gopar. Transition between anomalous and anderson localization in systems with non-diagonal disorder driven by time-periodic fields. *The European Physical Journal B*, 93:1–7, 2020.

[8] Alain Aspect and Massimo Inguscio. Anderson localization of ultracold atoms. *Physics today*, 62(8):30–35, 2009.

[9] Sandra Eibenberger, Stefan Gerlich, Markus Arndt, Marcel Mayor, and Jens Tüxen. Matter–wave interference of particles selected from a molecular library with masses exceeding 10000 amu. *Physical Chemistry Chemical Physics*, 15(35):14696–14700, 2013.

[10] George P Thomson and Alexander Reid. Diffraction of cathode rays by a thin film. *Nature*, 119(3007):890–890, 1927.

[11] E Flores-Olmedo, AM Martínez-Argüello, M Martínez-Mares, G Báez, JA Franco-Villafañe, and RA Méndez-Sánchez. Experimental evidence of coherent transport. *Scientific Reports*, 6(1):25157, 2016.

[12] F Duncan M Haldane. Model for a quantum hall effect without landau levels: Condensed-matter realization of the" parity anomaly". *Physical review letters*, 61(18):2015, 1988.

[13] Charles L Kane and Eugene J Mele. Quantum spin hall effect in graphene. *Physical review letters*, 95(22):226801, 2005.

[14] Markus König, Steffen Wiedmann, Christoph Brüne, Andreas Roth, Hartmut Buhmann, Laurens W. Molenkamp, Xiao-Liang Qi, and Shou-Cheng Zhang. Quantum spin Hall insulator state in HgTe quantum wells. *Science*, 318(5851):766–770, 2007.

[15] Kostya S Novoselov, Andre K Geim, Sergei V Morozov, De-eng Jiang, Yanshui Zhang, Sergey V Dubonos, Irina V Grigorieva, and Alexandr A Firsov. Electric field effect in atomically thin carbon films. *science*, 306(5696):666–669, 2004.

[16] Ashok K Sood, Isaac Lund, Yash R Puri, Harry Efstathiadis, Pradeep Haldar, Nibir K Dhar, Jay Lewis, Madan Dubey, Eugene Zakar, Priyalal Wijewarnasuriya, et al. *Review of graphene technology and its applications for electronic devices*. InTech London, UK, 2015.

[17] Hideyuki Nakano, Hiroyuki Tetsuka, Michelle JS Spencer, and Tetsuya Morishita. Chemical modification of group iv graphene analogs. *Science and Technology of advanced MaTerialS*, 19(1):76–100, 2018.

[18] Leonid V Keldysh et al. Diagram technique for nonequilibrium processes. *Sov. Phys. JETP*, 20(4):1018–1026, 1965.

[19] Leo P Kadanoff. *Quantum statistical mechanics*. CRC Press, 2018.

[20] Philip Warren Anderson. Localized magnetic states in metals. *Physical Review*, 124(1):41, 1961.

[21] Jun Kondo. Resistance minimum in dilute magnetic alloys. *Progress of theoretical physics*, 32(1):37–49, 1964.

[22] Takeshi Inoshita. Kondo effect in quantum dots. *Science*, 281(5376):526–527, 1998.

[23] DV Averin and KK Likharev. Coulomb blockade of single-electron tunneling, and coherent oscillations in small tunnel junctions. *Journal of low temperature physics*, 62:345–373, 1986.

[24] A Spinelli, M Gerrits, R Toskovic, B Bryant, M Ternes, and AF Otte. Exploring the phase diagram of the two-impurity kondo problem. *Nature communications*, 6(1):10046, 2015.

[25] Leo Kouwenhoven and Leonid Glazman. Revival of the kondo effect. *Physics world*, 14(1):33, 2001.

[26] Joseph Maciejko, Chaoxing Liu, Yuval Oreg, Xiao-Liang Qi, Congjun Wu, and Shou-Cheng Zhang. Kondo effect in the helical edge liquid of the quantum spin Hall state. *Phys. Rev. Lett.*, 102:256803, Jun 2009.

[27] Pavel Daniilovich Kurilovich, Vladislav Daniilovich Kurilovich, Igor Sergeevich Burmistrov, and Moshe Goldstein. Helical edge transport in the presence of a magnetic impurity. *JETP Letters*, 106:593–599, 2017.

[28] Vadim Cheianov and Leonid I Glazman. Mesoscopic fluctuations of conductance of a helical edge contaminated by magnetic impurities. *Physical Review Letters*, 110(20):206803, 2013.

[29] BL Altshuler, IL Aleiner, and VI Yudson. Localization at the edge of a 2d topological insulator by kondo impurities<? format?> with random anisotropies. *Physical Review Letters*, 111(8):086401, 2013.

[30] Jesse A Vaitkus, Cong Son Ho, and Jared H Cole. Effect of magnetic impurity scattering on transport in topological insulators. *Physical Review B*, 106(11):115420, 2022.

[31] Tomasz Dietl. Quantitative theory of backscattering in topological hgte and (hg, mn) te quantum wells: Acceptor states, kondo effect, precessional dephasing, and bound magnetic polaron. *Physical Review B*, 107(8):085421, 2023.

[32] Saquib Shamim, Wouter Beugeling, Pragya Shekhar, Kalle Bendias, Lukas Lunczer, Johannes Kleinlein, Hartmut Buhmann, and Laurens W

Molenkamp. Quantized spin hall conductance in a magnetically doped two dimensional topological insulator. *Nature communications*, 12(1):3193, 2021.

[33] Shiyong Wang, Neerav Kharche, Eduardo Costa Girão, Xinliang Feng, Klaus Mullen, Vincent Meunier, Roman Fasel, and Pascal Ruffieux. Quantum dots in graphene nanoribbons. *Nano letters*, 17(7):4277–4283, 2017.

[34] Daniel S Fisher and Patrick A Lee. Relation between conductivity and transmission matrix. *Physical Review B*, 23(12):6851, 1981.

[35] Yigal Meir, Ned S Wingreen, and Patrick A Lee. Transport through a strongly interacting electron system: Theory of periodic conductance oscillations. *Physical review letters*, 66(23):3048, 1991.

[36] CWJ Beenakker and H Van Houten. Billiard model of a ballistic multiprobe conductor. *Physical review letters*, 63(17):1857, 1989.

[37] Carsten A Ullrich. A not-so-steady state. *Physics*, 3:47, 2010.

[38] Dimitrie Culcer, Aydın Cem Keser, Yongqing Li, and Grigory Tkachov. Transport in two-dimensional topological materials: recent developments in experiment and theory. *2D Mater.*, 7(2):022007, mar 2020.

[39] M. Z. Hasan and C. L. Kane. Colloquium: Topological insulators. *Rev. Mod. Phys.*, 82:3045–3067, Nov 2010.

[40] Xiao-Liang Qi and Shou-Cheng Zhang. Topological insulators and superconductors. *Rev. Mod. Phys.*, 83:1057–1110, Oct 2011.

[41] Antimo Marrazzo, Marco Gibertini, Davide Campi, Nicolas Mounet, and Nicola Marzari. Relative abundance of $\mathbb{Z}_2$ topological order in exfoliable two-dimensional insulators. *Nano Lett.*, 19(12):8431–8440, 2019.

[42] Conan Weeks, Jun Hu, Jason Alicea, Marcel Franz, and Ruqian Wu. Engineering a robust quantum spin Hall state in graphene via adatom deposition. *Phys. Rev. X*, 1:021001, Oct 2011.

[43] A. Avsar, H. Ochoa, F. Guinea, B. Özyilmaz, B. J. van Wees, and I. J. Vera-Marun. Colloquium: Spintronics in graphene and other two-dimensional materials. *Rev. Mod. Phys.*, 92:021003, Jun 2020.

[44] Andreas Roth, Christoph Brüne, Hartmut Buhmann, Laurens W. Molenkamp, Joseph Maciejko, Xiao-Liang Qi, and Shou-Cheng Zhang. Nonlocal transport in the quantum spin Hall state. *Science*, 325(5938):294–297, 2009.

[45] G. M. Gusev, Z. D. Kvon, O. A. Shegai, N. N. Mikhailov, S. A. Dvoretsky, and J. C. Portal. Transport in disordered two-dimensional topological insulators. *Phys. Rev. B*, 84:121302(R), Sep 2011.

[46] Ivan Knez, Charles T. Rettner, See-Hun Yang, Stuart S. P. Parkin, Lingjie Du, Rui-Rui Du, and Gerard Sullivan. Observation of edge transport in the disordered regime of topologically insulating InAs/GaSb quantum wells. *Phys. Rev. Lett.*, 112:026602, Jan 2014.

[47] Lingjie Du, Ivan Knez, Gerard Sullivan, and Rui-Rui Du. Robust helical edge transport in gated InAs/GaSb bilayers. *Phys. Rev. Lett.*, 114:096802, Mar 2015.

[48] F. Reis, G. Li, L. Dudy, M. Bauernfeind, S. Glass, W. Hanke, R. Thomale, J. Schäfer, and R. Claessen. Bismuthene on a SiC substrate: A candidate for a high-temperature quantum spin Hall material. *Science*, 357(6348):287–290, June 2017.

[49] Xiang-Bing Li, Wen-Kai Huang, Yang-Yang Lv, Kai-Wen Zhang, Chao-Long Yang, Bin-Bin Zhang, Y. B. Chen, Shu-Hua Yao, Jian Zhou, Ming-Hui Lu, Li Sheng, Shao-Chun Li, Jin-Feng Jia, Qi-Kun Xue, Yan-Feng Chen, and Ding-Yu Xing. Experimental observation of topological edge states at the surface step edge of the topological insulator $zrte_5$. *Phys. Rev. Lett.*, 116:176803, Apr 2016.

[50] Zaiyao Fei, Tauno Palomaki, Sanfeng Wu, Wenjin Zhao, Xinghan Cai, Bosong Sun, Paul Nguyen, Joseph Finney, Xiaodong Xu, and David H. Cobden. Edge conduction in monolayer WTe_2. *Nat. Phys.*, 13:677–682, 2017.

[51] Sanfeng Wu, Valla Fatemi, Quinn D. Gibson, Kenji Watanabe, Takashi Taniguchi, Robert J. Cava, and Pablo Jarillo-Herrero. Observation of the quantum spin Hall effect up to 100 kelvin in a monolayer crystal. *Science*, 359(6371):76–79, 2018.

[52] K. Hatsuda, H. Mine, T. Nakamura, J. Li, R. Wu, S. Katsumoto, and J. Haruyama. Evidence for a quantum spin Hall phase in graphene decorated with Bi_2Te_3 nanoparticles. *Sci. Adv.*, 4(11):eaau6915, 2018.

[53] Katja C. Nowack, Eric M. Spanton, Matthias Baenninger, Markus König, John R. Kirtley, Beena Kalisky, C. Ames, Philipp Leubner, Christoph Brüne, Hartmut Buhmann, Laurens W. Molenkamp, David Goldhaber-Gordon, and Kathryn A. Moler. Imaging currents in HgTe quantum wells in the quantum spin Hall regime. *Nat. Mater.*, 12:787–791, 2013.

[54] Kyoichi Suzuki, Yuichi Harada, Koji Onomitsu, and Koji Muraki. Edge channel transport in the InAs/GaSb topological insulating phase. *Phys. Rev. B*, 87:235311, Jun 2013.

[55] Lukas Lunczer, Philipp Leubner, Martin Endres, Valentin L. Müller, Christoph Brüne, Hartmut Buhmann, and Laurens W. Molenkamp. Approaching quantization in macroscopic quantum spin Hall devices through gate training. *Phys. Rev. Lett.*, 123:047701, Jul 2019.

[56] Chen-Hsuan Hsu, Peter Stano, Jelena Klinovaja, and Daniel Loss. Helical liquids in semiconductors. *Semicond. Sci. Technol.*, 36(12):123003, oct 2021.

[57] Jukka I. Väyrynen, Dmitry I. Pikulin, and Jason Alicea. Noise-induced backscattering in a quantum spin Hall edge. *Phys. Rev. Lett.*, 121:106601, Sep 2018.

[58] Jianhui Wang, Yigal Meir, and Yuval Gefen. Spontaneous breakdown of topological protection in two dimensions. *Phys. Rev. Lett.*, 118:046801, Jan 2017.

[59] Anders Ström, Henrik Johannesson, and G. I. Japaridze. Edge dynamics in a quantum spin Hall state: Effects from Rashba spin-orbit interaction. *Phys. Rev. Lett.*, 104:256804, Jun 2010.

[60] Jan Carl Budich, Fabrizio Dolcini, Patrik Recher, and Björn Trauzettel. Phonon-induced backscattering in helical edge states. *Phys. Rev. Lett.*, 108:086602, Feb 2012.

[61] Jukka I. Väyrynen, Moshe Goldstein, and Leonid I. Glazman. Helical edge resistance introduced by charge puddles. *Phys. Rev. Lett.*, 110:216402, May 2013.

[62] Flaviano José Santos, Dario A. Bahamon, Roberto B. Muniz, Keith McKenna, Eduardo V. Castro, Johannes Lischner, and Aires Ferreira. Impact of complex adatom-induced interactions on quantum spin Hall phases. *Phys. Rev. B*, 98:081407(R), Aug 2018.

[63] Anders Mathias Lunde and Gloria Platero. Hyperfine interactions in two-dimensional hgte topological insulators. *Phys. Rev. B*, 88:115411, Sep 2013.

[64] Adrian Del Maestro, Timo Hyart, and Bernd Rosenow. Backscattering between helical edge states via dynamic nuclear polarization. *Phys. Rev. B*, 87:165440, Apr 2013.

[65] Chen-Hsuan Hsu, Peter Stano, Jelena Klinovaja, and Daniel Loss. Effects of nuclear spins on the transport properties of the edge of two-dimensional topological insulators. *Phys. Rev. B*, 97:125432, Mar 2018.

[66] Chen-Hsuan Hsu, Peter Stano, Jelena Klinovaja, and Daniel Loss. Nuclear-spin-induced localization of edge states in two-dimensional topological insulators. *Phys. Rev. B*, 96:081405(R), Aug 2017.

[67] Supriyo Datta. *Electronic transport in mesoscopic systems*. Cambridge university press, 1997.

[68] Dmitry A Ryndyk et al. Theory of quantum transport at nanoscale. *Springer Series in Solid-State Sciences*, 184:9, 2016.

[69] B Andrei Bernevig, Taylor L Hughes, and Shou-Cheng Zhang. Quantum spin hall effect and topological phase transition in hgte quantum wells. *science*, 314(5806):1757–1761, 2006.

[70] B. Andrei Bernevig, Taylor L. Hughes, and Shou-Cheng Zhang. Quantum Spin Hall Effect and Topological Phase Transition in HgTe Quantum Wells. *Science*, 314(5806):1757–1761, 2006.

[71] Anders Mathias Lunde and Gloria Platero. Hyperfine interactions in two-dimensional hgte topological insulators. *Physical Review B*, 88(11):115411, 2013.

[72] X. Dang, J. D. Burton, and E. Y. Tsymbal. Magnetic gating of a 2D topological insulator. *J. Phys.: Condens. Matter*, 28:38LT01, 2016.

[73] Leandro R. F. Lima and Caio Lewenkopf. Breakdown of topological protection due to nonmagnetic edge disorder in two-dimensional materials in the quantum spin Hall phase. *Phys. Rev. B*, 106:245408, Dec 2022.

[74] P Markos and C. M. Soukoulis. *Wave Propagation: From Electrons to Photonic Crystals and Left-Handed Materials*. Princeton University Press, Princeton, 2008.

[75] Timothy A. L. Ziman. Localization with off-diagonal disorder: A qualitative theory. *Phys. Rev. B*, 26:7066–7069, Dec 1982.

[76] M. Inui, S. A. Trugman, and Elihu Abrahams. Unusual properties of midband states in systems with off-diagonal disorder. *Phys. Rev. B*, 49:3190–3196, Feb 1994.

[77] Klaus Capelle. A bird's-eye view of density-functional theory. *Brazilian journal of physics*, 36:1318–1343, 2006.

[78] David S Sholl and Janice A Steckel. *Density functional theory: a practical introduction*. John Wiley & Sons, 2022.

[79] Sthitadhi Roy and David E. Logan. Fock-space anatomy of eigenstates across the many-body localization transition. *Phys. Rev. B*, 104:174201, Nov 2021.

[80] Henrik Bruus and Karsten Flensberg. *Many-body quantum theory in condensed matter physics: an introduction*. OUP Oxford, 2004.

[81] Piers Coleman. *Introduction to many-body physics*. Cambridge University Press, 2015.

[82] Denis Lacroix. Review of mean-field theory. *Ecole Joliot-Curie (30 years)" Physics at the femtometer scale". La Colle sur Loup, France*, page 28, 2011.

[83] Gian-Carlo Wick. The evaluation of the collision matrix. *Physical review*, 80(2):268, 1950.

[84] Alexei M Tsvelik. *Quantum field theory in condensed matter physics*. Cambridge university press, 2007.

[85] Herbert B Callen and Theodore A Welton. Irreversibility and generalized noise. *Physical Review*, 83(1):34, 1951.

[86] Václav Špička, Bedřich Velickỳ, and Anděla Kalvová. Electron systems out of equilibrium: Nonequilibrium green's function approach. *International Journal of Modern Physics B*, 28(23):1430013, 2014.

[87] Joseph Maciejko. An introduction to nonequilibrium many-body theory. *Lecture Notes, Springer*, 9(61):104, 2007.

[88] David C Langreth et al. Linear and nonlinear electron transport in solids, 1976.

[89] V Vovchenko, D Anchishkin, J Azema, P Lombardo, R Hayn, and AM Daré. A new approach to time-dependent transport through an interacting quantum dot within the keldysh formalism. *Journal of Physics: Condensed Matter*, 26(1):015306, 2013.

[90] Yuan Li, MBA Jalil, and Seng Ghee Tan. Nonequilibrium keldysh formalism for interacting leads—application to quantum dot transport driven by spin bias. *Annals of Physics*, 327(6):1484–1493, 2012.

[91] Yigal Meir and Ned S. Wingreen. Landauer formula for the current through an interacting electron region. *Phys. Rev. Lett.*, 68:2512, 1992.

[92] Thomas Johann Seebeck. *Magnetische polarisation der metalle und erze durch temperatur-differenz*. Number 70. W. Engelmann, 1895.

[93] Jean Charles Athanase Peltier. *Nouvelles expériences sur la caloricité des courans électriques*. 1834.

[94] William Thomson. 4. on a mechanical theory of thermo-electric currents. *Proceedings of the Royal society of Edinburgh*, 3:91–98, 1857.

[95] M. Jonson and G. D. Mahan. Mott's formula for the thermopower and the wiedemann-franz law. *Phys. Rev. B*, 21:4223, 1980.

[96] U. Sivan and Y. Imry. Multichannel landauer formula for thermoelectric transport with application to thermopower near the mobility edge. *Phys. Rev. B*, 33:551, 1986.

[97] X. Hou, Y. Wang, H. K. H. Lee, R. Datt, N. U. Miano, D. Yan, M. Li, F. Zhu, B. Hou, W. C. Tso, and Z. Li. Indoor application of emerging photovoltaics—progress, challenges and perspectives. *J. Mater. Chem. A*, 8:21503–21525, 2020.

[98] X.-L. Shi, J. Zou, and Z.-G. Chen. Advanced thermoelectric design: From materials and structures to devices. *Chem. Rev.*, 120:7399–7515, 2020.

[99] B. Luo, G. Liu, and L. Wang. Recent advances in 2d materials for photocatalysis. *Nanoscale*, 8:6904–6920, 2016.

[100] J. Cheng, C. Wang, X. Zou, and L. Liao. Recent advances in optoelectronic devices based on 2d materials and their heterostructures. *Adv. Opt. Mater.*, 7:1800441, 2018.

[101] G. Tan, L.-D. Zhao, and M. G. Kanatzidis. Rationally designing high-performance bulk thermoelectric materials. *Chem. Rev.*, 116:12123–12149, 2016.

[102] T. G. Novak, K. Kima, and S. Jeon. 2d and 3d nanostructuring strategies for thermoelectric materials. *Nanoscale*, 11:19684–19699, 2019.

[103] D. Li, Y. Gong, Y. Chen, J. Lin, Q. Khan, Y. Zhang, Y. Li, H. Zhang, and H. Xie. Recent progress of two-dimensional thermoelectric materials. *Nano-Micro Lett.*, 12:36, 2020.

[104] B. Sothmann, R. Sánchez, and A. N. Jordan. Thermoelectric energy harvesting with quantum dots. *Nanotechnology*, 26:032001, 2015.

[105] I-J. Chen, A. Burke, A. Svilans, H. Linke, and C. Thelander. Thermoelectric power factor limit of a 1d nanowire. *Phys. Rev. Lett.*, 120:177703, 2018.

[106] J. J. Urban. Prospects for thermoelectricity in quantum dot hybrid arrays. *Nature Nanotech.*, 10:997–1001, 2015.

[107] E. O. Wrasse, A. Torres, R. J. Baierle, A. Fazzio, and T. M. Schmidt. Size-effect induced high thermoelectric figure of merit in pbse and pbte nanowires. *Phys. Chem. Chem. Phys.*, 16:8114, 2014.

[108] A. I. Boukai, Y. Bunimovich, J. Tahir-Kheli, J.-K. Yu, W. A. Goddard, and J. R. Heath. Silicon nanowires as efficient thermoelectric materials. *Nature*, 451:168–171, 2008.

[109] D. L. Nika, E. P. Pokatilov, A. A. Balandin, V. M. Fomin, A. Rastelli, and O. G. Schmidt. Reduction of lattice thermal conductivity in one-dimensional quantum-dot superlattices due to phonon filtering. *Phys. Rev. B*, 84:165415, 2011.

[110] D. Yang, W. Yao, Y. Yan, W. Qiu, L. Guo, X. Lu, C. Uher, X. Han, G. Wang, T. Yang, and X. Zhou. Intrinsically low thermal conductivity from a quasi-one-dimensional crystal structure and enhanced electrical conductivity network via pb doping in sbcrse3. *NPG Asia Mater.*, 9:e387, 2017.

[111] R. Farghadan and F. Ildarabadi. Gate-voltage induced giant spin seebeck effect in phosphorene nanoribbons. *Phys. Rev. B*, 102:035430, 2020.

[112] R. Ma, H. Geng, W. Y. Deng, M. N. Chen, L. Sheng, and D. Y. Xing. Effect of the edge states on the conductance and thermopower in zigzag phosphorene nanoribbons. *Phys. Rev. B*, 94:125410, 2016.

[113] W. Huang, J.-S. Wang, and G. Liang. Theoretical study on thermoelectric properties of kinked graphene nanoribbons. *Phys. Rev. B*, 84:045410, 2011.

[114] Y. Ouyang and J. Guo. A theoretical study on thermoelectric properties of graphene nanoribbons. *Appl. Phys. Lett.*, 94:263107, 2009.

[115] Z. Zhang, Y. Xie, Q. Peng, and Y. Chen. A theoretical prediction of super high-performance thermoelectric materials based on mos2/ws2 hybrid nanoribbons. *Sci. Rep.*, 6:21639, 2016.

[116] D. D. Fan, H. J. Liu, L. Cheng, P. H. Jiang, J. Shi, and X. F. Tang. Mos2 nanoribbons as promising thermoelectric materials. *Appl. Phys. Lett.*, 105:133113, 2014.

[117] V.-T. Tran, J. Saint-Martin, P. Dollfus, and S. Volz. Optimizing the thermoelectric performance of graphene nanoribbons without degrading the electronic properties. *Nanoscale*, 7:2313, 2017.

[118] Z. W. Tan, J.-S. Wang, and C. K. Gan. First-principles study of heat transport properties of graphene nanoribbons. *Nano Lett.*, 11:214–219, 2011.

[119] L. Liang, E. Cruz-Silva, E. C. Girão, and V. Meunier. Enhanced thermoelectric figure of merit in assembled graphene nanoribbons. *Phys. Rev. B*, 86:115438, 2012.

[120] Y.-B. Dai, K. Luo, and X.-F. Wang. Thermoelectric properties of graphene-like nanoribbon studied from the perspective of symmetry. *Sci. Rep.*, 10:9105, 2020.

[121] V. Saraswat, R. M. Jacobberger, and M. S. Arnold*. Materials science challenges to graphene nanoribbon electronics. *ACS Nano*, 15:3674–3708, 2021.

[122] Y.-W. Son, M. L. Cohen, and S. G. Louie. Energy gaps in graphene nanoribbons. *Phys. Rev. Lett.*, 97:216803, 2006.

[123] W. Y. Rojas, C. E. P. Villegas, and A. R. Rocha. Ab initio modelling of spin relaxation lengths in disordered graphene nanoribbons. *Phys. Chem. Chem. Phys.*, 21:26027–26032, 2019.

[124] C. E. P. Villegas, M. R. S. Tavares, G.-Q. Hai, and P. Vasilopoulos. Plasmon modes and screening in double metallic armchair graphene nanoribbons. *Phys. Rev. B*, 88:165426, 2013.

[125] A. Narita, X. Feng, Y. Hernandez, S. A. Jensen, M. Bonn, H. Yang, I. A. Verzhbitskiy, C. Casiraghi, M. R. Hansen, A. H. R. Koch, G. Fytas, O. Ivasenko, B. Li, K. S. Mali, T. Balandina, S. Mahesh, S. DeFeyter, and K. Müllen. Synthesis of structurally well-defined and liquid-phase-processable graphene nanoribbons. *Nature Chem.*, 6:126–132, 2014.

[126] J. Cai, P. Ruffieux, R. Jaafar, M. Bieri, T. Braun, S. Blankenburg, M. Muoth, A. P. Seitsonen, M. Saleh, X. Feng, Klaus Müllen, and R. Fasel. Atomically precise bottom-up fabrication of graphene nanoribbons. *Nature*, 466:470–473, 2010.

[127] H. Wang, H. S. Wang, C. Ma, L. Chen, C. Jiang, C. Chen, X. Xie, A.-P. Li, and X. Wang. Graphene nanoribbons for quantum electronics. *Nat. Rev. Phys.*, 3:791–802, 2021.

[128] Z. Chen, A. Narita, and K. Müllen. Graphene nanoribbons: On-surface synthesis and integration into electronic devices. *Adv. Mat.*, 32:2001893, 2020.

[129] C. E. P. Villegas, P. B. Mendonça, and A. R. Rocha. Optical spectrum of bottom-up graphene nanoribbons: towards efficient atom-thick excitonic solar cells. *Sci. Rep.*, 4:6579, 2014.

[130] Boris V Senkovskiy, Alexey V Nenashev, Seyed K Alavi, Yannic Falke, Martin Hell, Pantelis Bampoulis, Dmitry V Rybkovskiy, Dmitry Yu Usachov,

Alexander V Fedorov, Alexander I Chernov, et al. Tunneling current modulation in atomically precise graphene nanoribbon heterojunctions. *Nature communications*, 12(1):2542, 2021.

[131] K. Cerņevics, O. V. Yazyev, and M. Pizzochero. Electronic transport across quantum dots in graphene nanoribbons:toward built-in gap-tunable metal-semiconductor-metal heterojunctions. *Phys. Rev. B*, 102:201406(R), 2020.

[132] M. Zhao, D. Kim, V. L. Nguyen, J. Jiang, L. Sun, Y. H. Lee, and H. Yang. Coherent thermoelectric power from graphene quantum dots. *Nano Lett.*, 19:61–68, 2019.

[133] Y. Yan, Q.-F. Liang, H. Zhao, and C.-Q. Wu. Thermoelectric properties of hexagonal graphene quantum dots. *Phys. Lett. A*, 376:1154–1158, 2012.

[134] A. R. Rocha, V. M. García-Suárez, S. Bailey, C. Lambert, J. Ferrer, and S. Sanvito. Spin and molecular electronics in atomically generated orbital landscapes. *Phys. Rev. B*, 73:085414, 2006.

[135] W. Kohn and L. J. Sham. Self-consistent equations including exchange and correlation effects. *Phys. Rev.*, 140:A1133–A1138, 1965.

[136] P. Hohenberg and W. Kohn. Inhomogeneous electron gas. *Phys. Rev.*, 136:B864–B871, 1964.

[137] Alberto García, Nick Papior, Arsalan Akhtar, Emilio Artacho, Volker Blum, Emanuele Bosoni, Pedro Brandimarte, Mads Brandbyge, Jorge I Cerdá, Fabiano Corsetti, et al. Siesta: Recent developments and applications. *The Journal of chemical physics*, 152(20), 2020.

[138] Pablo Ordejón, D Sanchez-Portal, Alberto Garcia, E Artacho, Javier Junquera, and JM Soler. Large scale dft calculations with siesta. *Riken Review*, pages 42–44, 2000.

[139] J. M. Soler, E. Artacho, J. D. Gale, A. García, J. Junquera, P. Ordejón, and D. Sánchez-Portal. The siesta method for ab initio order-n materials simulation. *J. Phys.: Condens. Matter*, 14:2745, 2002.

[140] Felippe P Amorim, Alberto Torres, Cesar EP Villegas, and Alexandre R Rocha. Gate voltage enhances the thermoelectric transport of quantum dots in graphene nanoribbons. *Computational Materials Science*, 227:112207, 2023.

[141] H. Zheng, H. J. Liu, X. J. Tan, H. Y. Lv, L. Pan, J. Shi, and X. F. Tang. Enhanced thermoelectric performance of graphene nanoribbons. *Appl. Phys. Lett.*, 100:093104, 2012.

[142] F. Mazzamuto, V. H. Nguyen, Y. Apertet, Caer, C. Chassat, J. Saint-Martin, and P. Dollfus. Enhanced thermoelectric properties in graphene nanoribbons by resonant tunneling of electrons. *14th International Workshop on Computational Electronics - Phonon and electron transport in graphene nanoribbons*, pages 1–4, 2010.

[143] F. Mazzamuto, V. H. Nguyen, Y. Apertet, Caer, C. Chassat, J. Saint-Martin, and P. Dollfus. Enhanced thermoelectric properties in graphene nanoribbons by resonant tunneling of electrons. *Phys. Rev. B*, 83:235426, 2011.

[144] Daniel S. Fisher and Patrick A. Lee. Relation between conductivity and transmission matrix. *Phys. Rev. B*, 23:6851–6854, Jun 1981.

[145] Yigal Meir and Ned S Wingreen. Landauer formula for the current through an interacting electron region. *Physical review letters*, 68(16):2512, 1992.

[146] A Ferretti, A Calzolari, R Di Felice, and Franca Manghi. First-principles theoretical description of electronic transport including electron-electron correlation. *Physical Review B*, 72(12):125114, 2005.

[147] Tai-Kai Ng. Ac response in the nonequilibrium anderson impurity model. *Physical review letters*, 76(3):487, 1996.

[148] Andrea Ferretti, Arrigo Calzolari, Rosa Di Felice, Franca Manghi, Marilia J Caldas, M Buongiorno Nardelli, and Elisa Molinari. First-principles theory of correlated transport through nanojunctions. *Physical review letters*, 94(11):116802, 2005.

[149] N Sergueev, Qing-feng Sun, Hong Guo, BG Wang, and Jian Wang. Spin-polarized transport through a quantum dot: Anderson model with on-site coulomb repulsion. *Physical Review B*, 65(16):165303, 2002.

[150] Yaakov Kleeorin and Yigal Meir. Quantum phase transition in a realistic double-quantum-dot system. *Scientific Reports*, 8(1):10539, 2018.

[151] Luis G. G. V. Dias da Silva, Caio H. Lewenkopf, Edson Vernek, Gerson J. Ferreira, and Sergio E. Ulloa. Conductance and kondo interference beyond proportional coupling. *Phys. Rev. Lett.*, 119:116801, Sep 2017.

[152] Izrail Moiseevitch Gelfand, Richard A Silverman, et al. *Calculus of variations*. Courier Corporation, 2000.

[153] Bruno Max de Souza Melo, Luis GGV Dias da Silva, Alexandre Reily Rocha, and Caio Lewenkopf. Quantitative comparison of anderson impurity solvers applied to transport in quantum dots. *Journal of Physics: Condensed Matter*, 32(9):095602, 2019.

[154] Piers Coleman. New approach to the mixed-valence problem. *Phys. Rev. B*, 29:3035–3044, Mar 1984.

[155] N. E. Bickers. Review of techniques in the large-n expansion for dilute magnetic alloys. *Rev. Mod. Phys.*, 59:845–939, Oct 1987.

[156] Alvar R Garrigues, Li Yuan, Lejia Wang, Eduardo R Mucciolo, Damien Thompon, Enrique Del Barco, and Christian A Nijhuis. A single-level tunnel model to account for electrical transport through single molecule-and self-assembled monolayer-based junctions. *Scientific reports*, 6(1):1–15, 2016.

[157] Alvar R Garrigues, Lejia Wang, Enrique Del Barco, and Christian A Nijhuis. Electrostatic control over temperature-dependent tunnelling across a single-molecule junction. *Nature communications*, 7(1):1–7, 2016.